Project report

Quantitative modelling of diapirism and geochemical evolution of the subrosion process of salt domes in the northeast Netherlands for radioactive waste disposal

Authors:

Meng Li
Nathalie Collard
Sylvie Schueller
Liviu Matenco
Fadi Henri Nader
Fred Beekman
Marie-Christine Cacas
Jeroen Bartol

Consortium: Utrecht University and IFP Energies Nouvelles

Beneficiary: Ministry of Infrastructure and Water Management

November 2024

Samenvatting

In Nederland, wordt steenzout overwogen voor de geologische eindberging van radioactief afval vanwege de beschikbaarheid, ondoordringbaarheid en vervormbaarheid. Tijdens de geologische evolutie van steenzout kunnen processen zoals diapirisme en subrosie het steenzout aantasten. Op geologische tijdschalen kunnen steenzoutlagen door hun lage dichtheid en viscositeit diapirische structuren vormen die naar de ondiepe ondergrond stijgen. Toppen van diapieren kunnen daar vervolgens eroderen door geochemische interacties met grondwater ("subrosie"). Een beter begrip en kwantificatie van de processen van diapirisme en subrosie op meerdere ruimtelijke schalen en met een hoge resolutie in de tijd is daarom essentieel voor het beoordelen van de lange termijn veiligheid van geologische eindberging in steenzout.

Wij hebben een onderzoeksstudie uitgevoerd naar zoutdiapirisme in noord-oost Nederland. Daarin zijn we begonnen met een al beschikbaar regionaal geologisch model dat is gebaseerd op 3D reflectieseismiek en boorputgegevens en waarin zowel diepe (DGM Diep v.5) als ondiepe (DGM v.2.2) stratigrafische laagvlakken zijn geïntegreerd. Op basis van deze geologische gegevens hebben we een gedetailleerd model op bekkenschaal (100 km × 100 km met 250 m horizontale resolutie) gebouwd, bestaande uit 22 stratigrafische lagen met ouderdom lopend van het Perm tot het Kwartair (van ca. 300 miljion jaar geleden tot het heden), en met een verhoogde resolutie voor de laatste 2 miljoen jaar. Met behulp van de IFPEN-BEICIP TemisFlow™ numerieke modeleringssoftware hebben we vervolgens een kwantitatieve structurele restauratie van het Zechstein zout uitgevoerd om daarmee de ontwikkeling van verschillende zoutstructuren, de snelheid van diapirisme, en de relatie met de warmtestroom en grondwaterstroming in de verschillende stratigrafische stadia in noordoost Nederland te analyseren. Ons numerieke model heeft een hogere tijdstapresolutie voor de meest recente 2 miljoen jaar om de recente evolutie van diapieren in meer detail te kunnen onderzoeken en daarmee de lange termijnstabiliteit van potentiële eindbergingslocaties beter te kunnen voorspellen.

De grote zoutdiapieren zijn doorgaans ontstaan door Mesozoïsche extensie-reactivatie van diepere, onder het zout liggende breukstructuren. Daarbij werd de deformatie van steenzout in onder- en bovenliggende lagen losgekoppeld van elkaar. Zoutdiapirisme versnelde tijdens de belangrijkste latere tektonische gebeurtenissen die het sedimentaire bekken beïnvloedden, en was uitzonderlijk hoog (een factor tien hoger) gedurende de bekkeninversie tijdens het Laat-Krijt–Vroeg-Paleogeen (ca. 100 – 61 miljoen jaar geleden). Echter, op basis van ons onderzoek is er in de afgelopen 2 miljoen jaar weinig tot geen diapirisme geweest, of werden diapieren zelfs dieper begraven. Als de hedendaagse glacio-tektonische omstandigheden niet wezenlijk veranderen, lijkt diapirisme dan ook een minder belangrijke factor dan eerder werd gedacht voor de komende 1 miljoen jaar.

De resultaten van eerdere studies zijn samen met de resultaten van de diapierevolutie en de daaraan gerelateerde grondwaterstroming en warmtestroom gebruikt als input voor de numerieke modellering van subrosie op reservoirschaal. Daarvoor zijn twee, door IFP Energies Nouvelles (IFPEN) ontwikkelde complementaire modelleermethodieken, toegepast: (1) generieke geochemische modellering met Arxim om de effecten van verschillende omgevingscondities op subrosie van steenzout over een periode van 1 miljoen jaar te bestuderen, en (2) 3D reactieve transportmodellering met Geoxim om de subrosieprocessen aan de top en flanken van zoutkoepels over een periode van 10,000 jaar te analyseren. Subrosiesnelheden werden berekend middels geochemische modellering van haliet, sulfaat (haliet + anhydriet) en kalium-magnesium (K-Mg) zoutfacies, waarbij verschillende zoutgehaltes (1 tot 90 g L^{-1}), temperaturen (20 tot 80°C) en Darcy grondwaterstroomsnelheden (1×10^{-6} m yr^{-1} tot 5×10^{-3} m yr^{-1}) over 1 miljoen jaar werden getest.

De resultaten tonen aan dat Darcy stroomsnelheid van grondwater de grootste invloed heeft op de subrosiesnelheid van een zoutdiapier. Voor haliet en K-Mg zoutfacies neemt de subrosiesnelheid lineair toe met grondwaterstroomsnelheid. De subrosiesnelheid wordt ook, maar in mindere mate, beïnvloed door de samenstelling van de subroderende vloeistof: hoe negatiever de verzadigingsindex van de vloeistof ten

opzichte van de mineralogische samenstelling van de diapir, hoe hoger de subrosiesnelheid. Vloeistoffen die niet in evenwicht zijn met carnalliet en kieseriet leiden tot een snellere oplossing van deze mineralen uit de diapier dan die van haliet en anhydriet. De initiële mineralogie van de diapier is belangrijk: de subrosiesnelheid neemt toe bij een hoger gehalte K-Mg zout en neemt af bij een hoger gehalte aan anhydriet. Het bestudeerde temperatuurbereik heeft in vergelijking met de Darcy stroomsnelheid en zoutgehalte van het grondwater en met de initiële mineralogie van de diapier een verwaarloosbaar effect op de subrosiesnelheid.

Uitgedrukt in meter per miljoen jaar (m/My) is subrosie aan de top van de diapir sneller (ca. 10 m/My) is sneller dan aan de randen (ca. 1 m/My) door de hogere stromingssnelheid van grondwater in die specifieke zone. In het model met kaplaag rondom de diapier is de subrosie van de top van de diapier aanzienlijke minder snel, bijna de helft minder, dan in een model zonder kaplaag. De subrosiesnelheid aan de randen van de diapier blijft van dezelfde orde van grootte, of het nu gaat om de opwaartse of neerwaartse stroming langs de flanken. De diepte lijkt daarbij weinig invloed te hebben op de berekende snelheid, waarbij echter vermeld dient te worden dat er onvoldoende hydrogeologische gegevens zijn om een goed gedefinieerd stromingsregime rondom de diapier te definieren in de reactieve transportmodellen: meer onderzoek is vereist om de onderzekerheid in subrosie snelheid verder te reduceren.

Samengevat laat ons 3D bekkenmodel zien dat er langdurige netto-diapirismesnelheden zijn van enkele m/My in het Trias – Vroeg-Krijt, 70 m/My in het Laat-Krijt, en tot minder dan 10 m/My in het Paleogeen – Neogeen. Diapieren zijn in dikte afgenomen en dieper begraven in het Pleistoceen – Holoceen, met een gemiddelde diapirisme snelheid van -10 m/My en uitschieters tot -400 m/My in het Holoceen. Ons 3D reactief transportmodel voorspelt onder theoretisch ideale omstandigheden een subrosiesnelheid van 10 m/My aan de top van de diapieren en 1 m/My aan de randen. Het stromingsregime rondom de diapieren kan deze subrosiesnelheden echter aanzienlijk doen veranderen wanneer hydrogeologische omstandigheden significanter veranderen dan aangenomen. Onze 0D parametrische studie van de effecten van variaties in vloeistofzoutgehalte, temperatuur en vloeistofstroom rapporteert een groot bereik van subrosiesnelheden variërend van 180 m/My tot 3×10^7 m/My, sterk afhankelijk van de Darcy-snelheid. Concluderend laat onze onderzoekstudie op basis van de reconstructie van de recente evolutie van zoutdiapieren en de resultaten van het meer betrouwbare 3D reactieve transportmodel, zien dat een zoutdikte van 350 m rondom een eindbergingslocatie, zoals aangenomen in het huidige Nederlandse bergingsconcept, inderdaad voldoende lijkt om te voorkomen dat diapirisme en subrosie de natuurlijke steenzoutbarrière en daarmee ook de veiligheid van een eindberging in de komende miljoen jaar zullen aantasten.

Gezien de onzekerheden in de geologische modellen die als input zijn gebruikt en de beperkingen van de gebruikte modelleringsmethodieken, adviseren we om aanvullend kwantitatief onderzoek uit te voeren naar diapirisme en subrosie ten behoeve van de ontwikkeling van nauwkeuriger modellen voor veiligheidsbeoordelingen en langetermijnbeheerstrategieën van berging van radioactief afval in steenzout. Specifiek adviseren wij: (1) het maken van een verbeterde 3D weergave van de geometrie van de zoutstructuren door een hogere resolutie interpretatie van de beschikbare seismische en boorputgegevens; (2) een betere numerieke modellering door het toepassen van een tweestappenprocedure met een voorwaartse numerieke modelleringstechniek en een volledig gekoppelde thermomechanisch-geochemische benadering; (3) het uitbreiden van de subrosie dataset met metingen rondom de zoutdiapier van grondwaterstroomsnelheden, regionale hydraulische gradiënten en gesteentepermeabiliteiten; en (4) het gebruikmaken van een groter regionaal subrosiemodel en een volledig 3D diapiermodel voor een betere representatie van het grondwatersnelheidsveld rondom de diapier.

Executive Summary

In the Netherlands, rock salt is considered for the deep geological disposal of radioactive waste due to its availability, impermeability, and deformability. However, processes such as diapirism and subrosion forced by the geological evolution may compromise this rock salt barrier. Over geological timescales, salt forms diapiric structures due to its low density and viscosity, rising to the shallow subsurface where their upper part may be eroded by geochemical interactions with groundwater. Thus, a better understanding and multi-scale quantification of the diapirism and subrosion processes with higher temporal resolution is essential for assessing the long-term safety of geological disposal in rock salt.

We investigated salt diapirism in the northeast Netherlands starting from a readily available combination of regional geological models, including deep (DGM Diep v.5) and shallow (DGM v.2.2) stratigraphic surfaces, as well as lithostratigraphic compositional information, all constrained by previous interpretations of 3D reflection seismics and well data. Based on this combination of information, we have constructed a detailed (250-m horizontal resolution) basin-scale model (100 km × 100 km) that employed 22 Permian– Quaternary stratigraphic surfaces spanning around 260 million years, with increased resolution for the last 2 million years. We employed a quantitative structural restoration approach by using the IFPEN-BEICIP TemisFlow™ numerical modelling approach for the Zechstein salt to integrate the rates of diapirism, evolution of various salt structures and the connection with the thermal and fluid flow evolution at these different stratigraphic stages in the northeast Netherlands. Our model employed an increased temporal resolution for the most recent 2 million years in order to assess with increased details the most recent diapiric evolution for forecasting the long-term stability of potential disposal sites. The large salt domes in the northeast Netherlands generally follow sub-salt fault systems often activated during the Mesozoic extensional evolution, where the salt functioned as a rheologically weak layer decoupling deformation in the underburden from the overburden. Salt diapirism accelerated during the main tectonic events affecting the sedimentary basin and was particularly high (one order of magnitude higher) during the late Cretaceous–early Paleogene (around 100 – 61 million years ago) basin inversion. In contrast, our analysis suggests that diapirism had little to no activity, or even diapirs were buried deeper in the last 2 million years. If the current glacio-tectonic conditions continue and given the uncertainties of our approach, the modelling infers that diapirism is a less important process than previously thought to be relevant for the next 1 million years.

Previous studies combined with the results of the diapir evolution and associated fluid flow and thermal flow are used as input to the subsequent reservoir-scale modeling of subrosion. Two complementary modelling approaches developed by IFP Energies nouvelles were applied: (1) generic geochemical modelling using Arxim to study the effects of different environmental conditions on salt rock subrosion over a 1-million-year period, and (2) 3D reactive transport modelling using Geoxim to investigate the subrosion processes at the top and flanks of salt domes over 10,000 years period. Subrosion rates were calculated through geochemical modelling for halite, sulphate (halite + anhydrite), and potassium - magnesium salt facies, considering varying salinities (1 to 90 g L^{-1}), temperatures (20 to 80°C), and Darcy groundwater flow velocities (1×10^{-6} m yr^{-1} to 5×10^{-3} m yr^{-1}), over 1 million years. The results show that Darcy flow velocity has the most significant impact on subrosion rates which increase linearly with rising velocity for halite and potassium – magnesium salt facies. Less pronounced than the influence of the Darcy's velocity, the subrosion rate is also influenced by the composition of the subroding fluid: the more negative the fluid's saturation index with respect to the diapir mineralogical composition, the higher the subrosion rate. Recharge fluids that are away from equilibrium with carnallite and kieserite cause these minerals to dissolve more quickly than halite and anhydrite. The initial mineralogy of the subroded rock is very important: the subrosion rate increases with a higher proportion of potassium-magnesium salt and decreases with an increase in the amount of anhydrite. The temperature range considered has a negligible effect on the subrosion rate compared to Darcy velocity, salinity, or initial mineralogy.

Expressed in meters per million years (m/My), subrosion at the top of the diapir (i.e., on the order of 10 m/My) is greater than at its margins (i.e., on the order of 1 m/My) due to the higher flow rates in that specific shallower zone. The model incorporating caprock shows a significant reduction in the subrosion rate at the top of the diapir, with the rate being nearly halved compared to the scenario without caprock. The subrosion rate at the margins of the diapir remains of the same order of magnitude, whether on the upstream or downstream flanks, and depth has little effect on the calculated rate. These results may also be due to the low number of hydrogeological constraints used in our study, resulting in a less constrained flow regime around the diapir in the reactive transport simulations: more research is needed to further reduce the uncertainty of the subrosion rate.

In summary, our 3D basin model shows long-term net diapirism rates ranging from a few m/My in the Triassic – Early Cretaceous, 70 m/My in the Late Cretaceous to below 10 m/My in the Paleogene – Neogene. Diapirs have been buried and/or lost thickness in Pleistocene – Holocene with an average diapirism rate of -10 m/My and strongly varying rates up to -400 m/My in Holocene. Our 3D reactive transport model infers a subrosion rate of 10 m/My on the top of the diapirs, and 1 m/My on the margins under theoretical situations, while the flow regime around the diapirs could change these values drastically when hydrogeological conditions change more significantly than assumed. Our 0D parametric study explores the impacts of varying fluid salinity, temperature and fluid flow and reports broad subrosion rates ranging from 180 m/My to 3×10^7 m/My, strongly dependent on the Darcy flow velocity. Considering the overall recent evolution of the salt diapirs and the results of the more reliable 3D reactive transport model, the modelling suggests that a salt thickness of 350 m surrounding the disposal site, as assumed in the current Netherlands disposal concept, seems to be sufficiently conservative to prevent diapirism and subrosion impairing the natural barrier and therefore also the safety of the deep geological disposal for the next one million years.

Given existing constraints and uncertainties of the geological models used as input and the type of modelling used in our study, we strongly recommend further studies continuing on a more quantitative understanding of diapirism and subrosion for the development of accurate repository performance models, safety assessments, and long-term management strategies for disposal in the rock salt. We recommend: (1) an improved representation of the geometry of the salt structures by a higher resolution interpretation of the available reflection seismics and well data, (2) improving the numerical modelling in a two-steps procedure by adding a forward numerical modelling technique and a fully coupled thermo-mechanical-geochemical approach, (3) building an improved subrosion dataset in terms of flow velocities, permeabilities around the salt diapir and the hydraulic gradient at regional scale, and (4) extending the lateral boundaries of the subrosion model and consider a complete 3D representation of the diapir to avoid altering the velocity field around it.

Contents

1 Introduction

In the Netherlands, radioactive waste is generated by nuclear power plants, industry, hospitals, and research organizations. This waste emits ionizing radiation, which can harm living tissue, including humans. Consequently, it must be isolated from the environment until its radiation levels have sufficiently decreased to safe levels. The widely accepted method for long-term isolation is disposal within a stable geological environment deep below Earth's surface where (geological) processes occur at slow and predictable rates over extended periods to minimize influences caused by surface processes or events. In the Netherlands, one option for geological disposal is emplacement of the radioactive waste in a specially mined facility in either rock salt or poorly indurated clay. Worldwide, specially mined deep geological facilities already have or will be constructed for example in clay (Haute Marne, France), crystalline rock (SFR, Sweden; Onkalo, Finland) and rock-salt (WIPP, USA). Furthermore, rock salt has been used for hydrogen storage, such as in Etzel Caverns (Germany), Teesside (HyNet, UK) and has potential for CO2 storage as well, such as in Huttenheim (Germany). Other options for disposal of radioactive waste considered in the Netherlands are deep boreholes and a shared multinational mined repository (Ministry of infrastructure and the Environment, 2016).

For geological disposal in the Netherlands, one of the host rocks that is currently considered is rock salt (Fig 1-1, 1-2). Rock salt functions as a natural barrier for disposal, as it is impermeable (Hansen et al., 2016), self- sealing for fractures (e.g., Urai et al., 2008; Desbois et al., 2012; Berest et al., 2014), encapsulates buried material by creep (Hansen et al., 2016) and has high thermal conductivity (Bartol & Vuorio, 2022). Therefore, rock salt can actively provide good containment. In the meanwhile, the heat generated by decaying radioactive waste can be effectively dissipated, reducing the risk of thermal damage to the repository. Rock salt forms diapirs in the subsurface after deposition, increasing locally in thickness into shallow salt domes that can be reached from the surface. In the Netherlands, the widespread availability of rock salt formations makes them a strong candidate for a future geological repository (Fig 1-1). Yet, salt structures should be studied to understand and predict their future evolution and assess the safety of a repository. Two processes that could impair the natural barrier and could potentially lead to releasing radioactive waste into the environment before it has decayed sufficiently are the continuation of diapirism and subrosion (Prij et al., 1993).

Diapirism involves the upward movement of rock salt through overlying sediment layers due to its lower density and lower viscosity when compared to the overburden clastic or carbonate rocks. If the rate of diapirism is high, there is a potential risk that the salt, along with the radioactive waste it contains, could rise to the surface before the waste radioactivity has decayed sufficiently (Prij et al., 1993). Subrosion is a process taking places at both geological (My) and societal (ky) time scales that involves the dissolution of salt at the margin of diapirs due to percolation of and interactions with fluids such as groundwater. Subrosion reduces the natural salt barrier from it top and sides, which could eventually result in contact between groundwater and the radioactive waste and increase the risk of the release of radionuclides. Therefore, understanding these processes and their rates by developing numerical models to demonstrate the safety of a repository over long geological periods is essential.

Numerous studies have demonstrated that salt forms gradually rising diapiric structures at geological time scales due to its inherent viscous behavior at low temperatures, triggered, enhanced or accelerated by differential loading of the overburden rocks, tectonic stresses or by slow convective processes triggered at geological time scales by differences in composition and burial temperature. Salt diapirism at geological or recent time scales, classified as passive or active using the absence or presence and thickness of a diapir roof as criteria (e.g., Schultz-Ela et al., 1993; Rowan and Gilles, 2021), has been extensively studied by observations including in or around the Netherlands (see the reviews of Geluk et al., 1993; Harding and Huuse, 2015; Jackson and Hudec, 2017) and simulated by modelling studies,

in particular by physical analogue modelling (e.g., Nalpas and Brun, 1993, Brun et al., 1996; Smit et al., 2008; Gabrielssen et al., 2023), but also by numerical models (e.g., Daudre and Cloetingh, 1994; Tilita et al., 2015; Manea et al., 2021; Burton and Dafov, 2023). These studies have demonstrated that diapirism is enhanced by evolving differential loading and tectonic stress. The geological evolution of salt diapirs in the Netherlands is well known, with geometries well quantified either in regional studies (e.g., Geluk et al., 2007 and references therein) or local situations (e.g., Lauwerier, 2022; Almalki, 2023). These studies have shown variable rates of diapirism in the order of 1 – 100 m/My at long-term geological timescales, while the short-term recent evolution may be affected by temporary glacial loading and erosion, sea-level change or fluvial erosional unloading processes (e.g., Geluk et al., 1993; Lang et al., 2014). The salt diapirism rates are well-quantified and understood at long-term geological time scales, while a high-resolution quantification and process-oriented understanding by numerical modelling studies capable of evaluating different stages of diapirism observed in the Netherlands is required to increase the resolution needed for the long-term prediction of rock salt evolution.

Subrosion is the process of removing salt at the top of diapirs by geochemical fluid-rock interaction processes triggered by a reactive ground-water flow that leaves insoluble material agglomerating or not in the formation of salt caprock deposits. Such a removal could eliminate with time the natural salt barrier, releasing the radionuclides in the environments by (ground)water circulation (Prij et al., 1993). Subrosion has been observed and modelled to be accelerated in human-induced situations of diapiric cover removal or enhanced ground-water usage in the proximity of the diapir (e.g., Al-Halbouni et al., 2017; Kobe et al., 2019). It is an important process considered in radioactive waste disposal in specific situations where the salt caprock is influenced by glacial, fluvial erosional or other geomorphological processes, such as the sites considered in Germany (Gerardi and Wildenborg, 1999; Kothe et al., 2007). In the Netherlands, the landmark and still valid multi- disciplinary study of Geluk et al. (1993) has shown a rather complex geochemical interaction process in the formation of the Zuidwending diapir caprock. In this specific situation, dissolution of the salt at the interface with overlying anhydrite is facilitated by a complex network of veins and fractures with the permeability gradually closing with time by the volume expansion during the hydration of anhydrite to gypsum, a process influenced by the conditions of pressure, temperature and reactive fluid saturation. Given the observations and knowledge of the lithostratigraphy of the Zechstein salt in the Netherlands, this subrosion process interpreted for Zuidwending is likely to affect similar rocks elsewhere at the top of Netherlands salt diapirs, although with mixtures of other differently reactive lithologies (carbonates or clay layers) and in different pressure, temperature, neighboring reservoir rocks and fluid saturation conditions. Current long-term estimates from observations in a few salt domes in the NE studies estimates subrosion at the geological time scale to be in the order of 10-100 m/My (e.g., Almalki, 2023; Lauwerier, 2022), although there are significant error bar estimates and the genetic relationship with the stage of diapirism is unclear. Furthermore, these studies lack the higher resolution required to estimate the recent 2 million years (Quaternary) and predict the future evolution of this process.

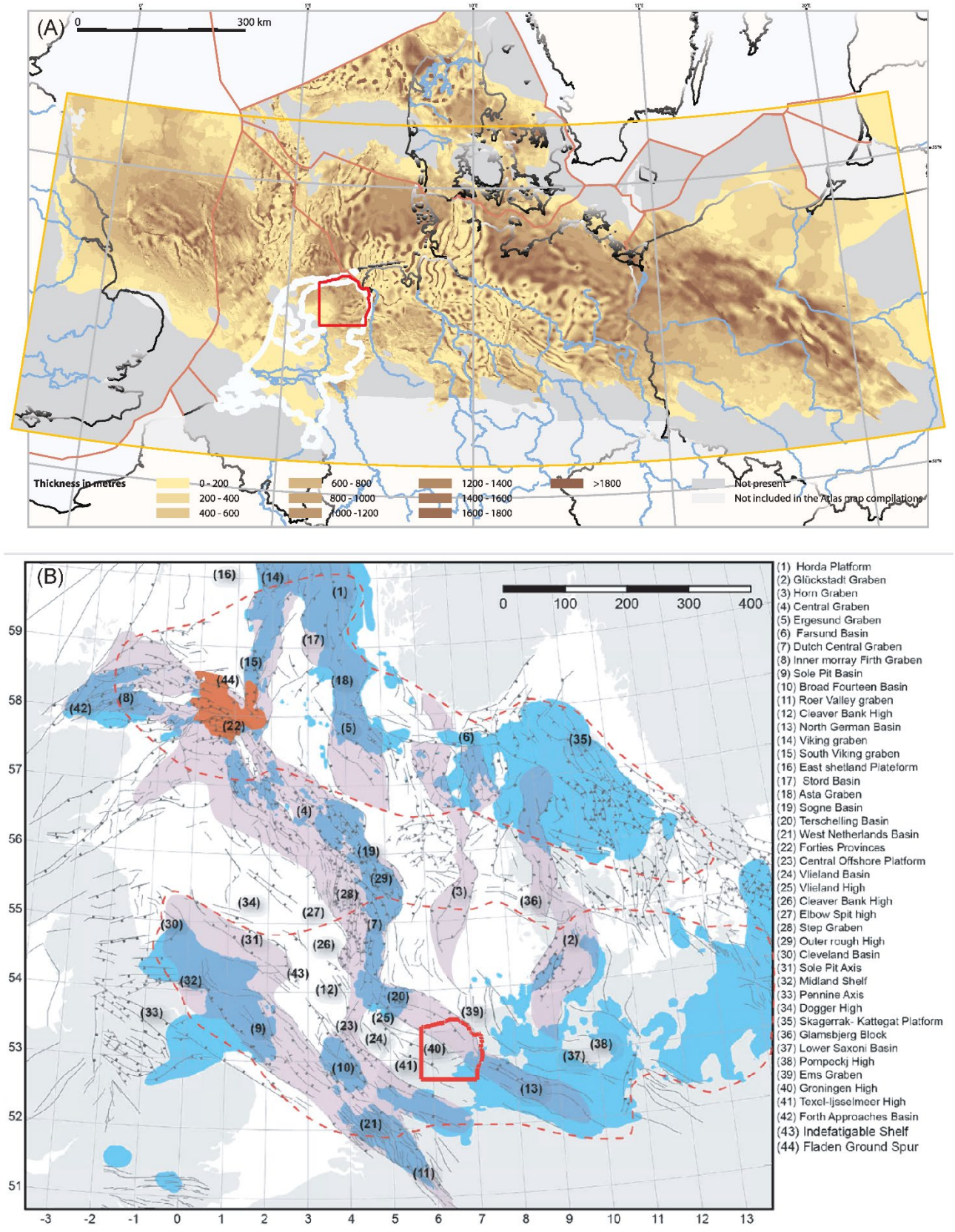

Figure 1-1: (A) Map of the distribution of the Zechstein evaporitic system in the South Permian Basin with the location of the studied area (after Doornebal and Stevenson, 2010). (B) Map of the Triassic – Early Cretaceous extensional system of the North Sea and adjacent areas (Lafosse and Smit, 2020) with the location of the studied area. Pink - Triassic depocenters, blue - Jurassic depocenters, orange - Jurassic magmatism.

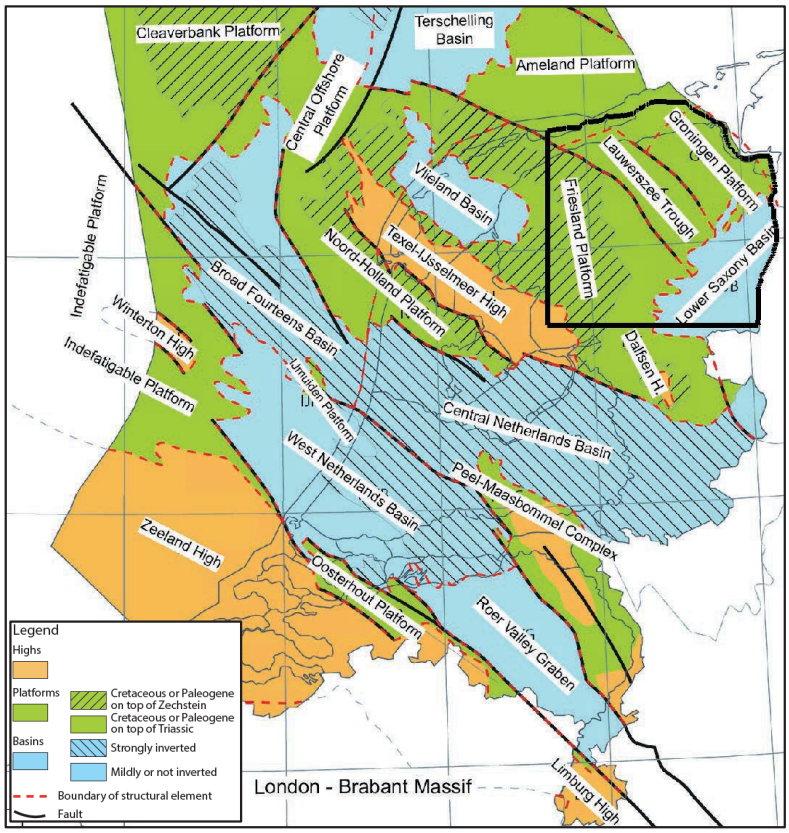

Figure 1-2: Simplified distribution of the main tectonic units in the Netherlands onshore and adjacent offshore (after Kombrink et al., 2012) with the location of the studied area.

Figure 1-3: Detailed location of the studied area in the northeast Netherlands onshore with the location of the main Zechstein diapiric structures (https://www.nlog.nl/en/rock-salt-0).

In this report, we aim to increase our process-oriented understanding and perform a multi-scale quantification of the diapirism process with increased temporal resolution for the most recent evolution in Pleistocene – Holocene times. To quantify the evolution of various salt domes at different evolution stages in the Netherlands, we combined existing geological model to build a regional integrated 3D basin model that accounts for the thermal and burial history of the onshore northeast Netherlands, and conducted coupled fluid and thermal flow simulations to simulate the evolution of salt structures from their formation at the scales of this studied area and (sub-)basin diapiric structures.

As no specific site has been chosen yet for radioactive waste disposal, we use the observed variability of existing Zechstein salt structures in the northeast Netherlands (Fig 1-3) to build a process-oriented understanding of their generic evolution. The studied area also includes traditional salt mining sites and currently used gas/oil storage sites. The studied diapirs include both massive salt domes that are in the range of hundreds of meters to the surface, such as Gasselte-Drouwen, Zuidwending, Winschoten, Anloo, Onstwedde, Pieterburen, Hooghalen, Schoonloo, Ternaard and Boertange, and deeper diapirs, columnar or more distributed, such as Klein Ulsda, Hoogezand, Gerkesklooster and Hoogeveen. Among them, Ternaard is partly located beneath the offshore Waddenzee.

2 Background

The study area in the NE onshore Netherlands covers parts of a number of tectonic units inherited from the evolution of the much larger South Permian Basin and the Mesozoic extensional and inversion history of NW Europe (Figs 1.1-1.2), namely the Lower Saxony Basin, Groningen Platform, Lauwerszee Trough, and Friesland Platform (Fig 2-1). The Lower Saxony Basin spans northern Germany and extends into the eastern Netherlands. It developed during the Permian and Mesozoic, heavily influenced by the Variscan orogeny and later by Jurassic rifting and Cretaceous inversion events. The basin is known for its thick deposits of Permian Zechstein salts and significant hydrocarbons, particularly gas reserves. The Groningen Platform, known for the very large Groningen gas field was less affected by the intense tectonic activity that shaped the surrounding basins, remaining relatively stable during the Permian-Mesozoic times. The Lauwerszee Trough is a northeast-trending sub-basin located between the Groningen High and the Friesland Platform, being separated from the later by the Hantum Fault Zone. The Friesland Platform is a more stable structural region compared to the surrounding basins that was significantly uplifted and eroded during the Late Jurassic.

2.1 Zechstein salt

The dominantly evaporitic Zechstein Group consists of distinct sedimentary cycles that represent different depositional environments within a large salt basin (Fig 2-2). The stratigraphic nomenclature used in the Netherlands is based on names derived from their German counterparts (Van Adrichem Boogaert & Kouwe, 1994). The five main cycles—Z1-Werra, Z2-Stassfurt, Z3-Leine, Z4-Aller, and Z5-Ohre Formations—are comparable across both the Dutch and North German Basins (Geluk et al., 2000; Peryt, et al., 2010).

The depth of the base of the Zechstein deposits varies significantly, ranging from around 700 meters in the southeast onshore to over 5000 meters in the northern offshore areas, such as the Dutch Central Graben, while it is significantly reduced or missing in the central NL onshore and adjacent offshore (Duin et al., 2006). Generally, the thickness of the salt increases toward the north, where it is dominated by highly deformed salt structures, including pillows, domes, and diapirs. These structures can reach thicknesses greater than 1300 meters in both the northern onshore and offshore regions. In contrast, in the southern to central on- and offshore areas, where the Zechstein Sea was shallower, the salt layers are much thinner, ranging from 50 to 200 meters, or may be absent altogether. In these regions, the Zechstein consists mainly of residual carbonates and anhydrite layers that are only meters to tens of meters thick (Duin et al., 2006).

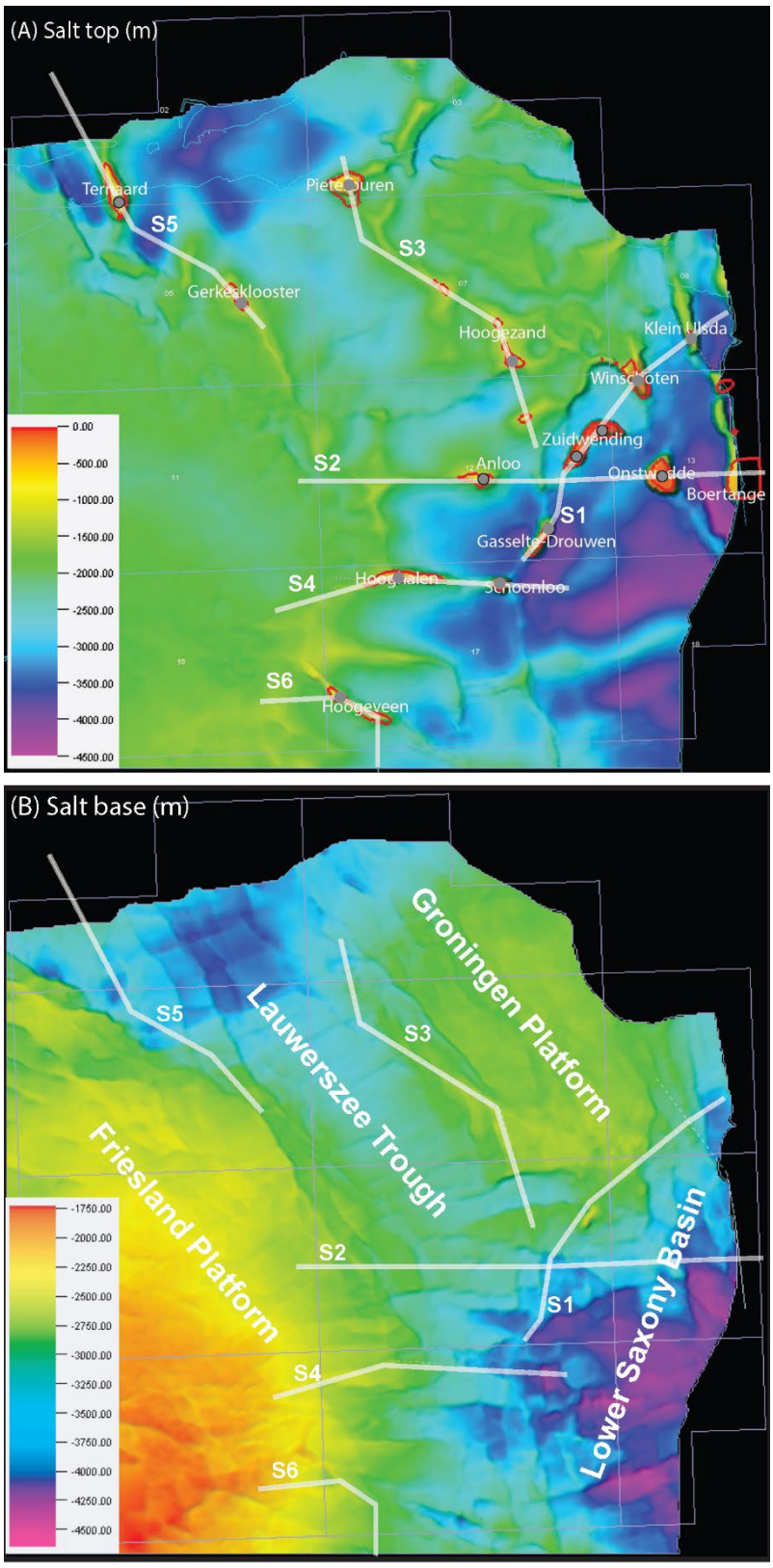

Figure 2-1: Depth maps of the top of (A) Zechstein Group and (B) top Rotliegend Group in the studied area (TNO-GDN, 2019). The location of the main salt domes (red lines) in (A) after https://www.nlog.nl/en/rock-salt-0 and the tectonic units in (B) after Kombrink et al. (2012). S1-S6 are the locations of the cross-sections in Figs 3-3, 3-4. Gray circles are the locations of the diapirs where diapirism rates are calculated. Gray circles with black rims are used as case studies in Chapter 4.

Following the well-established stratigraphy and evolution in the Netherlands (e.g., Geluk 2000, 2007; Strozyk et al., 2017), the Z1 - Werra Formation marks the initial marine transgression of the Zechstein

Sea into the Southern Permian Basin. The lower part of the cycle typically contains carbonates (limestone and dolomite) deposited during the early marine phase. As the water in the basin began to evaporate, anhydrite (calcium sulfate) and halite (rock salt) were precipitated. In the final stages of evaporation, more soluble salts like potassium salts (e.g., sylvite and carnallite) were deposited. The Z1 salt can reach significant thickness, particularly in subbasins like the Werra-Fulda Subbasin in Germany. It is mechanically coupled to the underlying Permian and Carboniferous sediments.

Z2 - Stassfurt Formation: Another marine transgression followed the partial evaporation of the Zechstein Sea after Z1. This cycle starts with the Z2 Basal Anhydrite, followed by thick halite deposits sometimes exceeding 500 m in thickness. Z2 is generally thinner than Z1 but can still contain significant amounts of evaporites. Potassium salts and other evaporites often cap the cycle as the last remnants of water evaporated.

Z3 - Leine Formation: Z3 represents the third major flooding event, followed by evaporation. This cycle includes claystone, dolomitic limestone, and anhydrite, with rock salt layers. The Main Anhydrite is particularly thick in some areas, reaching up to 150 m, and is fragmented due to movement in the underlying Z2 salt. The Z3 salt layer is thinner than Z2 but still significant, especially in northern onshore regions of the Netherlands.

Z4 - Aller Formation: Dominated by halite, the Z4 salt layer reaches up to 100 m thick. Potassium-magnesium-bearing salts are found at the top, and the cycle indicates a transition to more silici- clastic sedimentation in the basin margins.

Z5 - Ohre Formation: Z5 marks the final marine transgression and evaporation event. The Z5 cycle is relatively thin, with claystones and thin halite layers in the Netherlands. Z5 is often eroded or absent in some areas due to later geological processes. In Germany, additional cycles such as Z6 (Friesland) and Z7 (Fulda) are present, but these do not extend into the Netherlands. The Zechstein Upper Claystone Formation (ZEUC) forms the upper boundary of the Zechstein Group in the Netherlands, marking the end of significant evaporite deposition.

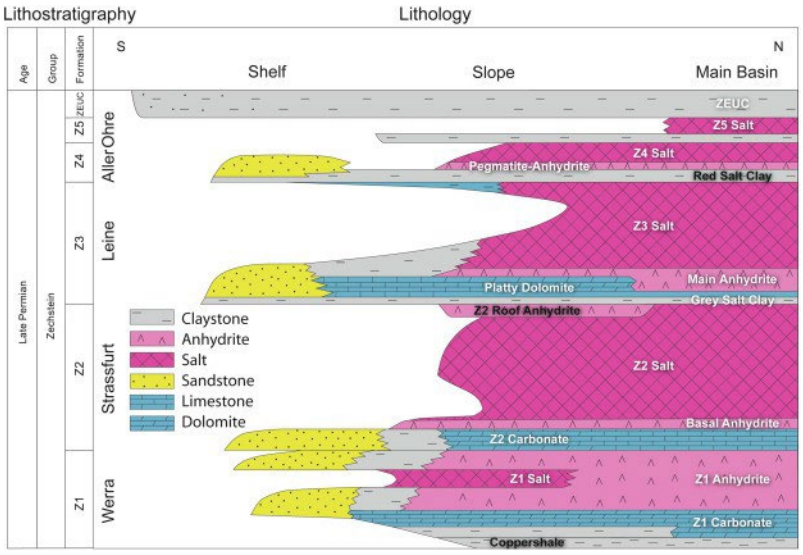

Figure 2-2: Basic Dutch Zechstein stratigraphy and lithology and their changes from the main basin, across the slope to the shelf/platform facies. Strozyk et al. (2017), modified after Geluk (2000).

2.2 Salt mechanics

Salt diapirism is a geological process in which a mass of salt rises through overlying rock layers due to its lower density and the pressure from the overlying materials. This process is driven primarily by the buoyancy of the salt. There are the three major modes of salt diapirism: active, passive and reactive modes, differentiated by the major driving force (Jackson & Hudec, 2017). Salt is much less dense than most sedimentary rocks, so when it is buried deep beneath the Earth's surface under layers of heavier rock, it tends to rise in response to the pressure exerted by these overlying rocks (active diapirism). This buoyancy effect is the fundamental mechanism that causes the salt to move upward, often forming structures such as salt domes, pillows, and walls. One key characteristic of salt that enables diapirism is its ductile behavior. When sedimentary layers are deposited unevenly (differential loading), areas of greater pressure can push the salt toward areas of lower pressure, facilitating its rise toward the surface (reactive diapirism). Tectonic forces also play a significant role in salt diapirism. In tectonically active regions, movements such as crustal extension or compression can either pull salt upwards or squeeze it into diapiric structures. In extensional regimes, salt can flow upward due to thinning of the overburden. While in compressional regimes, salt may be pushed into the cores of folds or squeezed upward along faults. Fault zones, in particular, can act as conduits for salt movement, allowing the salt to pierce through overlying rock layers more easily, forming fault-aligned salt diapirs. When the salt is already at surface, the salt thickness continues to grow as new layers of sediment are deposited around it (passive diapirism). As the salt rises, it may also cause the surrounding rocks to subside into the space left behind, forming what are known as salt withdrawal basins, or rim synclines, where syn-kinematic deposition can be studied to derive the timing of salt movement. These basins often form ring-like depressions around salt domes. Over time, the upward movement of salt can create complex subsurface structures that influence the surrounding geology, particularly in terms of how the overlying sedimentary layers are folded and faulted.

Subrosion is the process where salt at the margins or in the interior of a diapir dissolves in reactive fluids and is removed through natural groundwater circulation. This dissolution occurs when reactive water (or other fluids) infiltrates the subsurface and comes into contact with the salt. As the salt dissolves into the water, cavities form within the diapir or along its flanks, leading to the gradual collapse or subsidence of overlying sediments and rocks. The process becomes more pronounced when the salt reaches near-surface levels due to enhanced hydrogeological circulation of reactive water or other fluids. In regions with significant subrosion activity, this process can lead to faulting, fracturing and the formation of subsidence basins (e.g., Al-Halbouni et al., 2017; Kobe et al., 2019).

3 Methodology

3.1 Data collection and model initiation

Having collected data on past subrosion and diapirism rates, and the internal structure and thermo-hydro-mechanical properties of salt, the next step of the project is to develop a numerical solution to explore and quantify the evolution of salt structures and subrosion through time. Based on the synthesis of previous studies, we build numerical models to comprehensively reproduce the diapirism and subrosion rates at geological timescale with an increased resolution for the recent geological times. Our models also involve a quantification of the critical fluid-rock interaction geochemical processes involved in subrosion. By the requirement of generically quantifying different Netherlands salt domes in various stages of evolution, the first 3D model is at the scale of a (sub-)basin, in practice at the scale of the northern Netherlands onshore. We have selected the area containing the main diapiric Zechstein structures, which is roughly ~ 100 km × 100 km in the NL Groningen - Friesland - Overijssel provinces. The proven fluid-rock interaction processes defining subrosion at the top of the salt diapir take place at the (fluid-circulating) reservoir scale. Therefore, the second model is at the reservoir scale, mainly around one diapiric structure. We have employed a multi-scale non-coupled integrated approach by using a sequence of state-of-the-art numerical modelling codes, solving specific scale- and physics-defined processes at both scales and integrate their results in a stepwise, non-coupled and sequential order. This stepwise approach is available in the integrated numerical platform OpenFlow (IFPEN, Beicip Franlab, 2021, licensed at Utrecht University), which includes all individual software packages described below.

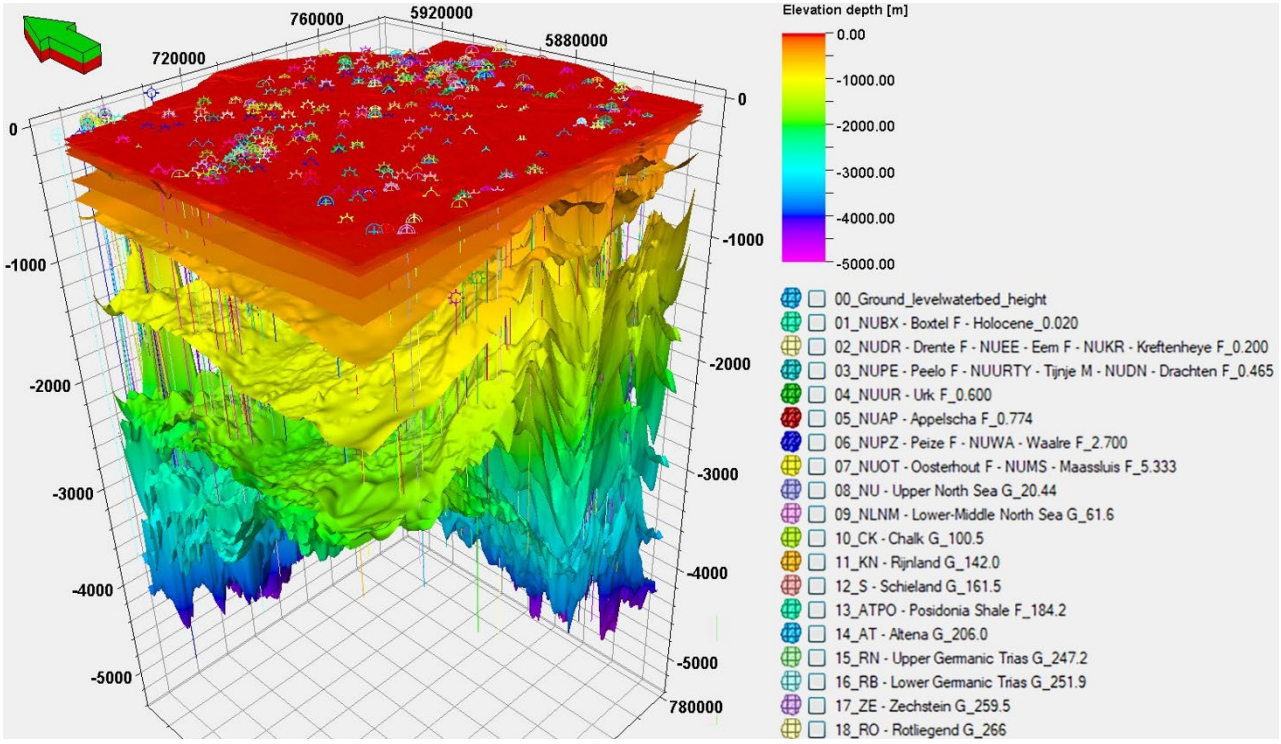

Figure 3-1: 3D representation of the 18 Permian – Holocene layers of the geological model combining DGM Diep 5.0 and DGM (dataset compiled from TNO-GDN, 2019; Hummelman et al., 2019). Horizontal axes are coordinates in the UTM31N(ED50) projection system. Vertical axis is depth in meters. Vertical lines with symbols on top are the deep wells available in the studied area. Stratigraphic horizons represented are listed next to the figure (number, abbreviation, name and absolute age of the base of stratigraphic interval), see the stratigraphic nomenclator of nlog.nl and dinoloket.nl for further details.

The (sub-)basin diapiric evolution has been simulated in the thermal and burial scenario of the northern Netherlands onshore by incorporating a quantitative structural restoration coupled with fluid and thermal flow in the TemisFlow™ software package (Lemgruber-Traby et al., 2020; Nader et al., 2023). This step has created an integrated 3D basin model, accounting for temperature and pressure evolution through time. We have started with an initial 8 layers in the overburden of the Zechstein salt by using the DGM Diep model (v5.0) of the Netherlands (TNO-GDN, 2019). To increase the resolution for the more recent evolution of the salt diapirism we created a higher resolution loading model for the Cenozoic by including the shallow DGM model developed by TNO, publicly available via dinoloket.nl (Hummelman et al., 2019, Figs 3-1 - 3-4). This approach has increased the total number of layers modelled to 18. To model the Upper Germanic Triassic Group with complex facies composition and the Late Cretaceous Chalk Group and Lower North Sea Group with large thicknesses and variable lithological facies, we divided them into sublayers, which increases the total number of layers to 29 (Fig 3-5). Thereby, we obtained the temporal resolution to model the evolution of the rates of salt diapirism through time, with increased resolution for the more recent Pleistocene – Holocene times (Fig 3-6). We use paleobathymetry estimates for the Netherlands (Fattah et al., 2012). However, such estimates are valid for the entire area and do not include lateral variabilities. We used the height of the ground water level as the present-day bathymetry and interpolate between the present-day bathymetry and first paleobathymetry data point in Fattah et al. (2012). Paleobathymetry is used as paleotopography because deposition was submarine before Pleistocene time.

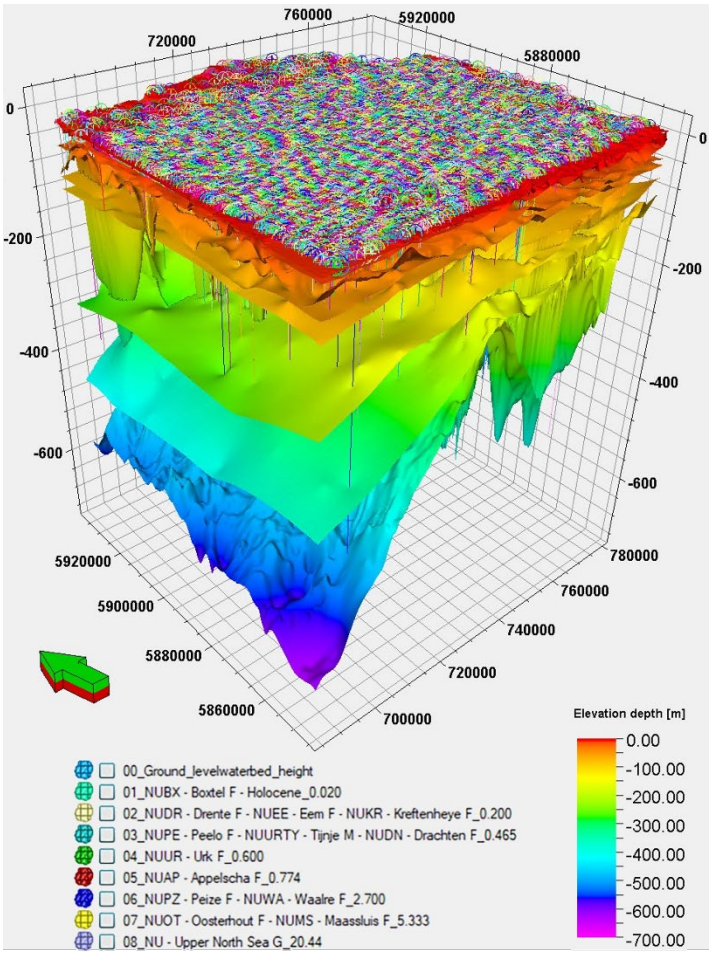

Figure 3-2: 3D representation of the upper 8 Miocene – Holocene layers of the geological model combining DGM Diep 5.0 and DGM (dataset compiled from TNO-GDN, 2019; Hummelman et al., 2019). Horizontal axes are coordinates in the UTM31N(ED50) projection system. Vertical axis is depth in meters. Vertical lines with symbols on top are the shallow wells available in the studied area. Horizons represented are listed below the figures (number, abbreviation, name and absolute age of the base of stratigraphic interval), see the stratigraphic nomenclator of nlog.nl and dinoloket.nl.

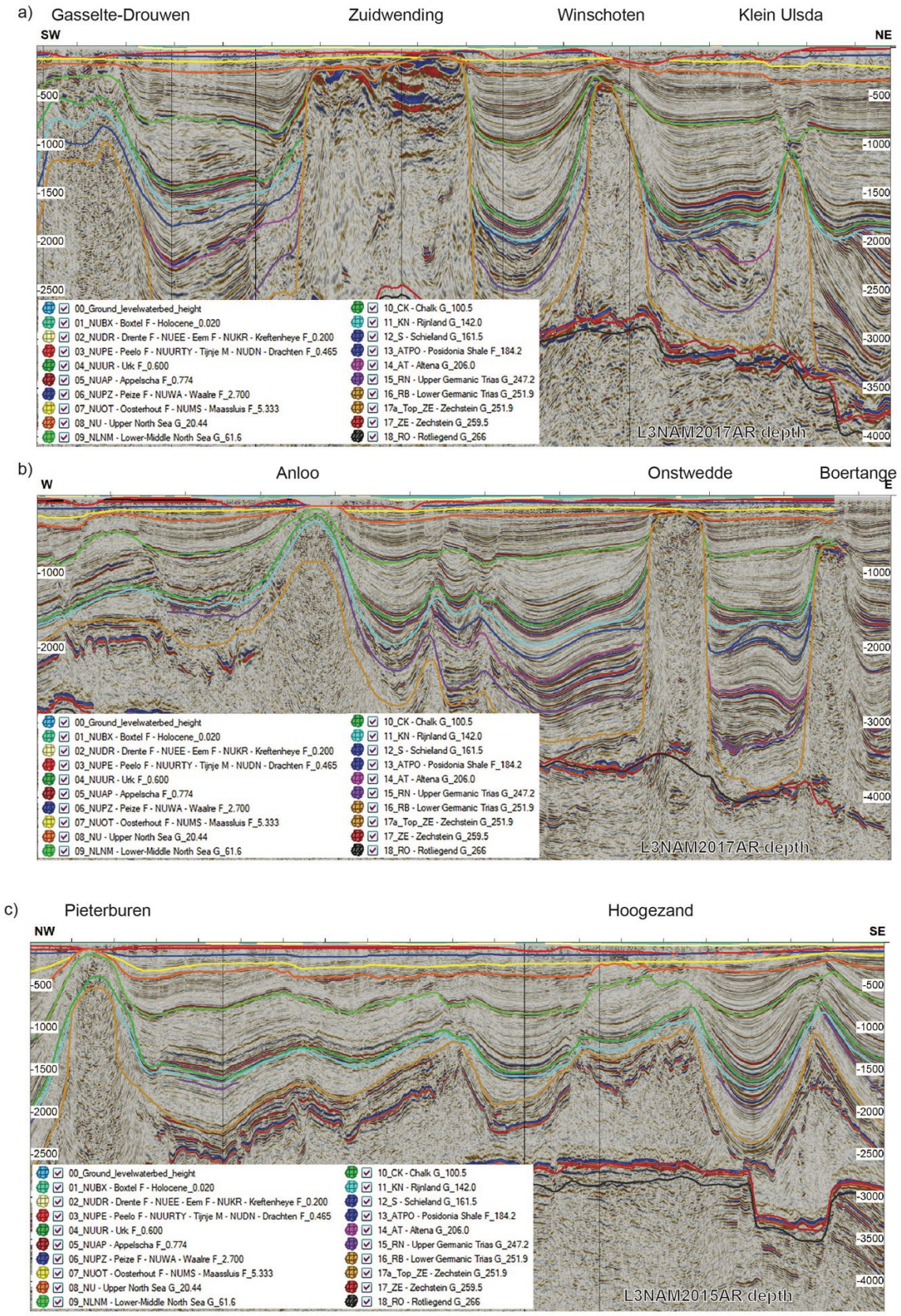

Figure 3-3: Regional cross-sections across the main diapiric structures in the studied area taken from 3D seismic datasets (L3NAM2017AR and L3NAM2015AR, in TVD, see nlog.nl) with the 18 stratigraphic layers used in this study. Location of cross-sections in Fig. 2-1. a) Regional cross -section S1 across the Gasselte-Drouwen - Zuidwending - Winschoten - Klein Ulsda diapiric structures; b) Regional cross -section S2 across the Anloo – Onstwedde - Boertange diapiric structures; c) Regional cross -section S3 across the Pieterburen - Hoogezand diapiric structures.

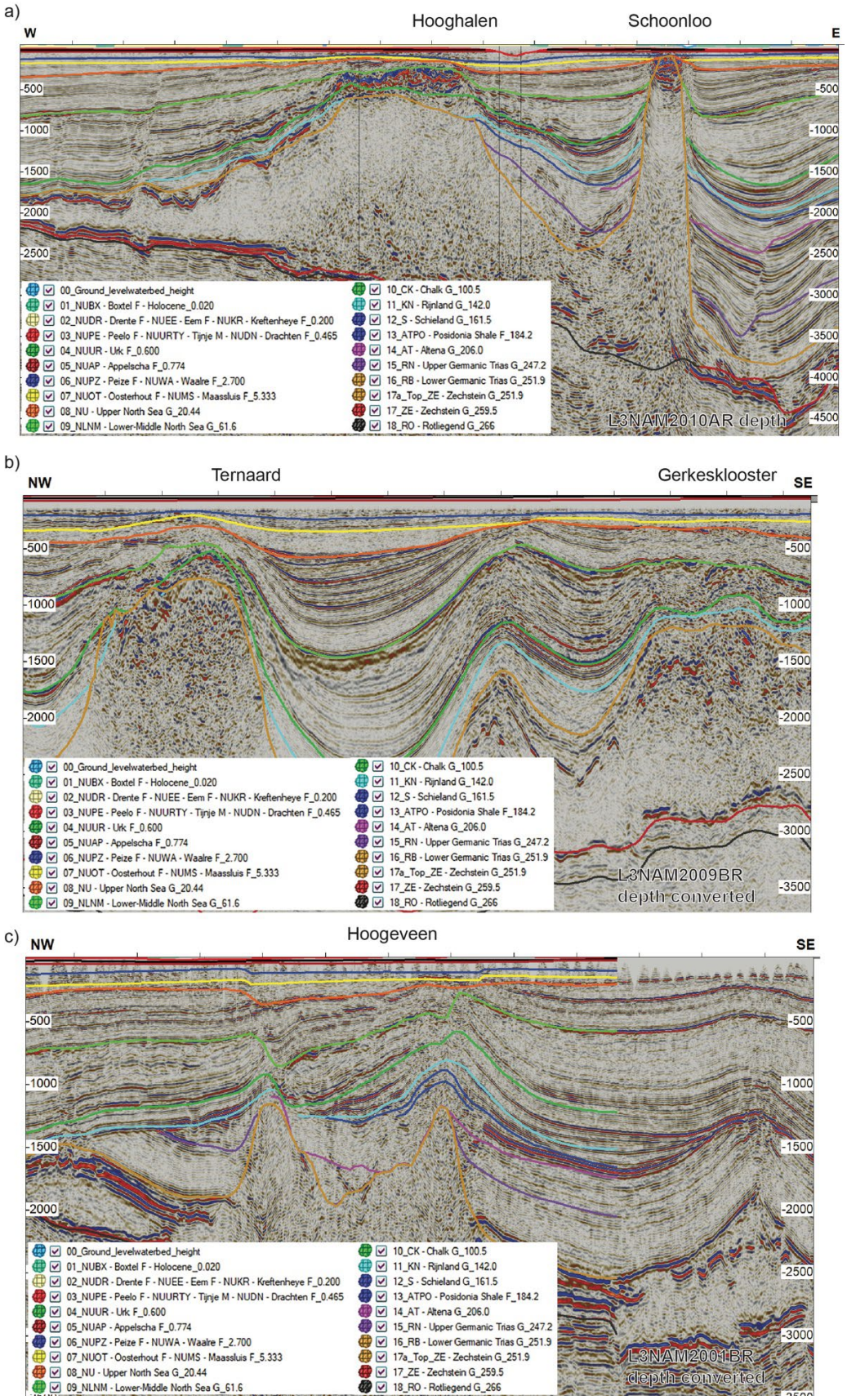

Figure 3-4: Regional cross-sections across the main diapiric structures in the studied area taken from 3D seismic datasets (L3NAM2010AR in TVD, L3NAM2009BR and L3NAM2001BR in TWT converted in TVD by using the Velmod 4a velocity model, see nlog.nl) with the 18 stratigraphic layers used in this study. Location of cross-sections in Fig. 2-1. a) Regional cross-section S1 across the Hooghalen - Schoonloo diapiric structures; b) Regional cross -section S2 across the Ternaard - Gerkesklooster diapiric structures; c) Regional cross -section S3 across the Hoogeveen diapiric structure.

Layer	Group/Formation	Bottom Age (Ma)	Dominant depositional environment	Lithology approximation in TemisFlow	Paleobathemetry (m)
29	NUBX - Boxtel F - Holocene	0.020	continental to deltaic marine	90% sand 10% shale	interpolated
28	NUDR - Drente F - NUEE - Eem F - NUKR - Kreftenheye F	0.200	glacial and continental	50% sand 50% shale	interpolated
27	NUPE - Peelo F - NUURTY - Tijnje M - NUDN - Drachten F	0.465	glacial and continental	50% sand 50% shale	interpolated
26	NUUR - Urk F	0.600	continental	90% sand 10% shale	interpolated
25	NUAP - Appelscha F	0.774	continental	90% sand 10% shale	49
24	NUPZ - Peize F - NUWA - Waalre F	2.700	continental	90% sand 10% shale	93
23	NUOT - Oosterhout F	5.333	marine	70% sand 30% shale	193
22	NU - Upper North Sea G	20.44	marine	50% sand 50% shale	10
21..18	NLNM - Lower-Middle North Sea G	61.6	marine	30% sand 70% shale	147
17..14	CK - Chalk G	100.5	marine	chalk	200
13	KN - Rijnland G	142.0	marine	30% sand 70% shale	0
12	S - Schieland G	161.5	continental to shallow marine	50% sand 50% shale	18
11	ATPO - Posidonia Shale F	184.2	marine	shale	179
10	AT - Altena G	206.0	marine	30% sand 70% shale	0
9	RN - Upper Germanic Trias G	210.1	shallow marine	50% sand 50% shale	20
8		216.3		limestone	18
7		241		sandstone	10
6		245.1		salt	9
5		247.2		50% sand 50% shale	10
4	RB - Lower Germanic Trias G	251.9	continential to shallow marine	90% sand 10% shale	18
3	ZE - Zechstein G	259.5	marine evaporatic	salt	7
2	RO - Rotliegend G	266	continental	90% sand 10% shale	0
1	Pre RO	360	marine	shale	50

Figure 3-5: The separation in stratigraphic units used as an input in the diapirism modelling, with dominant depositional environment, lithologies, paleobathymetry and presence of main sedimentary units, by following the general stratigraphic nomenclature of the Netherlands. Stratigraphy is based on DGM and DGM-deep models (Hummerlman et al., 2019, TNO-GDN 2014, 2019), paleobathymetry is based on Fattah et al. (2012).

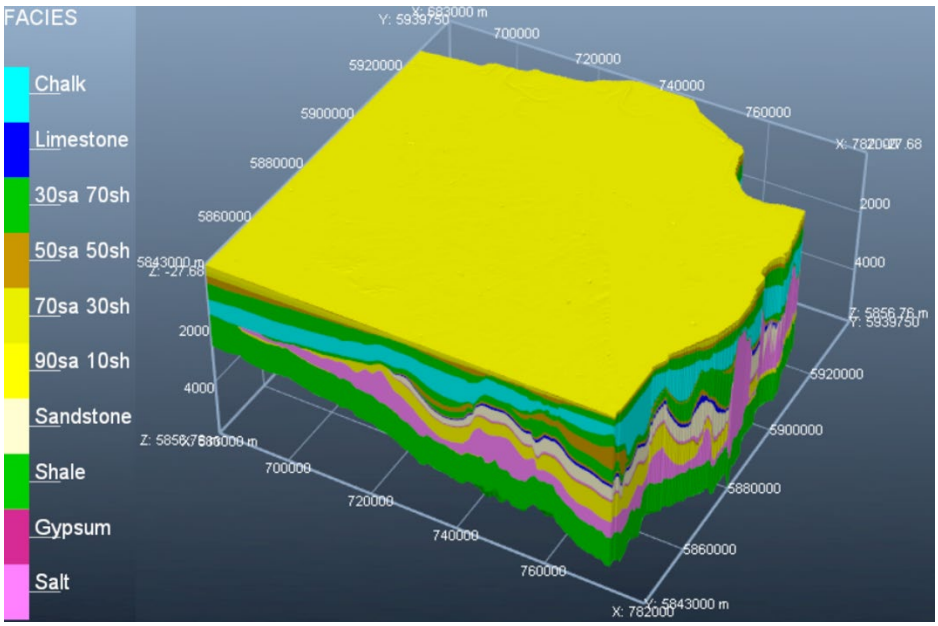

Figure 3-6: Sedimentary model with 29 (sub-)layers. The colors represent the lithofacies explained in the legend.

3.2 Salt restoration

The main modelling approach used for sediment restoration is 3D vertical backstripping, where sedimentary units are sequentially removed from a stratigraphic column using the compaction curves defined for each facies, and the depth of the underlying units is updated in such a way that the model top boundary matches the given paleotopography. The approach allows for the recovery of the basement subsidence and uplift history. It takes into account the decompaction of the remaining sequence following each stage of the backstripping, as well as the changes in sea level and bathymetry. At each step of the backstripping, TemisFlow™ removes a stratigraphic layer and calculates the decompacted sediment thickness in a multi-1D fashion. This method does not change sediment thickness (except for decompaction) in any vertical column. Due to the density and viscosity of salt, salt can move from the vertical column where it is deposited to form diapirs and withdrawal basins. With the presence of salt, salt restoration needs to be combined with standard backstripping method in such a way that the salt thickness can be flexibly adjusted to obtain physically reasonable results.

Without accounting for diapirism in the restoration, the salt would form downward-pointing structures after backstripping because this method does not account for lateral salt movement (Fig 3-7). To remove these artefacts and account for diapirism, additional steps must be employed. Because sedimentary layers in non-diapiric regions are continuous without folding or strong thickness variations, the diapirism in the study area is local, without large-scale regional salt movements. This inference means that the salt thickness obtained by one diapir comes from its surrounding withdrawal basin, allowing to correct the artefacts of the downward-pointing structures. The modelling keeps the total salt volume constant through time. The net salt volume changes due to influx or outflux through the lateral boundary, while erosion and subrosion is neglected.

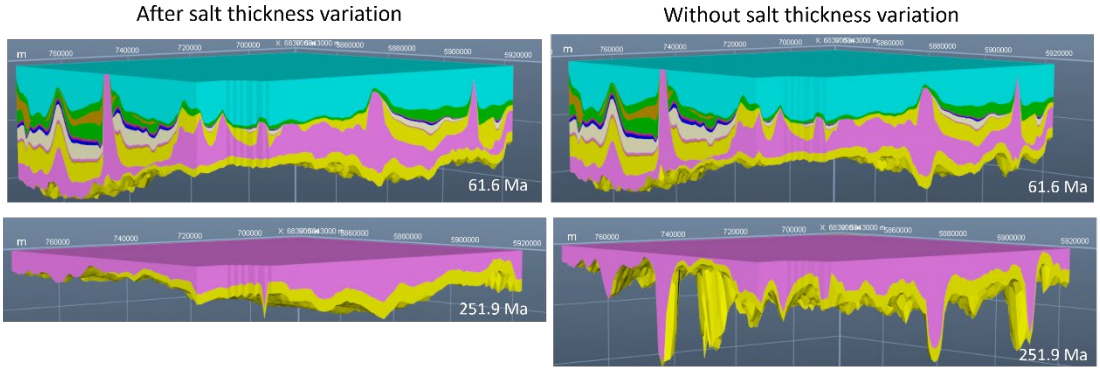

Figure 3-7: Backstripping method is combined with salt restoration to obtain correct salt structures. The figure shows two representative cross-sections that are perpendicular to each other, with and without salt thickness correction. See Fig 3-6 for the lithostratigraphic legend.

Another important constraint comes from the observations of stratal geometries around the main salt domes. The seismic interpretation shows that the major piercing events, when salt truncated the layers in the overburden, took place in the Late Cretaceous – early Paleogene during the deposition of the Chalk Group (Fig. 3-3, 3-4). This interpretation shows that although the diapirism was a continuous process that started already during Triassic times, as observed by the syn-kinematic deposition in the rim synclines, the salt piercing into the overburden took place dominantly during the Late Cretaceous – Paleogene basin inversion stage. Standard multi-1D backstripping method cannot take this into account since the removed overburdening sediments due to salt piercement are not considered. This results in much faster diapir growth before Late Cretaceous and an underestimated diapirism during Late Cretaceous (Fig 3-8A). To reconstruct the piercing events, the removed sediments overlying the diapirs need to be reconstructed. First, a standard backstripping with salt restoration is conducted. We subsequently calculate the sediment thicknesses to be added by interpolation of the sediment thickness of each layer around the diapirs right before the Chalk Group deposition (around 100 Ma). Finally, backstripping is repeated to obtain the correct decompaction of the added thicknesses back to their time of deposition. After correction, the artefacts of diapiric structures already risen to the surface in Triassic and Jurassic times were removed. The corrected diapiric structures are modelled to be buried at depth until the Late Cretaceous times (Fig 3-8B).

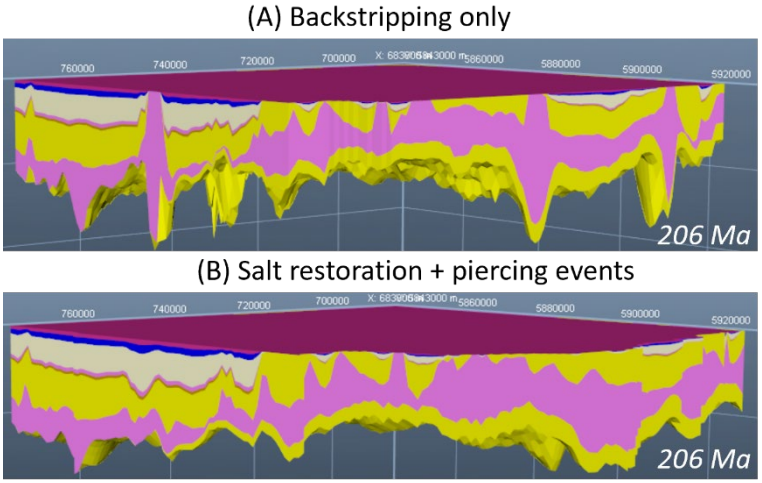

Figure 3-8: Representative cross sections showing non-realistic salt structures at 206 Ma that are removed after salt restoration and the piercing events are accounted in Late Cretaceous times. See Fig 3-6 for the lithostratigraphic legend.

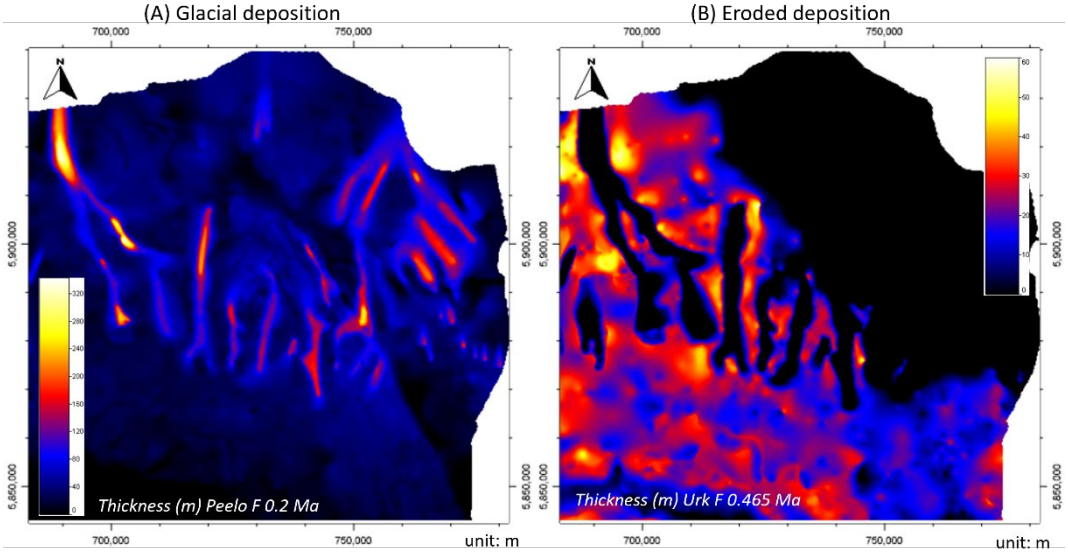

Figure 3-9: (A) Glacial deposition in Peelo formation (0.2 Ma) and (B) eroded sediments in Urk formation (0.465 Ma).

The glacial erosion that took place in Pleistocene times (Peelo and Drenthe formations) required further corrections. Tertiary sediments were significantly eroded and replaced by thick sequences (over 300 m) of glacial and post-glacial sediments (Fig 3-9). The eroded thickness until the top of erosional channels was added before the time of the glacial event to obtain the correct loading and buried depth for salt diapirs. Without this correction, the diapirs appear to have been at shallower depths before Pleistocene times. This incorrect diapiric growth and collapse results in overestimates for both the diapirism rate before Pleistocene and the subrosion rate afterwards. We corrected the eroded thickness in the same manner as with the piercing events, by restoring the original thickness of sediments observed on the flank of the glacial erosional channels. After adding back the eroded sediments, the diapirism rate is reduced, resulting in realistic geometries (Fig 3-10).

The last step in our correction procedure is accounting the sub-salt fault offsets truncating the Rotliegend strata (Fig 3-11A). These faults formed in several tectonic events starting with the Permian times, but the large offsets were acquired during the Triassic – Early Cretaceous extensional evolution affecting the larger Southern North Sea Basin. We implemented these offsets to be ultimately established at the end of the Early Cretaceous time, while being gradually restored earlier (Fig 3-11).

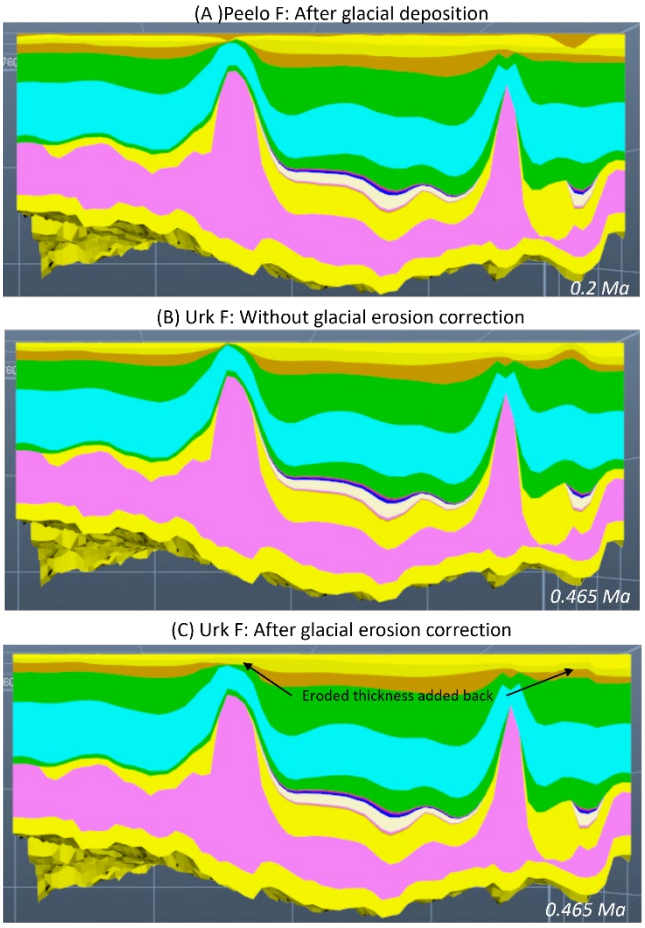

Figure 3-10: Non-realistic diapiric evolution and sediment geometries (0.465 Ma) are removed after glacial erosion correction. The figure shows a representative cross-section. Refer to Fig 3-6 for the stratigraphic table.

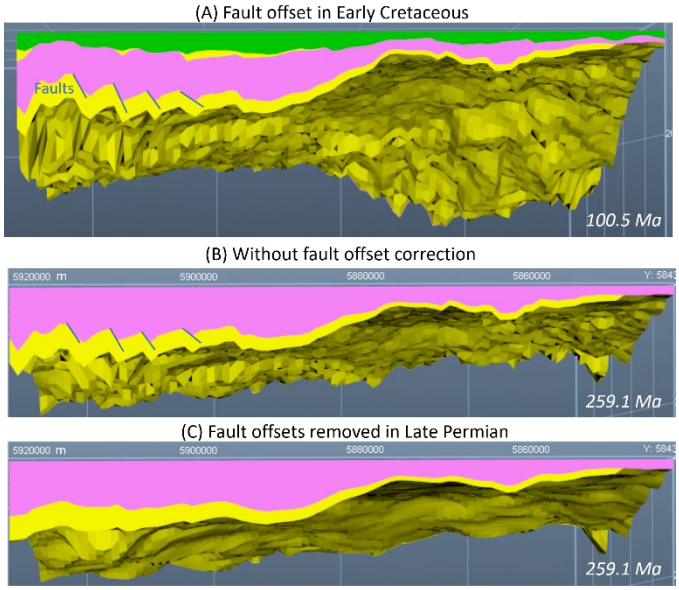

Figure 3-11: Fault offsets implemented gradually starting with Triassic times. The figure shows a representative cross-section. Refer to Fig 3-6 for the stratigraphic table.

3.3 Simulation method

After backstripping, the model can be used to simulate the fluid flow and heat transfer. These modelling outputs are compared with existing observations and literature data to calibrate the model setup and parameters. After calibration, the simulated temperature and Darcy velocity profiles are used as a reference to build the subrosion model. To simulate better the fluid flow and heat transfer, we have extended the sedimentary model to lithospheric scale to prescribe the correct thermal boundary conditions (Fig 3-12). We added upper crust, lower crust and upper mantle layers below the sediments to model down to the lithosphere-asthenosphere boundary at 100 km depth. The crust thickness is based on the EuCRUST-07 model (Tesauro et al., 2008), with an average thickness of upper crust of 13 km and lower crust 20 km. A rifting event is modeled in Jurassic and Early Cretaceous (161.5-100.5 Ma), with a low stretching factor β = 1.1 that approximates best the cumulative offsets over the platforms and troughs areas. Simulations of heat and fluid flow are conducted using the Visco simulator in TemisFlow™. The surface temperature and the temperature at the lithosphere-asthenosphere boundary are kept constant at 10 °C and 1330 °C, respectively. Lateral boundaries are set to be hydrostatic for fluid flow and no flux for heat flow.

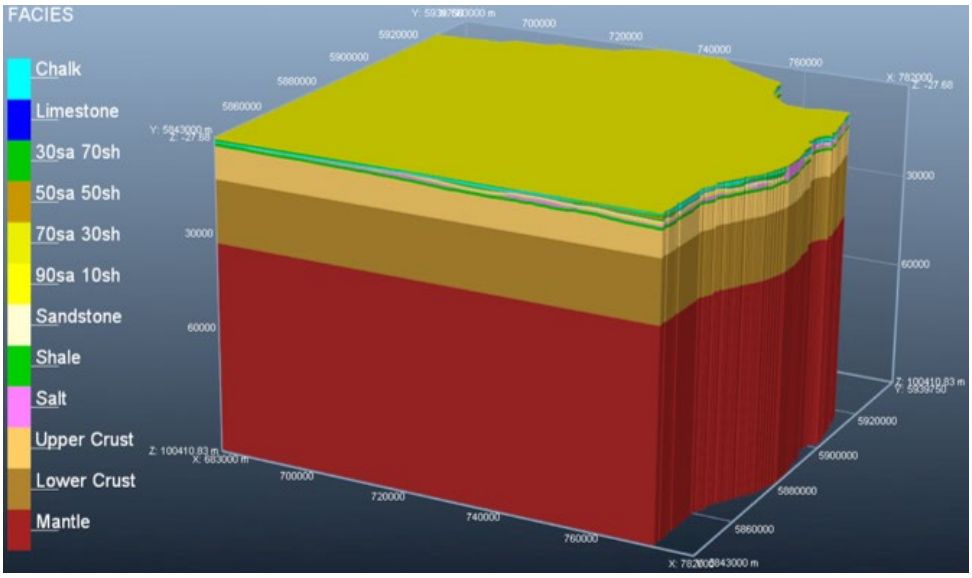

Figure 3-12: Extended model with crust and upper mantle for heat and fluid flow simulations.

3.4 Calibration method

We first use temperature and porosity data to calibrate our model. Model properties and parameters are corrected in places where there is a mismatch between data and model output. Subsurface temperature data from the onshore Netherlands are available on the Dutch Oil and Gas portal (http://www.nlog.nl) and on the Dutch Geothermal Platform (https://geothermie.nl). These temperature measurements are based on Bottom Hole Temperature (BHT) data and Drill-Stem Tests (DST). The temperature dataset used were corrected by Bonte et al (2012) and are expected to have an error margin of 8-10 °C. This high-accuracy dataset contains 193 measurements from 83 wells in the study area. For comparison we picked up 26 wells where multiple measurements at various depth are available (Fig 3-13). GTV-01 and STK-01 are along the Onstwedde-Anloo cross-section. Other wells are distributed on Lower Saxony Basin, Lauwerszee Trough and Friesland Platform. In general, the temperatures inferred by modeling and those from well logs match within the error margin. The comparison for the two wells GTV-01 and STK-01 along the Onstwedde-Anloo cross-section shows good match, indicating the validity of the model in the diapir-dense region (Fig 3-14). There is a general

trend of underestimation by a few °C for many wells in the deep region, but the differences are within or around the same magnitude of the error margin.

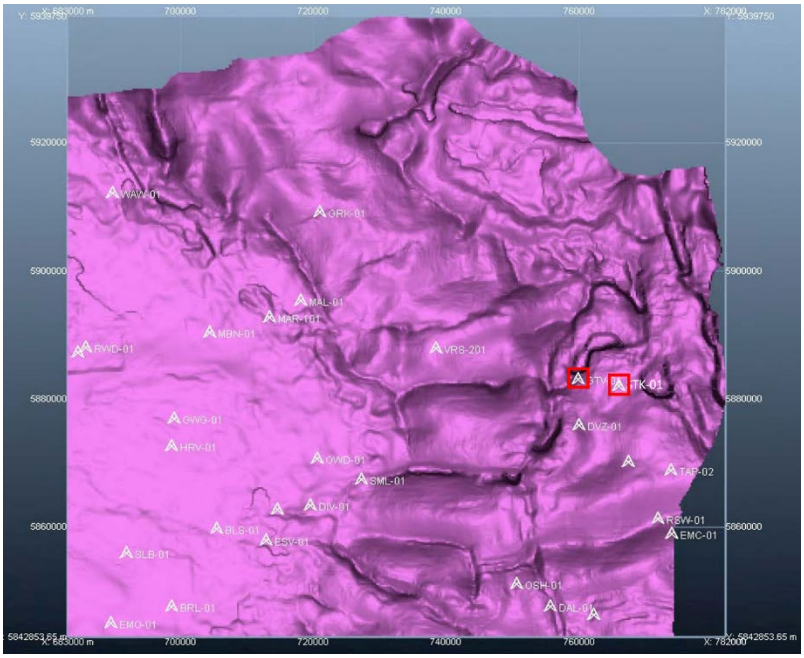

Figure 3-13: Location of the wells documented in Bonte et al. (2012), with the depth of the salt top (purple) as background. Wells GTV-01 and STK-01 used in Fig 3-14 are highlighted in red boxes.

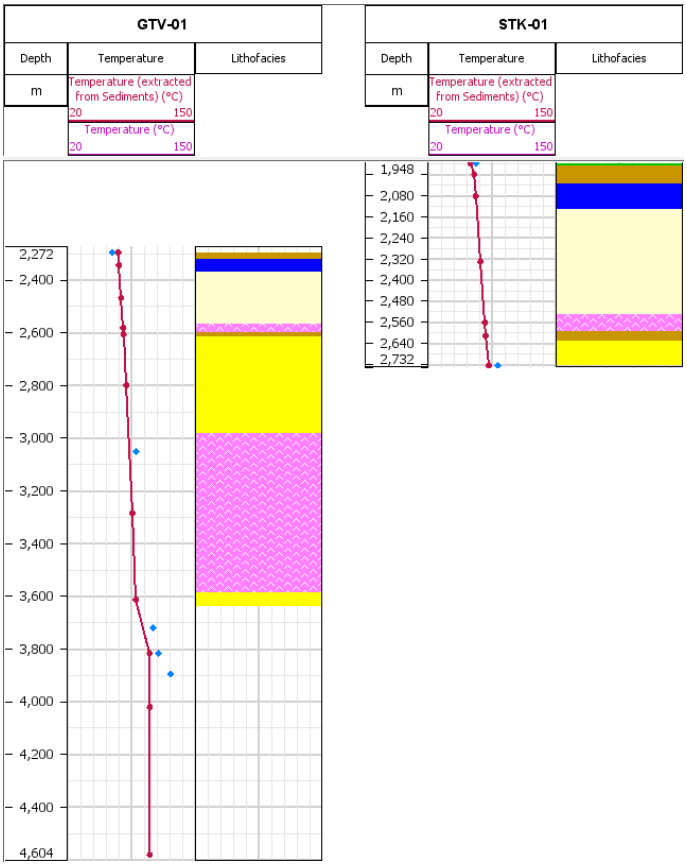

Figure 3-14: Calibration of the temperature profile against well logging from wells GTV-01 and STK-01, which are located along the Onstwedde-Anloo cross-section. The simulation results are shown in red and the well measurements in blue. The lithofacies codes are displayed in the legend of Fig 3.6.

Porosity and permeability data for the Paleozoic - Mesozoic main reservoirs are available from the LogQM dataset (Vis et al., 2010), where the 15 available regional distributions of reservoirs (https://www.nlog.nl/en/reservoir- characteristics) were truncated and re-gridded to the geometrical voxels dataset. We compared our simulated porosities in the Rijnland Group, Upper Germanic Triassic Group, Lower Germanic Triassic Group and Rotliegend Group reservoirs to calibrate the model. We found that the simulated porosity ranges in Upper and Lower Germanic Triassic reservoirs are higher than the ranges in the dataset. The overestimate is everywhere inside the reservoir and sometimes up to 10 percentage points. This difference is a result of the mechanical properties of the generic sandstone in TemisFlow™, which is different from similar rocks observed in the northeast Netherlands. The inconsistency was resolved by modifying the sandstone's depth dependency of porosity to fit the observation data (e.g., Geluk et al., 1997). After the calibration, the simulated porosities are all in the ranges of the collected porosity data, with the largest difference less than a few percentage points. Figure 3-15 shows the comparison between the simulated and collected porosity maps for the major reservoir layers above and below Zechstein salt.

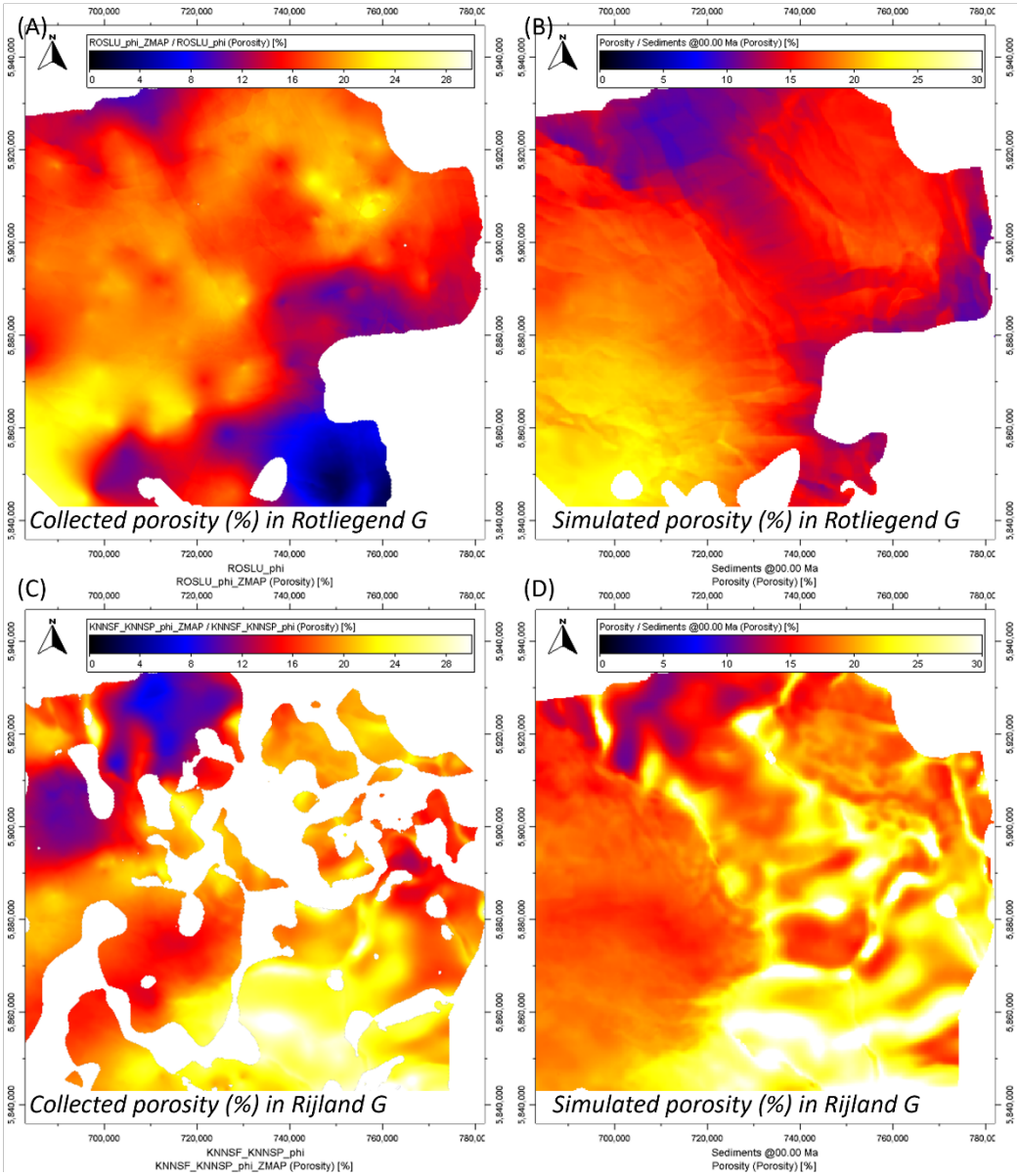

Figure 3-15: Calibration of the simulated porosity maps (B,D) against collected data (A,C) for the reservoirs in Rijnland Group (KN, C-D) and Rotliegend Group (RO, A-B).

4 3D basin modelling results

The geometry of present-day diapirs is constrained by the base and top maps of the Zechstein group based on seismic imaging. The depth of the base of the Zechstein deposits varies significantly, ranging from around 2 km to 5 km in the studied area (Fig 4-1). The Zechstein salt is shallow on the Groningen and Friesland platform, deeper on the Lauwerszee Trough and the deepest in the Lower Saxony Basin (Fig 1-2, 2-1). The fault system shows a major trend in the NW-SE direction, following the orientation of the Lauwerszee Trough. E-W oriented faults connect the NW-SE oriented ones inside and around the trough, and N-S oriented faults in the Lower Saxony Basin near the NL-Germany boundary. The top Zechstein depth map depicts the major diapirs (Fig 2-1). The salt thickness on the Friesland platform can be thinner than 100 m, while elsewhere the thickness is on average 1 km. Generally, the thickness of the salt increases from SW to NE, where it is dominated by highly deformed salt structures, including pillows, domes, and diapirs. The thickness of the large diapirs, such as Zuidwending or Onstwedde, is over 3500 m while the surrounding syn-kinematic deposition in withdrawal basins is typically in the order of 100-300m meters. The geometry of diapirs shows a very good connection to the fault system affecting the underburden. Typically, salt migrates in the footwall of normal faults, forming larger diapirs in places where the offset is higher, a result of higher differential loading. Often, a salt wall aligns with a fault zone, linking individual salt structures together (Fig 2-1). For instance, the Groningen Platform features a ring of salt diapirs and pillows connected by shallower salt walls, which follow the major bounding fault zones. Toward the center of the high, there is a ring of salt withdrawal basins, followed by another ring of smaller salt pillows in the core of the high. The boundary between the Friesland Platform in the west and the Lauwerszee Trough in the center of the northern Netherlands is marked by several NW-SE trending salt pillows, walls, and diapirs aligned along the fault zones. The Waddenzee area, which spans the onshore-offshore transition, is another diapiric region with more mature salt structures (Strozyk et al., 2014).

The salt structure evolution of the 14 diapirs in northeast Netherlands, gathered along 6 seismic sections S1-S6 in Fig 2-1, is presented in Appendix Figs A-1~A-6. We focus our detailed discussion on the evolution of four representative diapirs, i.e. Zuidwending, Onstwedde, Anloo and Ternaard, with the first three closest to the surface and Ternaard located in the offshore Waddenzee. All other shallow diapirs show a similar evolution. These diapirs have a thickness of minimum 2 km and have variable geometries (Fig 4-1). Zuidwending is the diapir closest to the present-day surface (Fig 4-1A). It is a twin diapir with a narrow connection. The top of the diapir reaches a depth of 200 m below the surface with a vertical thickness of up to 3000 m. It pierced out the Triassic to Cretaceous sediments and forms an unconformity with the Neogene sediments. The base of the diapir is almost flat at the depth of 3000 m, with one major fault below salt at the northeast end. Onstwedde is another large diapir that has a thickness of over 3500 m and reaches slightly below 200 m from the surface (Fig 4-1B). It has a cylindrical shape, with a radius of around 2 km. It has a main fault at the base towards the east end. It is located in a fault-dense area with many small diapirs in the vicinity formed above the faults. Anloo is broad compared to the other diapirs, and increased salt thickness continues towards the west until the major fault line that defines the boundary of the Lauwerszee Trough (Fig 4-1B). It thus has an elongated shape in the W-E direction. The top of the diapir does not pierce any sedimentary elements deposited later, but still reaches 1 km below surface. Its base is on top of a series of small faults, making this region very active for salt movements. Fault activities are also active in the overburden along the Anloo-Onstwedde section. Ternaard reaches 800 m below surface and has an elongated shape along an N-S orientation (Fig 4-1C). It pierces through the Triassic sediments and affects sediments as young as the Paleogene. It has very thin withdrawal basins to the east and west side and a base with long wavelength depth variation.

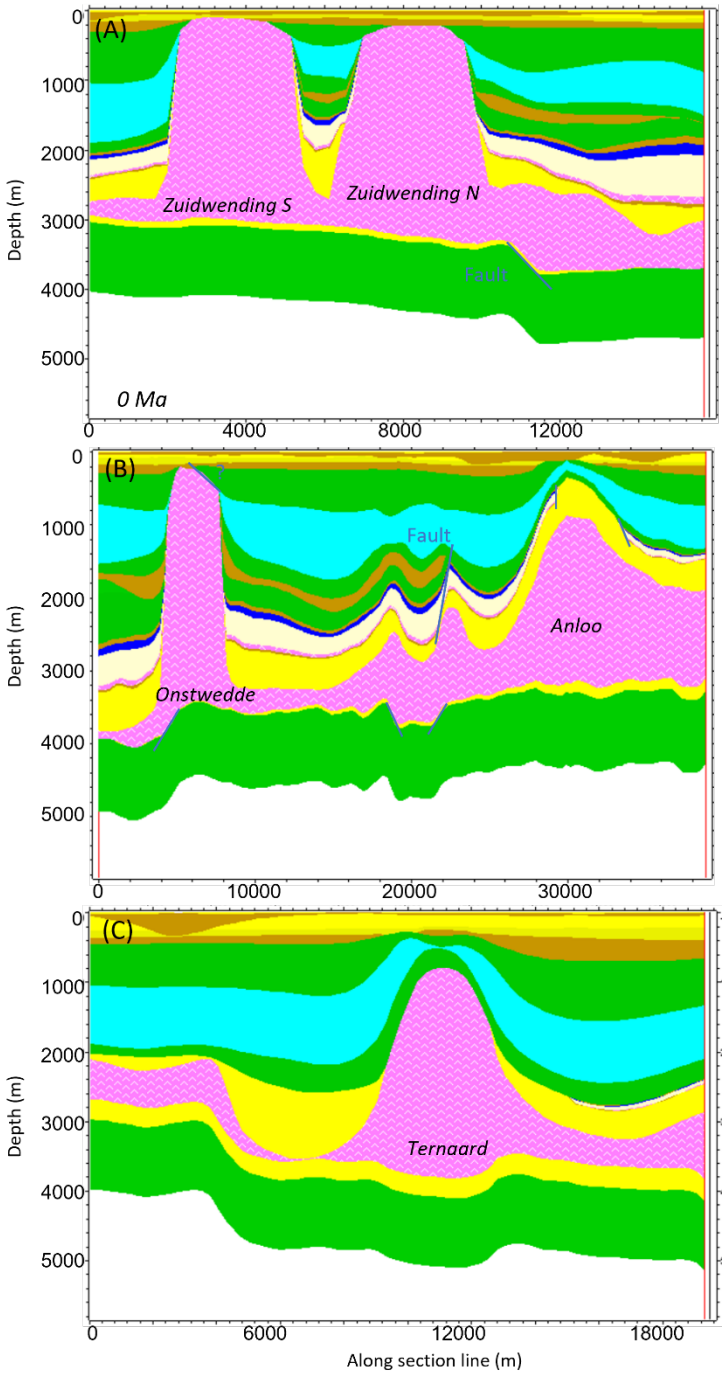

Figure 4-1: The present-day model geometries across the diapirs Zuidwending, Onstwedde, Anloo and Ternaard, simulating the structure observed in the interpreted seismic sections S1, S2 and S5 in Fig 2-1. The main faults are plotted with blue lines. See Fig 3-6 for the lithostratigraphic legend.

4.1 Diapirism per age

The thickness variations observed in the input lithostratigraphical model are used to determine whether salt movement has taken place during a specific age (Fig. 4-2). When thickness of a sedimentary layer varies significantly in the regions around the diapir, it is more likely that diapirism was active and contributed to the evolution of the withdrawal basins. When there are no thickness variations of a sedimentary layer across the diapir, the salt was likely not active and the missing overlying sediments could be removed later in a piercing event. These considerations were used in

deriving the evolution of all 14 main diapirs, resulting in calculations of the diapirism rates (Table 4-1).

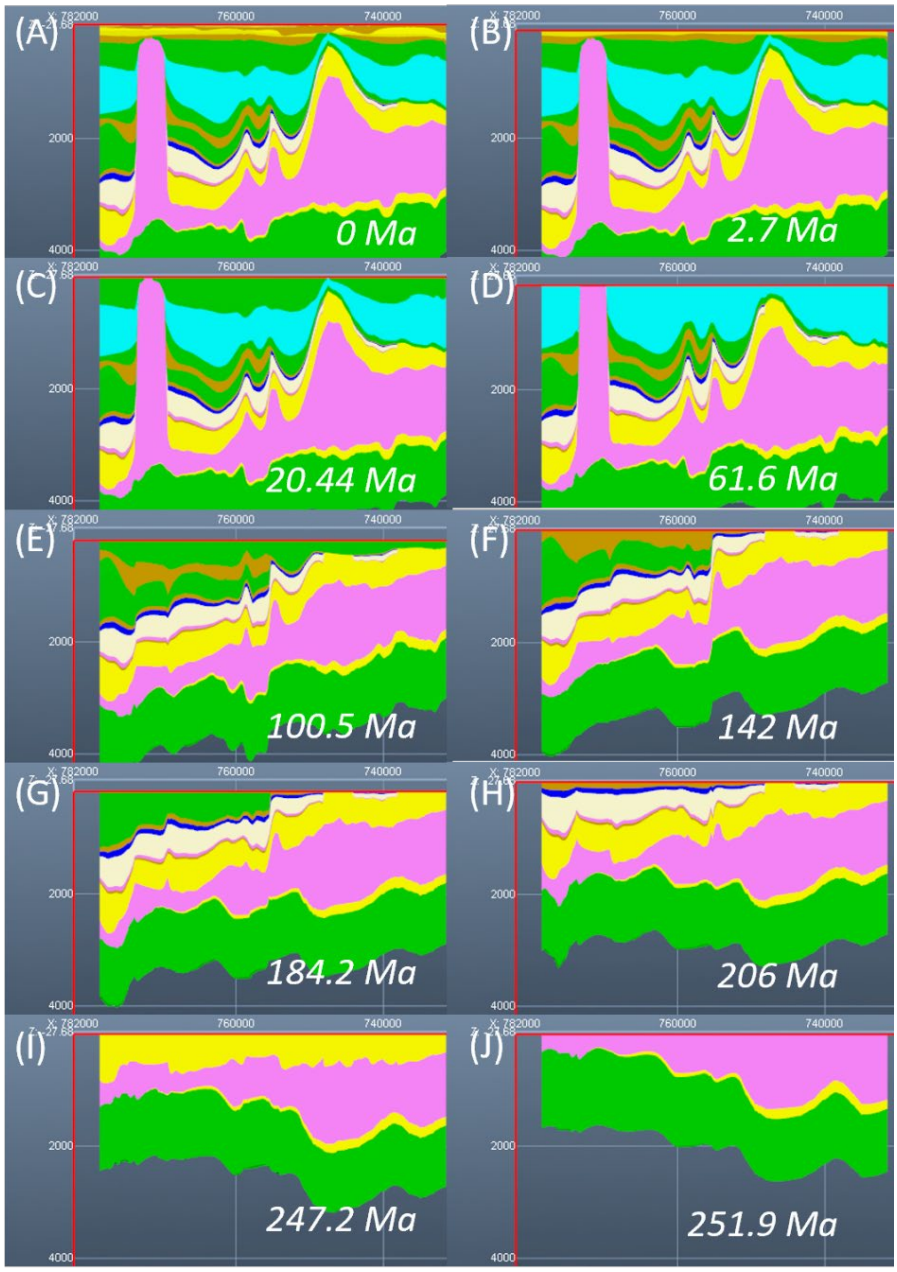

Figure 4-2: Salt evolution (251.9 Ma – 0 Ma) along the cross-section Onstwedde-Anloo (5x vertical exaggeration).

Early Triassic The Lower Germanic Triassic Group (RB) has a similar thickness around many diapirs including Zuidwending, Onstwedde and Anloo (Fig 4-1AB). Above Anloo, the RB forms a continuous deposition without interruption. These geometries indicate that no significant salt movement took place during the deposition of this stratigraphic interval. However, other locations such as Ternaard (Fig 4-1C), strong variation in the RB thickness are observed, indicating that the diapirism has been activated shortly after the deposition. The RB sediments are missing for the large diapirs Zuidwending and Onstwedde. As these sediments could have been removed later by erosion, it is unclear how large the diapirism was in Early Triassic times. However, since the RB thickness next to the diapir flanks is often thinner than at distance, a low amount of salt redistribution is inferred (Fig 4-2I).

Late Triassic The Upper Germanic Triassic Group (RN) has no thickness variations for many diapirs such as Zuidwending and Onstwedde, indicating the absence of significant amount of salt movements

(Fig 4-1AB). The RN sediments are missing around Ternaard, indicating either no deposition or later erosion (Fig 4-1C). The RN sediments are very thin above Anloo and gradually thin towards the center of the diapir, indicating active diapirism (Fig 4-1B). The RN also misses a tabular unit. Combining this observation with the thickness variation of RB for the small diapirs to the east (Between Anloo and Onstwedde), we interpret this absence to be related to Late Triassic faulting events (Fig 4-2H).

Jurassic The Jurassic deposits (Altena Group AT and Schieland Group S) are limited to the Lower Saxony Basin in the southeast, while elsewhere these deposits are thin or missing, such as along the flanks of the Ternaard and Anloo structures. A fault separates the presence of the Jurassic deposits between Anloo and Onstwedde (Fig 4-1B, 4-2FG). If no significant erosion is assumed, then the diapirism appears to be less significant during this time interval.

Late Jurassic - Early Cretaceous The relatively low amplitude (tens to few hundreds of meters) of thickness variations in the the syn-kinematic deposition observed in the Rijnland Group (KN) is in agreement with our model, demonstrating low-amplitude salt movements. However, many of the faults below the salt layer have continued their extensional evolution during the Late Jurassic and Early Cretaceous (see also Pharaoh et al., 2010). The fault offsets generated below salt induced subsidence in the post-salt Triassic sediments, resulting in differential loading. Therefore, the activity of these faults triggered later salt movements. The result is that many large salt pillows and diapirs formed next to the deeply subsided Triassic basins or rafts (Zuidwending, Onstwedde and small diapirs near Anloo, Fig 4-1, 4-2E).

Late Cretaceous – Early Paleogene. The thick Chalk Group (up to 1 km) implies coeval tectonic subsidence. The onset of inversion by switching from extension to shortening triggered thick-skinned reactive diapirism of salt pillows, leading to large-scale folding of the overlying sedimentary units. This process caused differential uplift and subsidence, with thicker sediments accumulating in rim synclines and thinner sediments forming above the salt diapirs. As a result, large thickness variations over the diapirs are observed. Salt is thin to absent over diapirs, while thick withdrawal basins are formed around the diapirs. This is clearly observed for Onstwedde and Zuidwending, where the CK is furthermore pierced by both diapirs (Fig 4-1, 4-2D). Anloo and Ternaard did not pierce the CK group, but diapirism caused substantial thinning over the diapirs. Due to inversion and uplift, the Cretaceous sediments above the diapirs have been also eroded, creating an unconformity at the Cretaceous-Paleogene boundary, such as in Ternaard.

Paleogene and Neogene Diapirism continued in the Paleogene, as observed by syn-kinematic sedimentation in withdrawal basins (Lower and Middle North Sea group). Large diapirs such as Zuidwending also pierced through this stratigraphic unit (Fig 4-1, 4-2BC). An unconformity is formed with the upper Neogene deposits. This continuation can be explained by passive diapirism, or a subsequent erosion that removed deposits over the diapirs. The latter is supported by the observation of Anloo and Ternaard, where such an unconformity is observed. This unconformity is also an indicator that salt diapirism has largely slowed down during the Neogene (Li et al., 2012). Neogene sediments are mainly thin undeformed layers, indicating slow subsidence and less tectonics (Fig 4-1,4-2B). In the studied area, most salt diapirs are confined within Cretaceous sediments and are covered by slightly deformed to undeformed Paleogene and Neogene sediments. However, some of the larger salt diapirs, such as Zuidwending (Fig 4-1A), continued to deform and could have reached (fairly close to) the surface and formed an unconformity with overlying Pliocene - Pleistocene sediments.

Pleistocene glaciations The Pleistocene glaciations (MIS 5 and MIS 12, Drenthe and Peelo

formations) have imprinted a large erosional relief in the subsurface of the northeast Netherlands (Fig 3-9). The earlier Neogene - Pleistocene sediments were eroded and replaced by thick sequences (over 300 m) of glacial and post-glacial sediments (Fig 4-3). This process has generated differential loading and reactive diapirism, well documented in the neighboring Germany (Lang et al., 2014). The post-glacial isostatic rebound (whether elastic or viscous) would promote differential loading. Despite the significant effects in the subsurface, our modelling results display no significant effects in salt diapirism in the studied area (Fig 4-3C vs. 4-3D). Our modeling results do not show evidence that the salt diapirs have moved significantly after the glacial erosion.

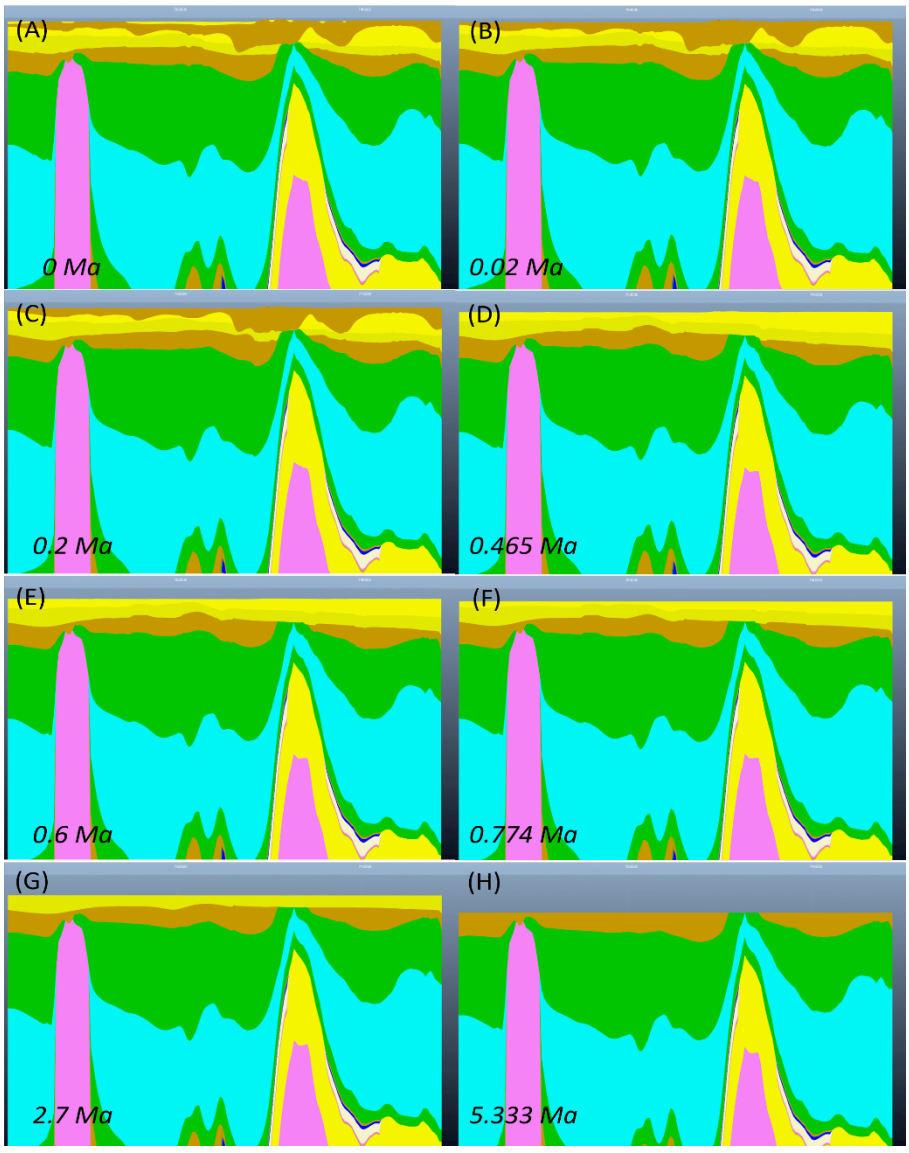

Figure 4-3: Shallow salt evolution in the Quaternary (5.333 Ma – 0 Ma) along the cross-section Onstwedde- Anloo with increased temporal resolution (20x vertical exaggeration).

4.2 Diapirism rate calculation

We calculate the net diapirism rate of all the 14 representative diapirs (Table 4-1), where peaks of the diapirs are chosen as representative (gray circles in Fig 2-1). For the four diapirs Anloo, Onstwedde, Zuidwending and Ternaard explained above, we also quantify their evolution in detail (Fig 4-1). We use two methods to calculate the diapirism rate, based on the modelled burial history (Fig 4-4). For Zuidwending, we picked both the peaks on the south and north sides for comparison. For Ternaard, we picked a location offshore to compare with the other onshore diapirs (rimmed gray circles in Fig 2-1).

Table A-1 Diapirism rate of the 14 diapirs in the northeast Netherlands per age.

Diapirism rate (m/Myr)	NUBX	NUDR	NUPE	NUUR	NUAP	NUPZ	Quaternary Average
Anloo	228.39	3.67	78.06	61.58	-44.36	-3.05	7.68
Gasselt-Drouwen	34.30	-0.94	-113.74	9.98	-28.46	-2.53	-13.84
Gerkesklooster	-163.06	1.11	19.48	-33.82	1.73	-5.95	-5.16
Hoogeveen	124.64	-6.70	-6.81	-2.92	-7.56	-13.45	-10.42
Hoogezand	-244.46	-12.49	-103.30	1.89	-8.76	11.54	-4.80
Hooghalen	8.24	1.94	2.42	-26.63	-24.04	-0.44	-2.79
Klein Ulsda	16.08	0.35	-13.86	-0.25	-27.08	-10.22	-10.22
Onstwedde	-344.14	-12.26	-35.89	0.53	-55.71	-7.21	-15.46
Pieterburen	-168.36	25.33	360.92	0.55	-41.08	-0.40	32.35
Schoonloo	-35.47	1.63	-83.60	-27.20	-94.10	-13.24	-25.00
Ternaard	-131.95	-6.05	83.02	-66.44	-19.30	-6.01	-2.34
Winschoten	20.36	0.84	-10.28	1.55	-38.30	-2.87	-5.16
Zuidwending N	-384.77	-8.81	-61.96	2.63	-34.97	-3.42	-13.92
Zuidwending S	-212.89	19.52	-90.65	2.24	-20.81	-3.21	-12.49

Diapirism rate (m/Myr)	NUOT	NU	NLNM	CK	KN	S	ATPO	AT	RN	RB
Anloo	-8.60	2.49	1.27	20.18	-3.24	-0.02	0.01	0.11	2.34	23.69
Gasselt-Drouwen	-3.11	-2.17	3.77	64.81	-2.13	-1.56	-5.61	1.22	-2.88	46.08
Gerkesklooster	-1.87	0.63	1.65	10.63	2.01	-0.02	0.01	0.11	0.01	11.33
Hoogeveen	-1.49	-5.06	-3.19	20.15	5.73	-0.02	-0.67	-3.74	1.17	34.29
Hoogezand	-3.63	-0.99	2.44	12.62	-1.42	-0.02	0.01	0.11	0.01	-9.73
Hooghalen	-3.60	2.61	2.59	31.53	1.02	-0.02	0.01	0.11	0.55	13.28
Klein Ulsda	-10.35	-1.48	-7.03	50.92	-2.69	-0.02	-0.09	-1.16	6.66	-9.91
Onstwedde	-18.20	0.31	4.54	71.16	0.17	1.82	-0.19	-0.87	-0.02	37.24
Pieterburen	-16.41	3.98	3.91	25.37	-3.06	-0.02	0.01	0.11	0.01	31.35
Schoonloo	5.43	2.07	5.63	67.66	4.86	8.68	0.01	-1.98	-2.13	46.87
Ternaard	-2.67	0.51	6.08	38.66	-1.43	-0.02	0.01	0.11	0.01	23.21
Winschoten	-8.16	0.89	3.07	52.43	-0.95	-4.79	0.01	1.65	2.17	6.11
Zuidwending N	-5.79	6.00	9.41	55.46	2.44	0.74	2.33	0.09	-0.81	16.49
Zuidwending S	-8.75	-1.96	5.71	58.44	1.07	2.92	0.01	2.28	0.46	1.15

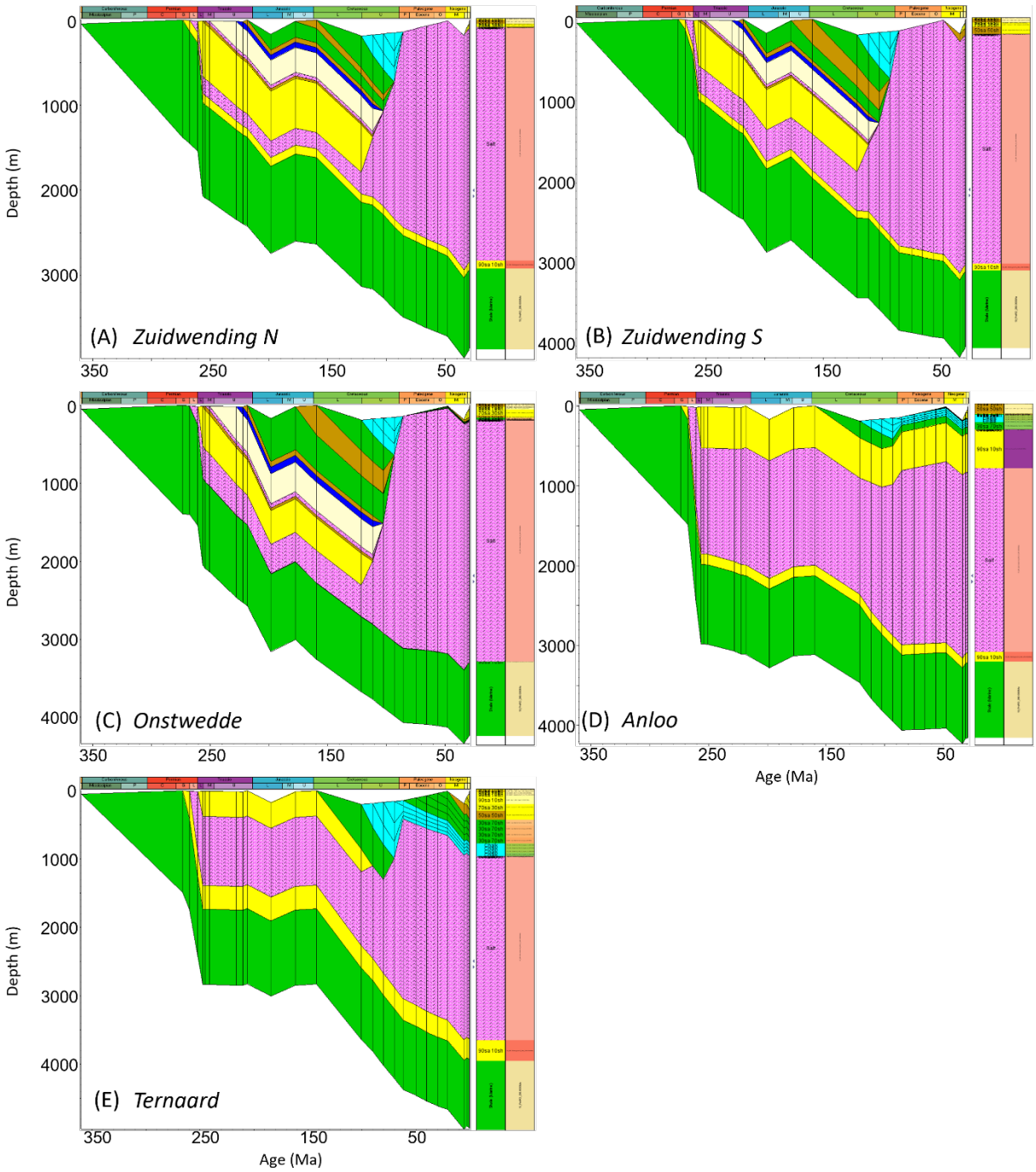

Figure 4-4: Burial history of the four diapirs Zuidwending, Onstwedde, Anloo and Ternaard (locations as rimmed gray circles shown in Fig 2-1).

We first use the thickness growth rate of the salt as an estimate of the diapirism rate (Fig 4-5A-C). The salt thickness is the difference between the depth of the bedded salt and the depth of the selected salt top location. Therefore, it is an estimate of the net diapirism rate, including any thickness loss due to erosion or subrosion. While others are still inactive, diapir Anloo starts its growth in Triassic times with a rate that peaked at 6 m/My in the Late Triassic (Fig 4-5B). The south side of the Zuidwending shows a steady, but slow growth in thickness since its deposition with an average of 1 m/My until the Early Cretaceous. The thickness increments for the other two diapirs Onstwedde, Ternaard, and the north side of Zuidwending are below the resolution of our modelling. All diapirs have an active growth during the deposition of the Late Cretaceous Chalk group. Onstwedde peaks at 70 m/My, Zuidwending follows at 60 m/My, Ternaard 35 m/My and Anloo the slowest at 20 m/My. Continued diapirism in Paleogene

times is also observed for all the four diapirs, while at different rates. Zuidwending north has a diapirism rate of 10 m/My. The diapirism rates of Zuidwending south, Onstwedde and Ternaard are 5 m/My, while Anloo has a diapirism rate of about 1 m/My. Diapirism of Zuidwending north continued in the Neogene, but a lower rates of 6 m/My. The other diapirs stopped growing and start to lose thickness, indicating that erosion and/or subrosion might have been active. Onstwedde and Anloo have a net diapirism rate of over -10 m/My. Calculations for the Quaternary fluctuate, and the accuracy is gradually decreasing due to inherent lower resolution of the seismic interpretation (Table 4-1). Nevertheless, the average diapirism rate in the Quaternary (2.7 Ma to now) is negative and in the order of magnitude of -10 m/My. It is also clear from the trend that the salt removal becomes faster as it approaches the present day (Fig 4-5C). The extreme values of diapirism rate in the order of -400 m/My calculated for Zuidwending north in the Holocene might not be reliable as only less than 10 m thickness variation is simulated in this short period of time (0.02 My), but such values might reflect the accelerated subrosion in the recent thousands of years. Therefore, this negative diapir growth reflecting its burial and/or subrosion is large for the exaggerated diapirs Zuidwending and Onstwedde, but has a lower impact on deeper buried Anloo and Ternaard, which are less influenced by subrosion.

One other way to evaluate the diapirism rate is to calculate the growth of the salt top in respect to the sea floor (bathymetry) (Fig 4-5D-F). This calculation is meaningful in assessing the potential of subrosion. The closer to the sea floor the salt top, the stronger the interaction between salt top and the ground water. Large diapirs such as Zuidwending and Onstwedde have been buried to 1500 to 2500 m depth before Late Cretaceous (Fig 4-5D). Anloo and Ternaard are buried to 500 m depth in Early Triassic, but the following Triassic and Jurassic deposits are missing. All diapirs moved to shallower depths during Late Cretaceous, with Onstwedde at a rate of 60 m/My, Zuidwending 45 m/My, Ternaard 15 m/My and Anloo less than 5 m/My (Fig 4-5E). Consequently, Onstwedde and Zuidwending salt moved closer to the surface, while Anloo and Ternaard remain buried at 700 m depth. This observation explains why the latter two diapirs did not experience strong subrosion at later times. Together with the subrosion, diapirs were further buried in the Pleistocene – Holocene times (Fig 4-5D). These diapirs are now at depths of more than 150 m, likely a result of their coeval zero to negative growth rate, indicating burial and a reduction of subrosion (Fig 4-5F). Similar with the thickness growth rate, the top growth rate also exhibits extreme negative values in the Holocene (0.02 My), showing a continuation of burial.

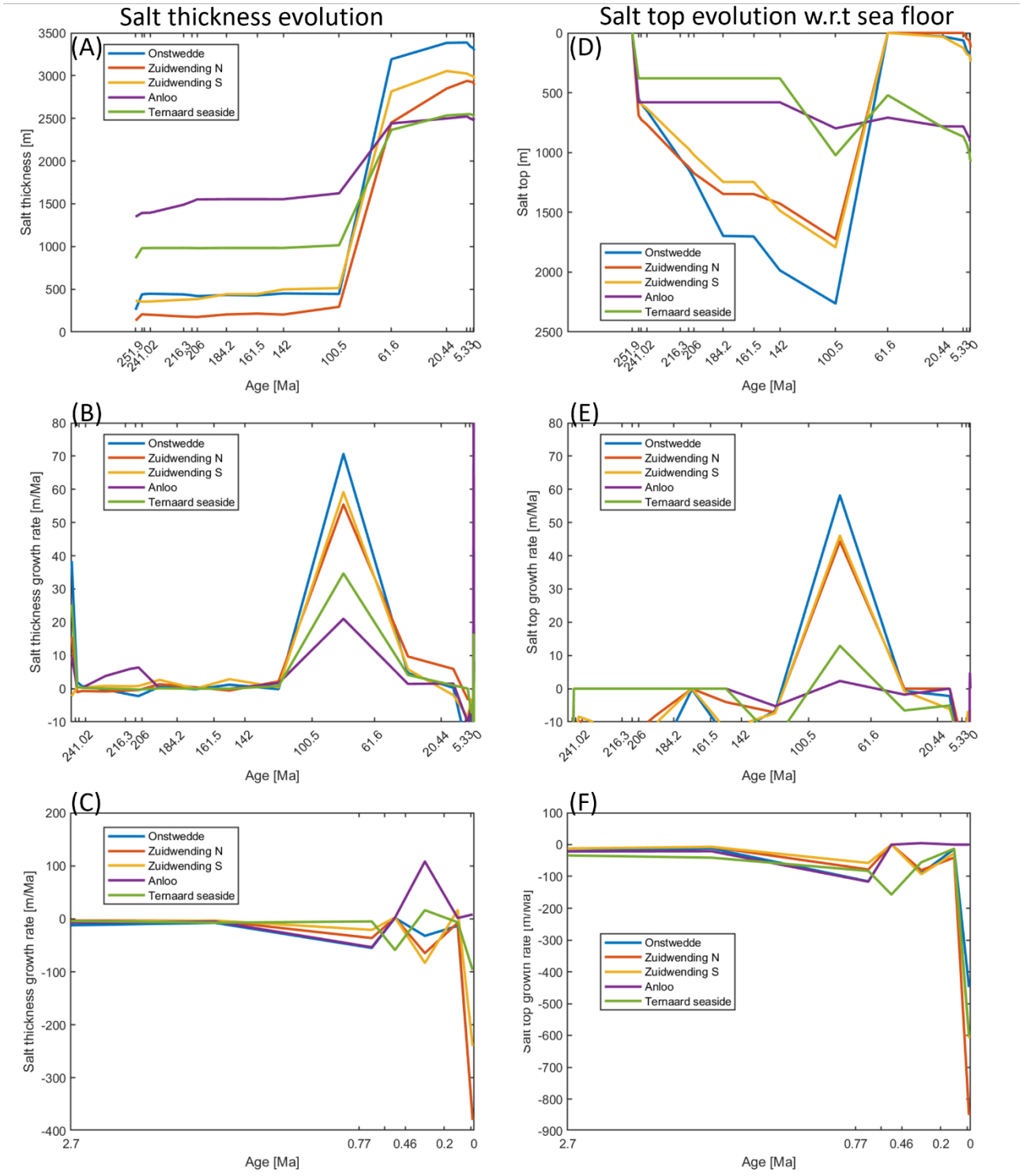

Figure 4-5: Two calculation methods of the diapirism rate for the four diapirs in focus. (A-C) Salt thickness evolution; (D-F) salt top evolution with respect to sea floor. (B,E) diapirism rate with (C,F) a zoom-in in the Quaternary. Note that the calculations in the Quaternary may include numerical artifacts due to the too short intervals.

4.3 Heat transfer and fluid flow simulation results

After calibration, our model was also used to simulate the fluid flow and heat transfer. The simulated temperature and Darcy velocity profiles were used to build the subrosion model presented in Chapter 6. Simulations of heat and fluid flows were conducted using the Visco simulator in TemisFlow™. Fig 4-6 displays the present-day profiles of the physical properties and variables from the simulation with

hydrostatic boundary conditions. Fig 4-7 displays the water overpressure profile and the flow rates. The Zechstein salt has a higher thermal conductivity than other sediments (Fig 4-6B). Therefore, the salt diapirs can reach a higher temperature at shallower depths and at high depths diapirs are colder when compared to the surrounding sediments (Fig 4-6D). However, our model is not able to generate an accurate temperature-depth profile within the salt diapir at its complete lithological composition because the available dataset is not able to separate the salt layer into different lithological distributions across the diapirs. The highest thermal gradient is measured between the top of the diapirs and the surface, where a large temperature contrast is expected (Fig 4-6F). The heat flow follows the thermal gradient, being high above the diapirs, roughly halved inside the diapirs and low elsewhere. The Zechstein salt is impermeable (Fig 4-6CE) and the geometry of diapirs creates a complex water overpressure profile (Fig 4-7A). Over- and under-pressured regions are trapped between the diapirs shown in the cross-section and the fluid flow follows the gradient of the overpressure. The flowing direction is especially complex in shallow sediments that are more porous, while a clear trend of flow is not obvious (Fig 4-7A). The overall overpressure is rather low, below 0.1 MPa everywhere.

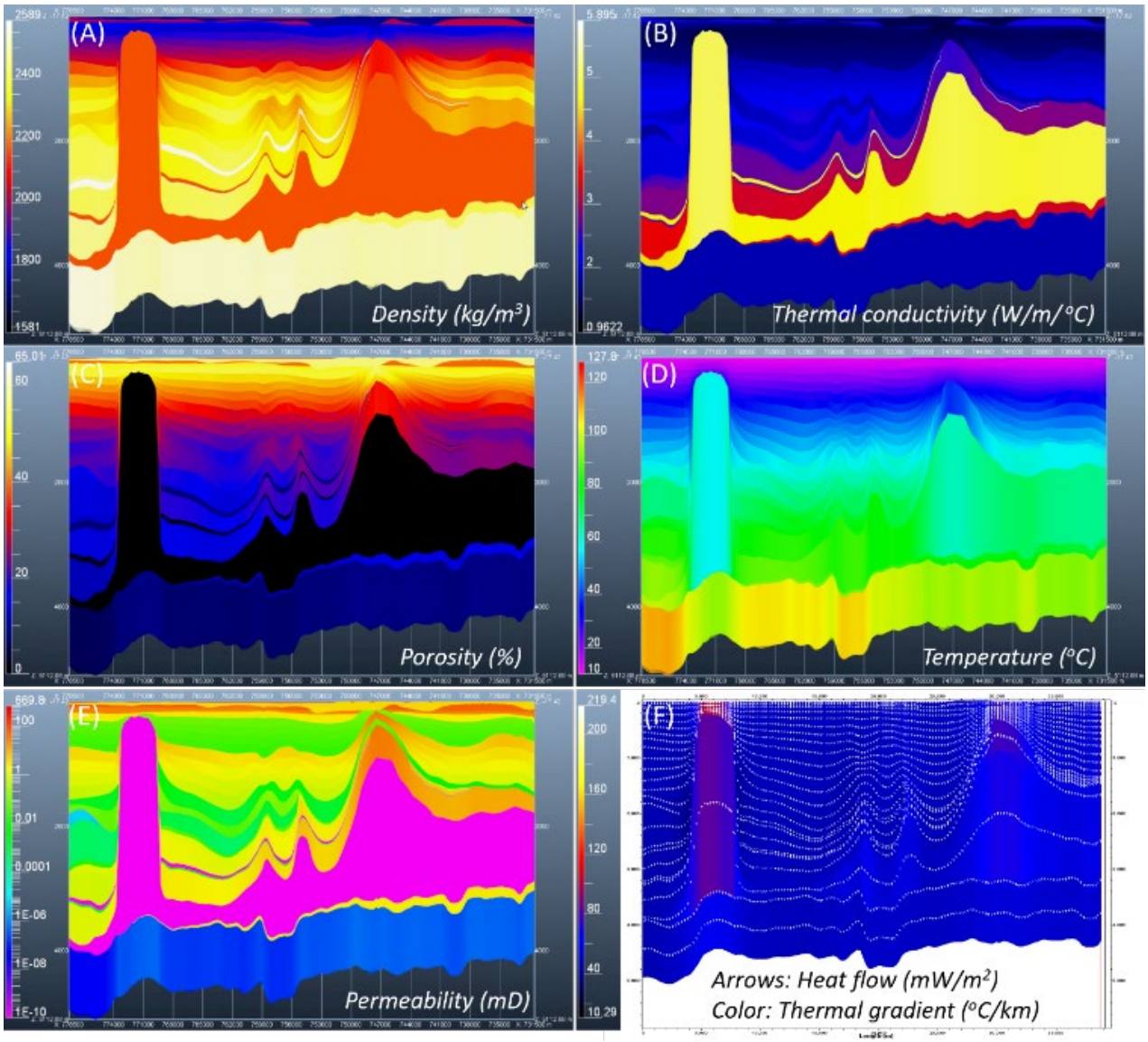

Figure 4-6: Simulated variables along the cross-section Onstwedde-Anloo at present day.

To better quantify the flow pattern and flow rate around the diapirs, we conducted a different simulation with a 1 MPa overpressure from the southern end of the model. We keep the northern end hydrostatic (contact with the North Sea) while the eastern and western boundaries are closed. These boundary conditions generates a general pressure flow gradient that is oriented northwards. The results show a clear trend of fluid flow along the same direction (Fig 4-7B), with a clear trend of flow around the diapirs horizontally or climbing upwards along its flanks (Fig 4-8). The simulated Darcy velocity around the diapir Onstwedde is about 1 mm/yr in the Lower Germanic Triassic reservoir at the bottom of the diapiric flank. In the upper part, this flow is 1-2 orders of magnitude higher in the North Sea Group flanking and overlying the diapirs, at a rate of 2~10 mm/yr. We find the simulated Darcy flow velocity sensitive to the overpressure and the hydraulic gradient. Given that both the hydraulic gradient and the flow rate in the Netherlands are generally poorly constrained at depths higher than 300 m, we infer that our results roughly fit in the broad ranges of Darcy velocity (0.035-3.5 mm/yr in lower regime and 0.35-35 m/yr in upper regime) reported by Geluk et al. (1993). Therefore, the subrosion modelling starts with a 0D parametric study to investigate the influence of and sensitivity on the hydraulic and geochemical properties, while accounting for more complex modelling of geochemically reactive fluid flow based on the temperature and Darcy velocities.

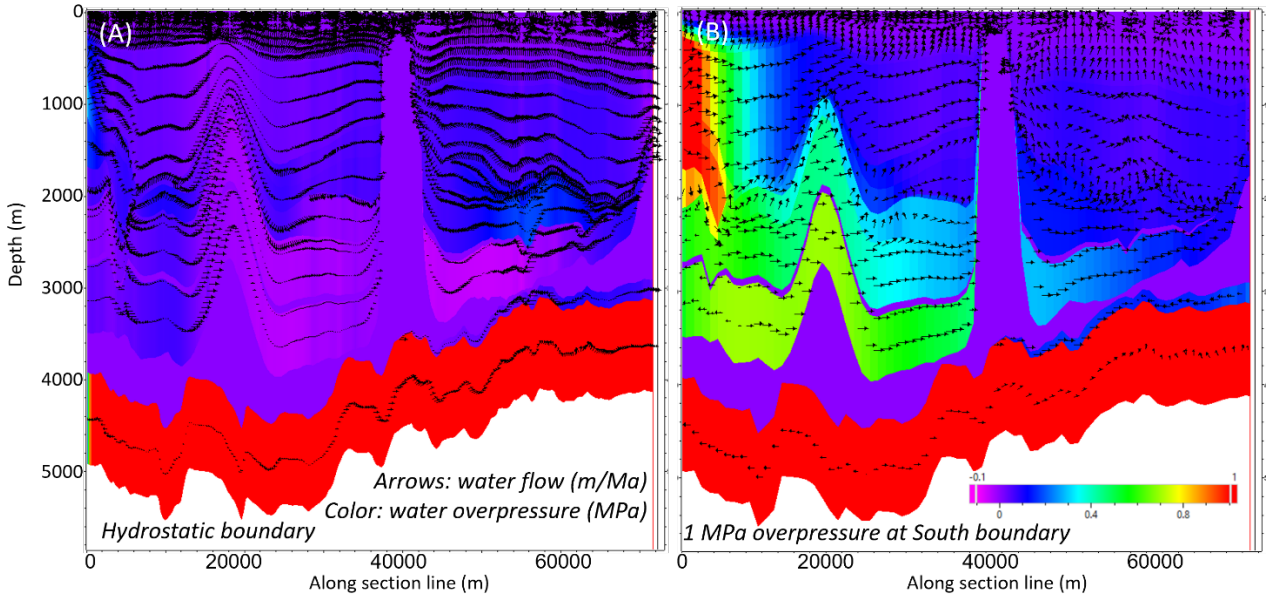

Figure 4-7: Comparison of simulated water flow under (A) hydrostatic condition and (B) with 1 MPa overpressure at the South boundary.

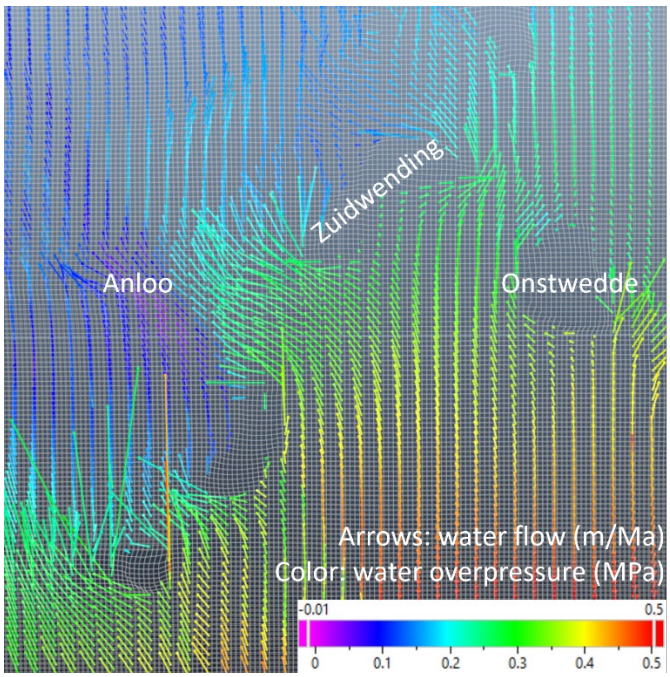

Figure 4-8: Water flow pattern around the two large diapirs. Color of the arrows shows the water overpressure.

5 0D Geochemical modelling: Parametric study

Geochemical modelling is a useful tool for understanding and predicting fluid-rock interaction processes in geological systems (Nader, 2017). One such process is subrosion, the subsurface dissolution of evaporitic rock formations—such as salt diapirs—caused by contact with undersaturated groundwater. This phenomenon can be effectively analyzed using geochemical modelling.

The primary goal of the 0D geochemical modelling in this study is to investigate the impact of the initial mineralogy, the fluid composition at the origin of the subrosion process (called hereafter subroding fluid), the fluid flow rate, and the temperature on the subrosion rate of diapiric salt formations. Specifically, the study focuses on the Permian Zechstein salt in the Netherlands over a period of 1 million years. To achieve this, a series of simulations with varying parameters were performed, modelling the injection of subroding fluids into a 0D grid, that is an opened batch reactor, representing the diapir. The mineral reactions were assessed under kinetic constraints (Fig. 5-1), and subrosion rates were calculated in post-processing, based on the results of the geochemical modelling, following Eq. 1.

The parametric study was conducted using the in-house geochemical calculator "Arxim," which is integrated into the prototype CooresFlow software developed by IFPEN. Arxim's capabilities include aqueous speciation, mineral mass transfer (both at equilibrium and under kinetic constraints), gas equilibria, redox reactions, and microbial processes.

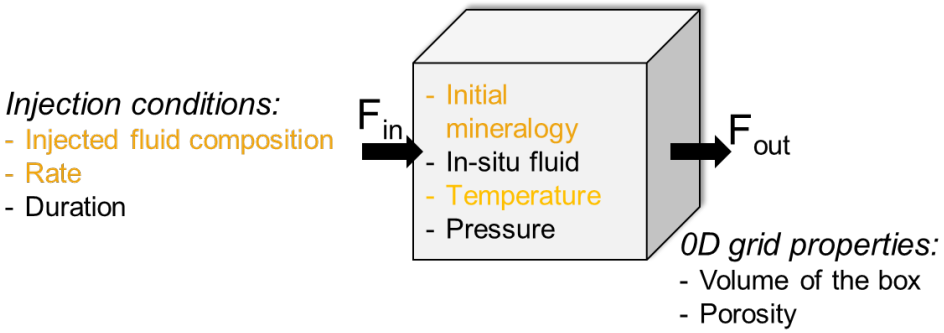

Figure 5-1. Conceptual model representing 0D geochemical simulations performed in the present study to evaluate the effect of key parameters (in orange) on the subrosion rates

The subrosion rates were obtained by dividing the amount of dissolved material by the surface area and the time period:

$$\textbf{subrosion rate}[m.yr^{-1}] = \frac{\Delta V_s}{t_{sim} \times S_{cell}} \quad (Eq.\ 1)$$

Where,

ΔV_s is the volume variation of the solid phase over the simulation period (m^3),

t_{sim} is the total simulation time (yr), and

S_{cell} is the surface area over which the fluid flows (m^2).

5.1 Input data

The dataset for geochemical modelling was defined and compiled in collaboration with Utrecht University. This dataset includes facies characteristics (such as porosity and permeability), the mineralogical

composition of the diapir (both primary and secondary minerals) and the associated kinetic reactions, and the fluid compositions, encompassing both in-situ fluid at equilibrium with the diapir and subroding fluids. Thermodynamic and kinetic data, along with the reactive surface areas of the diapir minerals, were found through a comprehensive literature review. Likewise, typical ranges for flow rate, pressure, and temperature conditions within the diapir were derived from prior studies and Chapter 4 of the present study only for the temperature (references provided below).

Some input data remained fixed throughout the geochemical simulations, while key parameters were varied to evaluate their impact on the subrosion rates. The fixed data is summarized in Table 5-1, and the variable input parameters are discussed in detail below.

Table 5-1. List of the fixed input data for the 0D geochemical modelling.

Data-Type	**Description**
Thermodynamic data base	Thermoddem
Activity model	Pitzer Shemat
System pressure*	1 bar
In-situ fluid composition	Injected fluid composition equilibrated with the initial mineralogy
Simulation period	1 My
Volume of the box	10^3 m^3
Porosity of the box	1 %

* The system is considered monophasic – the range of pressure values in this study has no effects on the investigated mineral stability.

Mineralogical composition

The initial mineralogical compositions were defined based on a TNO report titled *"Database with the Thermal, Hydrological, Mechanical, Chemical Properties of Rock Salt"* (Hunfeld et al., 2023), which includes data from well cores and associated mineralogical analyses. To construct a representative mineralogical dataset, data from three wells located in the northeastern Netherlands, within the region of diapirism, were combined. This dataset comprises a total of 735 mineral samples: BAR-NE-01 with 397 samples, ISH-01 with 38 samples, and VDM-01 with 300 samples. Well locations and initial mineral mass fraction distribution along the wells are shown in Fig. 5-2 and Fig. 5-4, respectively.

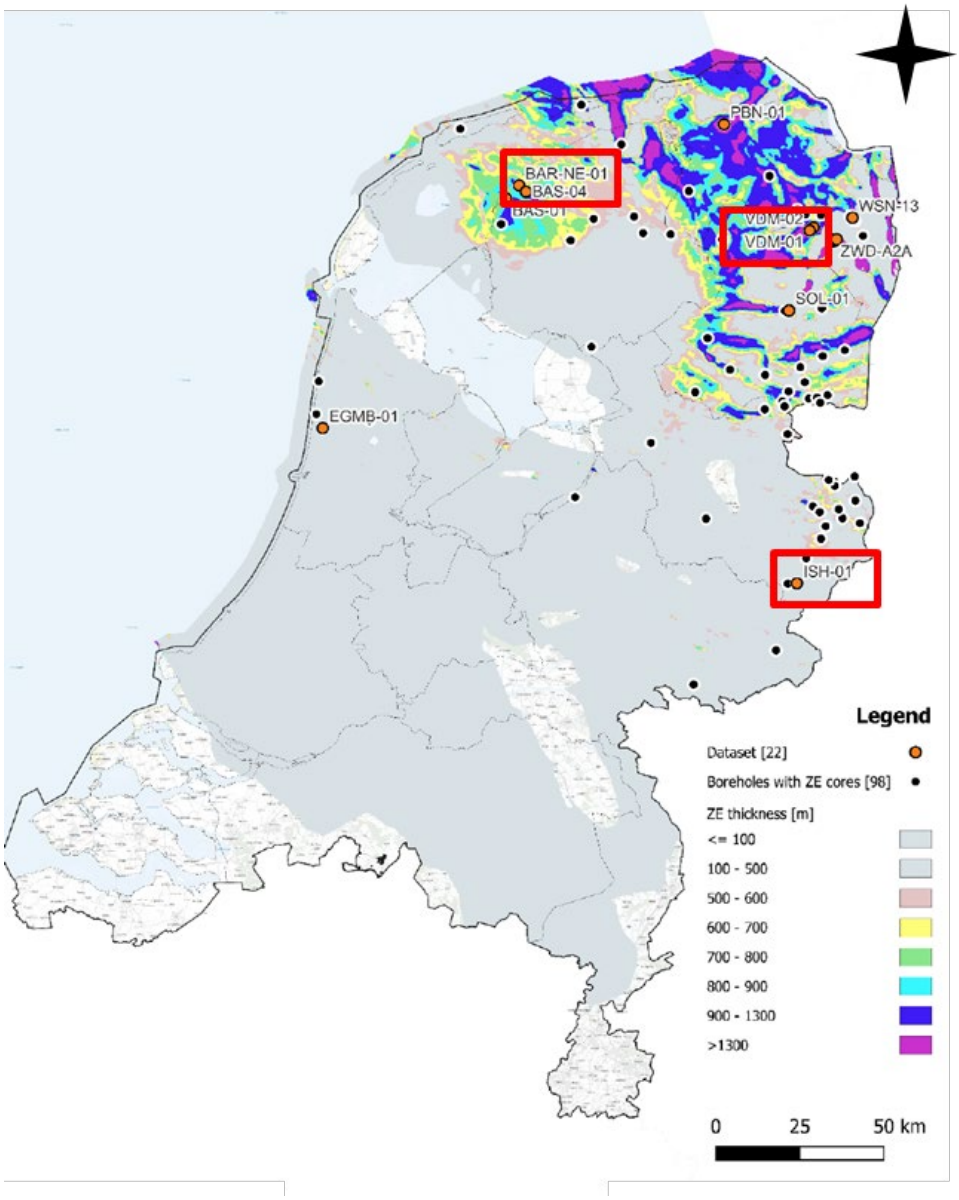

Figure 5-2. Overview of the onshore borehole locations with core retrieved from Permian Zechstein salt (Hunfeld et al., 2023). Locations of the selected wells are indicated with red rectangles.

Table 5-2 presents the median and average compositions of the key salt minerals identified in the studied cores representing the Permian Zechstein salt from the study area. Minerals considered minor in composition (i.e., those with median values below 1 wt.%) have been excluded from the table. The remaining minerals included in this study are: anhydrite, halite, carnallite, and kieserite.

To further analyze the dataset (735 samples), we applied a two-dimensional K-means clustering method, partitioning the samples into four clusters that represent the sequence of crystallization during evaporation up to K-Mg Salt saturation (Table 5-3; Fig. 5-3). Based on these clusters, we identified the corresponding facies, which are as follows: Halite (Cluster 1), Halite with K-Mg Salt (Cluster 2), Sulphate (Cluster 3), and K-Mg Salt (Cluster 0) (Table 5-3).

Table 5-2. Median and average values (in wt.%) of the mineral assemblage composition calculated for the selected dataset from Hunfeld et al. (2023).

[wt.%]	Anhydrite	Halite	Silvite	Carnallite	Bischofite	Kieserite
Median	1.1	60.8	0.	19.5	0.	2.7
Average	3.5	62.2	1.2	25.6	0.6	6.8

Table 5-3. Median values of the mineral composition in wt. % calculated for each cluster (based on K-means clustering method) and the corresponding facies.

Cluster	Anhydrite	Halite	Carnallite	Kieserite	K-Mg Salt	Facies
1	1	99	0	0	0	Halite
2	1	61	24	8	37	Halite + K-Mg Salt
3	90	10	0	0	0	Sulphate
0	1	31	55	5	68	K-Mg Salt dominant

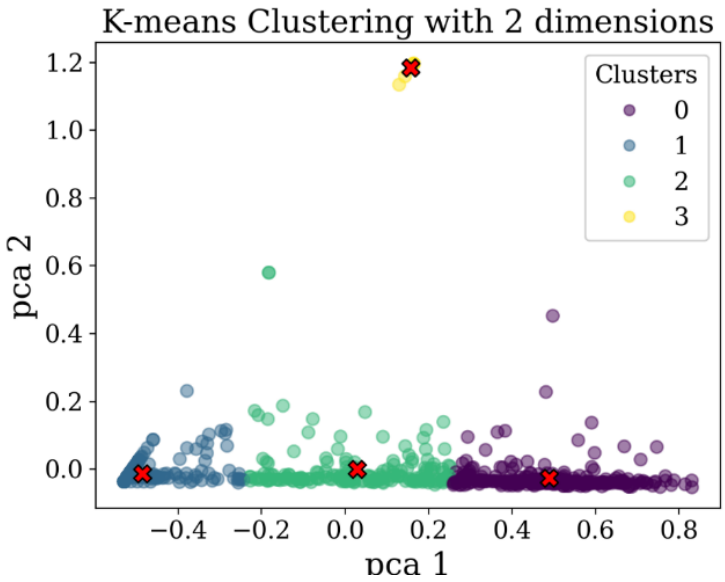

Figure 5-3. Partition of the 735 samples contained in the dataset into four clusters as a result of two-dimensional K-means clustering. The red crosses represent the centroids.

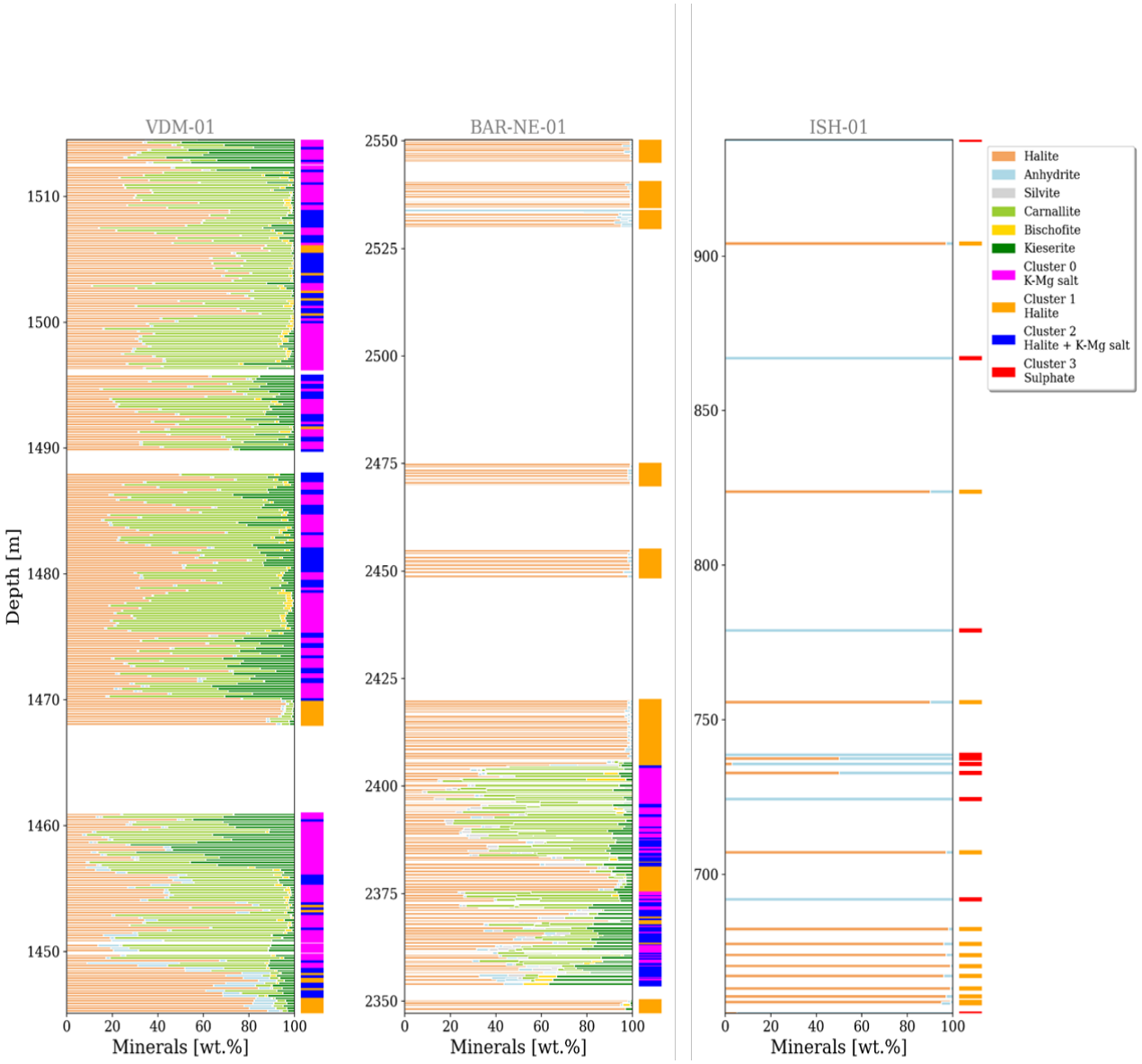

Figure 5-4. Initial mineral mass fractions (in wt.%) from core analysis of wells VDM-01, BAR-NE-01, and ISH-01 (Hunfeld et al., 2023; Nlog.nl), and the corresponding clusters. Empty white corresponds to depths without data.

Based on the K-means clustering results and the identified facies, three distinct mineralogical compositions were selected as initial salt constituents for the parametric study: Halite (M1), Sulphate (M2), and K-Mg Salt (M3). These compositions encompass varying mol% proportions of halite, carnallite, kieserite, and anhydrite (Table 5-4). The mineral dissolution reactions, kinetic parameters, log-rate constants (at 25°C), reactive surface areas, and activation energies of these facies-related minerals are shown in Table 5-5.

Table 5-4. Initial mineralogical constituents selected for the parametric study.

[mol %]	Halite – M1	Sulphate – M2	K-Mg Salt – M3
Halite	100	30	34
Carnallite	0	0	60
Kieserite	0	0	5
Anhydrite	0	70	0

Table 5-5. Mineral dissolution reactions and kinetic parameters used in the parametric study.

	Log-rate constant at 25°C	Reactive surface area [$m^2\ kg^{-1}$]	Activation energy [$kJ\ mol^{-1}$]
Halite $NaCl = Na^+ + Cl^-$	- 0.21	1×10^{-4}	7.4
Carnallite $KMgCl_3{:}6H_2O = K^+ + Mg^{2+} + 3Cl^- + 6H_2O$	- 0.21	1×10^{-4}	7.4
Kieserite $MgSO_4{:}H_2O = Mg^{2+} + SO_4^{2-} + H_2O$	- 3.19	1×10^{-4}	14.3
Anhydrite $CaSO_4 = Ca^{2+} + SO_4^{2-}$	- 3.19	1×10^{-4}	14.3

Subroding fluid composition, flow and thermal conditions

The conceptual model initially incorporates the mineralogical composition (salt) and the in-situ fluid, which is in equilibrium with the mineral phases under the suggested subsurface conditions. In the second phase, this system will be perturbed by the injection of a subroding fluid that is not in equilibrium with the existing minerals, leading to mineral dissolution and the onset of the subrosion process. Consequently, the subroding fluid must be defined and chemically characterized prior to its integration into the geochemical model.

Following a literature review and consultations with experts from Utrecht University and COVRA, we proposed three different types of fluid compositions for the subroding fluid to be used in the simulations (Table 5-6). These compositions correspond to waters typically found in shallow aquifers, deeply buried aquifers, and deep oil/gas reservoirs in the Netherlands. Table 5-6 presents the specific chemical compositions (pH, and concentrations of aqueous species in mg L^{-1}) of the proposed fluid compositions, which are primarily based on the works of Griffioen et al. (2016). The salinity of these fluids ranges from 1 g L^{-1} to 90 g L^{-1}. The degree to which the subroding fluids deviate from equilibrium with respect to the mineral phases can be quantified using the saturation index (SI = log Q/K): The more negative the mineral's saturation index, the further the fluid is from equilibrium with respect to that mineral. Table 5-7 shows the

calculated saturation index values for the four key salt-forming minerals—halite, anhydrite, carnallite, and kieserite—at 25°C and 1 bar for the three proposed subroding fluids.

Table 5-6. Selected subroding fluid median compositions for the parametric study (from Griffioen et al., 2016).

[mg L^{-1}]	**Shallow aquifers – S1**	**Deep, buried aquifers – S2**	**Deep O&G aquifers – S3**
pH	7.7	7.5	6.4
Na^+	582	3480	30400
K^+	25	67.2	310
Ca^{2+}	46.5	106	3958
Mg^2	19.8	85.1	920
Cl^-	460	5200	59130
SO_4^{2-}	43.2	93.7	78.8
HCO_3^-	458	595	231
H_4SiO_4	15.35	18.5	102

Table 5-7. Distance of the subroding fluids from the equilibrium with respect to the selected salt-forming minerals.

SI = log (Q/K) [25°C/1bar]	**Shallow aquifers – S1**	**Deep, buried aquifers – S2**	**Deep O&G aquifers – S3**
Halite	-5	-3.5	-1.7
Anhydrite	-2.3	-2.2	-1.3
Carnallite	-16.4	-13.3	-8.9
Kieserite	-6.3	-6	-5.6

In addition to the initial mineralogy of the diapir and the chemical composition of the subroding fluid, the estimated flow rates and temperature conditions may significantly influence the resulting subrosion rates. Consequently, these factors were also considered in the parametric study. Simulations were conducted using four different estimated Darcy velocity values: approximately (Q1) 1×10^{-6} m yr^{-1}, (Q2) 5×10^{-5} m yr^{-1}, (Q3) 5×10^{-4} m yr^{-1}, and (Q4) 5×10^{-3} m yr^{-1}. Additionally, three temperature values were selected—approximately (T1) 20°C, (T2) 50°C, and (T3) 80°C—based on the known depth positions and geothermal gradients of the investigated diapirs.

5.2 Results

In total, 30 geochemical calculations were conducted using Arxim to investigate the subrosion (dissolution) rates of three distinct facies of salt rocks (M1, M2, M3) under various conditions of water salinity, temperature, and flow velocities (Table 5-8). These calculations were organised into 10 simulation sets, each comprising different combinations of salinity values (S), temperature (T), and flow velocities (Q) for the three facies. The tested salinity levels included 1 g L^{-1} (S1), 9 g L^{-1} (S2), and 90 g L^{-1} (S3). Three temperature values were used: approximately 20°C yr^{-1}, Q2 = 5×10^{-5} m yr^{-1}, Q3 = 5×10^{-4} m yr^{-1}, and Q4 = 5×10^{-3} m yr^{-1}. Calculations with varying salinities and flow velocities were performed at the median temperature of 50°C. All simulations were conducted over a total duration of 1 million years (Table 5-8).

Table 5-8. Physico-chemical conditions (salinity, temperature, flow velocity and duration) for the simulation sets, performed on the three selected rocks salt facies (M1: halite; M2: Sulphate; M3: K-Mg salt).

	Simulation Set (N= 30 simulations)																								
	S1			S2			S3			T1			T2			T3			Q1			Q2			Q3			Q4		
	M1	M2	M3	M1	M2	M3	M1	M2	M3	M1	M2	M3	M1	M2	M3	M1	M2	M3	M1	M2	M3	M1	M2	M3	M1	M2	M3	M1	M2	M3
Salinity [gr L^{-1}]	1			9			90												9											
Temperature [°C]				50						20			50			80									50					
Velocity [m yr^{-1}]										1×10^{-6}									1×10^{-6}			5×10^{-5}			5×10^{-4}			5×10^{-3}		
Time [Myr]																1														

Figure 5-5 shows the evolution of the mineral volume fractions over the simulation time for each facies under varying physicochemical conditions (S1 to S3 for salinity, T1 to T3 for temperature, and Q1 to Q4 for flow velocity). Significant differences in the dissolution behavior can be seen among the facies.

For the Halite facies, only minor changes were observed in the mineral volume fractions across different salinity values (S1, S2, and S3), with dissolution occurring at a slow and steady pace over time. Similarly, the Sulphate facies, dominated by anhydrite, exhibited very limited dissolution, with the volume fraction of anhydrite remaining largely constant regardless of salinity variations, emphasizing that anhydrite dissolution is negligible in this context.

In contrast, the K-Mg Salt facies, particularly carnallite and kieserite, showed a pronounced response to salinity variations. Dissolution increased significantly when salinity decreased, especially under conditions S2 and S3, as demonstrated by the sharp drop in mineral fractions for carnallite. The effect of salinity is most evident under lower salinity conditions (S1), where the mineral fraction of carnallite decreased quickly compared to the higher salinity scenarios.

Temperature variations (T1 to T3, ranging from 20 to 80°C) did not produce distinct dissolution patterns across the three facies. The evolution of mineral volume fractions of Halite, Sulphate, and K-Mg Salt over time remained similar under different temperatures, suggesting that within the tested range, temperature had a minimal impact on the dissolution rates for all facies.

Flow velocity (Q1 to Q4) had a significant influence on dissolution for all three facies. As flow velocity increased, there was a rapid reduction in the initial mineral volume fractions. For halite, carnallite, and

kieserite, the dissolution process accelerated noticeably with velocities greater than Q1. Similarly, anhydrite dissolution was affected with velocities above Q2, although the overall change was still less significant compared to the K halite, carnallite, and kieserite. The results show that flow velocity is a critical factor driving the dissolution of these minerals, particularly for the K-Mg Salt facies, where dissolution occurs rapidly under higher velocity conditions (Q3 and Q4).

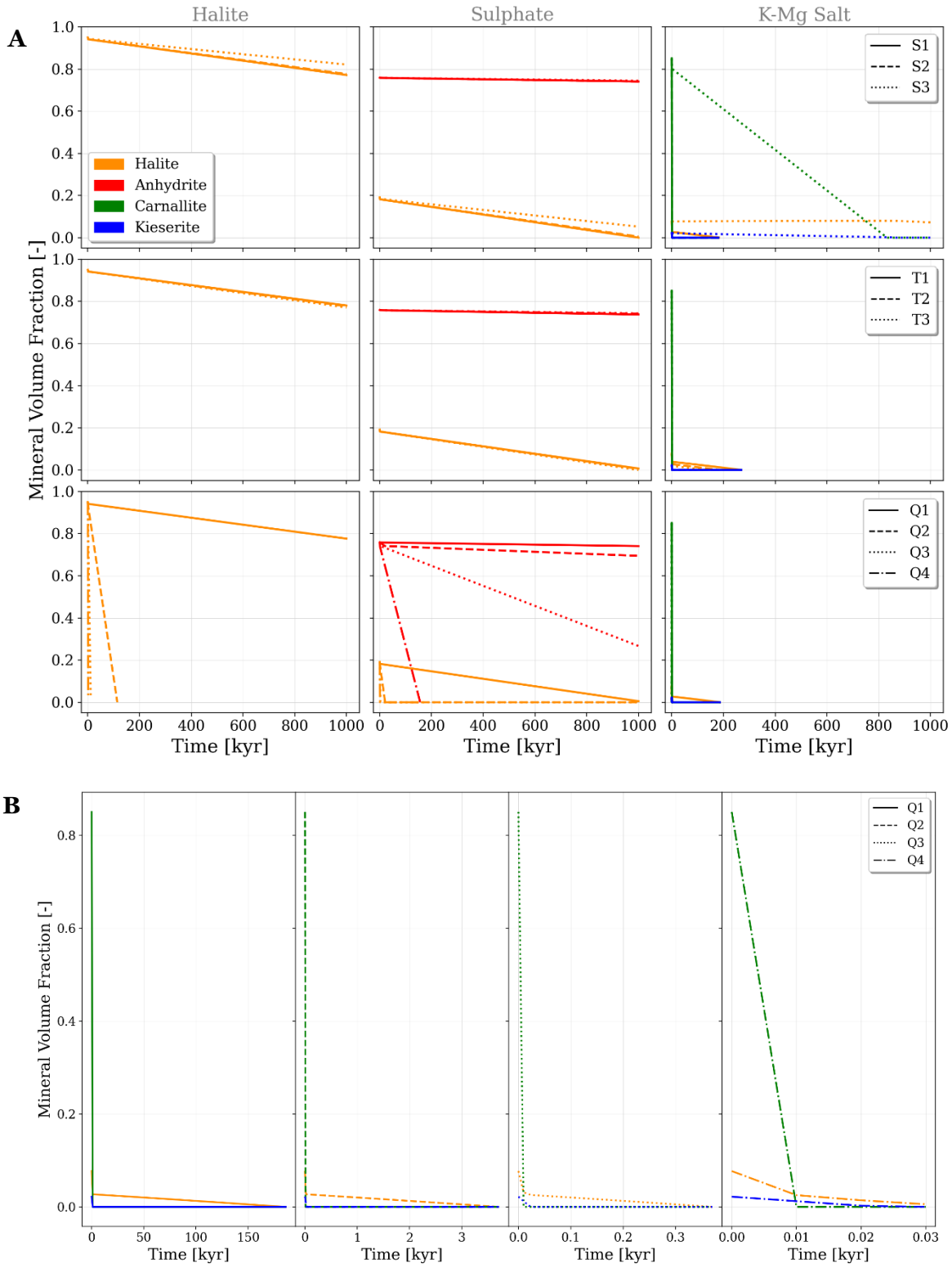

Figure 5-5. A) Cross-plots showing the evolution of the mineral volume fraction over time (up to 1Myr) for the mineral phases of the Halite, Sulphate, and Kg-Mg Salt facies under varying conditions (S1= 1 gr L^{-1}, S2= 9 gr L^{-1}; S3= 90 grL^{-1}; T1=

20°C, T2= 50°C, T3= 80°C; Q1= 1 × 10^{-6} m yr^{-1}, Q2= 5 × 10^{-5} m yr^{-1}, Q3= 5 × 10^{-4} m yr^{-1}, Q4=5 × 10^{-3} m yr^{-1}); B) Zoom in on the results of the flow velocity conditions for the K-Mg Salt facies.

In summary, our simulation results indicate that flow velocity plays a dominant role in the dissolution process for all three facies considered in this study. In contrast, variations in salinity and temperature had minimal impact on the dissolution of halite and anhydrite, with the latter remaining largely inert. However, for the K-Mg Salt facies, including carnallite and kieserite, dissolution was notably sensitive to changes in salinity, particularly at low salinity levels. Across most conditions, initial mineral volumes for the K-Mg Salt facies decreased rapidly at the onset of reactions, except under the high-salinity condition S3 (90 g L^{-1}), where dissolution was slower and limited (Fig. 5-5).

Figure 5-6 shows the quantified effect of different environmental conditions on the subrosion rates of K-Mg Salt, Sulphate, and Halite facies. Subrosion is analysed in relation to maximum and minimum values of temperature, salinity, and fluid velocity. The related subrosion rates are also reported in Table 5-9.

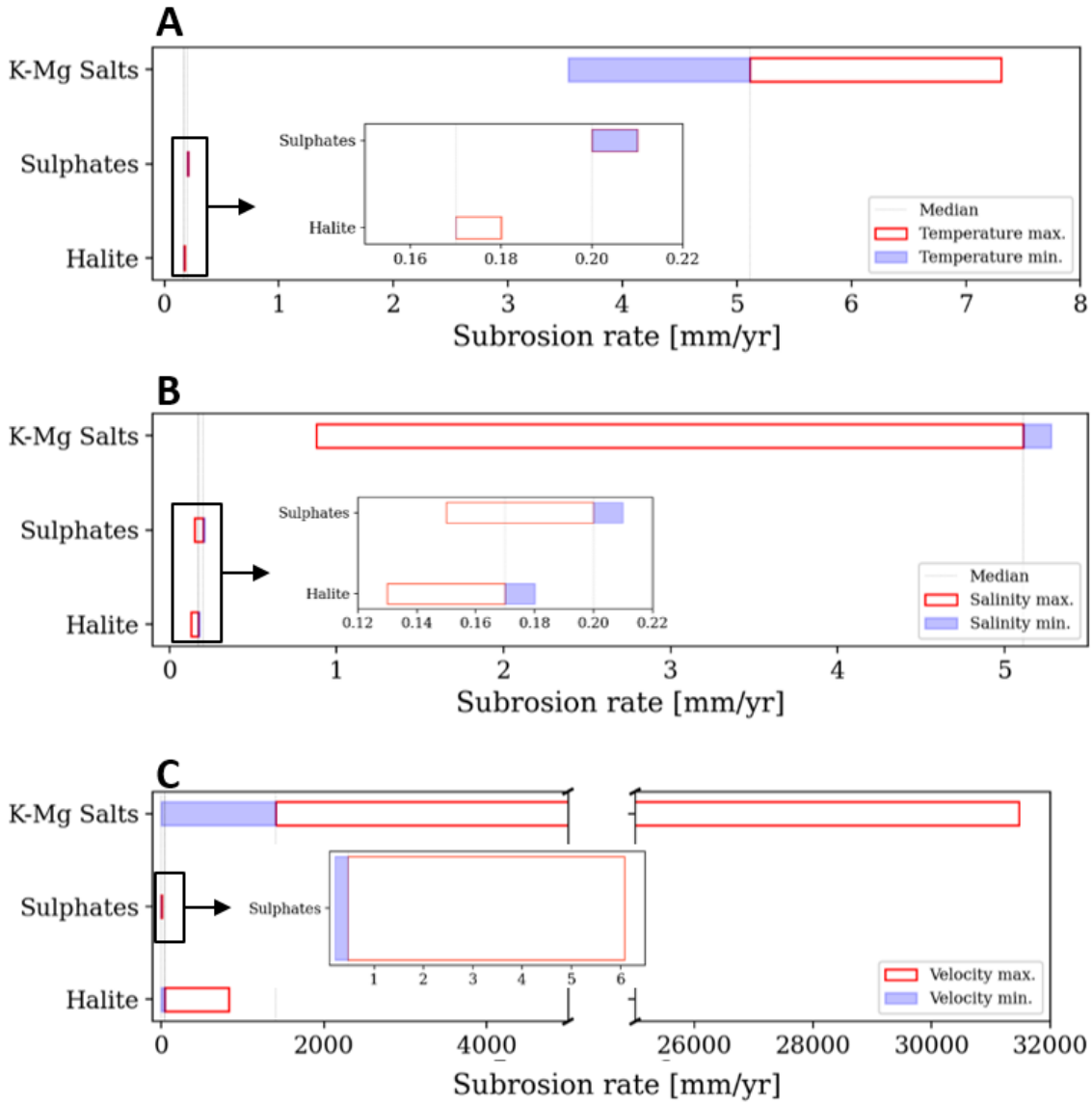

Figure 5-6. Diagrams showing the effects of (A) temperature, (B) salinity, and (C) velocity on the subrosion rate for K-Mg Salt, Sulphate, and Halite.

In Fig. 5-6A, subrosion rates are shown as a function of temperature, with maximum (red lines) and minimum (blue areas) values. The dissolution rate for Halite and Sulphates remains low, whereas K-Mg Salt exhibit significantly higher rates, reaching up to ~7 mm yr^{-1}. For all facies, the effect of temperature appears minor, with Sulphate and Halite subrosion rates only slightly influenced. However, the K-Mg Salt facies shows a noticeable sensitivity to temperature, where the subrosion rate increases from 3.53 to 7.31 mm yr^{-1} as temperature rises from 20°C to 80°C.

In Fig. 5-6B, the subrosion rates are plotted as a function of salinity, again showing maximum (red lines) and minimum (blue areas) values. The data highlights that the subrosion rate generally decreases with increasing salinity for all facies. K-Mg Salt display the highest dissolution rates, exceeding 5 mm yr^{-1}, for the subroding fluid furthest from equilibrium, and their subrosion rate is particularly sensitive to changes in salinity. In contrast, Sulphate and Halite facies show more stable subrosion rates, varying only between 0.13 and 0.18 mm yr^{-1} and 0.15 and 0.21 mm yr^{-1} respectively, when salinity decreases from 90 to 1 g L^{-1}.

Figure 5-6C highlights the strong influence of fluid flow velocity on subrosion rates. The K-Mg Salt facies, in particular, is highly sensitive to variations in flow velocity, with rates increasing dramatically up to 30 m yr^{-1} for the highest flow velocities considered in this study (Q4, 5×10^{-3} m yr^{-1}). Sulphate and Halite are less affected by these variations in flow velocity but still show notable changes, with subrosion rates increasing from 0.17 mm yr^{-1} to 0.82 m yr^{-1} for the Halite facies when the fluid velocity is multiplied by a factor 4.

Overall, Figure 5-6 underscores the complex interplay between temperature, salinity, and fluid flow velocity in controlling the subrosion rates of geological salts, with K-Mg salts being the most sensitive to variations in these factors, particularly flow velocity.

Table 5-9. Resulting subrosion rates (mm yr^{-1}) for the investigated salt facies (Halite, Sulphate and K-Mg Salt), under the varying salinity (S), temperature (T), and flow velocity (Q) values (in Table 5-8).

Subrosion Rate [mm yr^{-1}]	**Halite**	**Sulphate**	**K-Mg Salt**
S1 (1 g L^{-1})	0.18	0.21	5.28
S2 (9 g L^{-1})	0.17	0.20	5.11
S3 (90 g L^{-1})	0.13	0.15	0.88
T1 (20°C)	0.17	0.21	3.53
T2 (50°C)	0.17	0.20	5.11
T3 (80°C)	0.18	0.21	7.31
Q1 (1×10^{-6} m yr^{-1})	0.17	0.20	5.11
Q2 (5×10^{-5} m yr^{-1})	8.33	0.26	2.6×10^{2}
Q3 (5×10^{-4} m yr^{-1})	8.3×10^{1}	0.68	2.6×10^{3}
Q4 (5×10^{-3} m yr^{-1})	8.3×10^{2}	6.08	3.1×10^{4}

5.3 Synopsis of the 0D geochemical modelling

The main concluding statements based on the results of the undertaken (0D) geochemical modelling parametric study, including 30 simulations on three principal salt facies, representing the Permian Zechstein salt diapirs in the Netherlands with fixed and varying input parameters are:

- Subrosion rates were calculated through geochemical modelling for Halite, Sulphate (halite + anhydrite), and K-Mg Salt facies, considering varying salinities (1 to 90 g L^{-1}), temperatures (20 to 80°C), and Darcy flow velocities (1×10^{-6} m yr^{-1} to 5×10^{-3} m yr^{-1}), over 1 million years (Myr).
- Darcy flow velocity has the most significant impact on subrosion rates, which increase linearly with rising velocity for Halite and K-Mg Salt facies.
- The distance of the subroding fluid from equilibrium—represented here by salinity—also affects the subrosion rate, though its influence is less pronounced than that of Darcy velocity. The greater the deviation from equilibrium, the higher the subrosion rate. Recharge fluids that are further from equilibrium with carnallite and kieserite lead to these minerals dissolving more quickly than halite and anhydrite.
- Initial mineralogy is crucial, as highly reactive K-Mg Salt exhibit complete dissolution within 1 Myr under all conditions explored in this study. In contrast, anhydrite shows very low solubility. Consequently, the subrosion rate increases with a higher proportion of K-Mg Salt and decreases with an increase in the amount of anhydrite.
- The temperature range considered in this study has a negligible effect on the subrosion rate compared to Darcy velocity, salinity, or initial mineralogy.

6 3D Reactive transport modelling

3D reactive transport models were developed to simulate the subrosion process at the top and flanks of the Permian Zechstein salt diapirs in the Netherlands, under two scenarios: with and without the presence of a caprock. The input data for these models were sourced from published articles, reports, results from Task 1 (Phase 1 – basin modelling) and geochemical modelling, as well as consultations with Utrecht University experts. The model incorporated monophasic fluid flow, described by Darcy's law, and accounted for advective and dispersive solute transport under isothermal conditions**.** Chemical reactions under kinetic constraints were considered within the diapir, while the surrounding rock was treated as inert. The variation in fluid properties (density and viscosity) was calculated throughout the simulation, with density changes based on pressure, temperature, and salinity, and viscosity changes based on temperature and salinity, over time. The simulations were run for a period of 10 kyr due to the high computational cost of solving the chemical subsystem. The resulting trends can be proposed as starting point for deducing subrosion evolution over longer periods. The model's conceptual framework was based on the schematic representation of the diapir as outlined by Geluk et al. (1993).

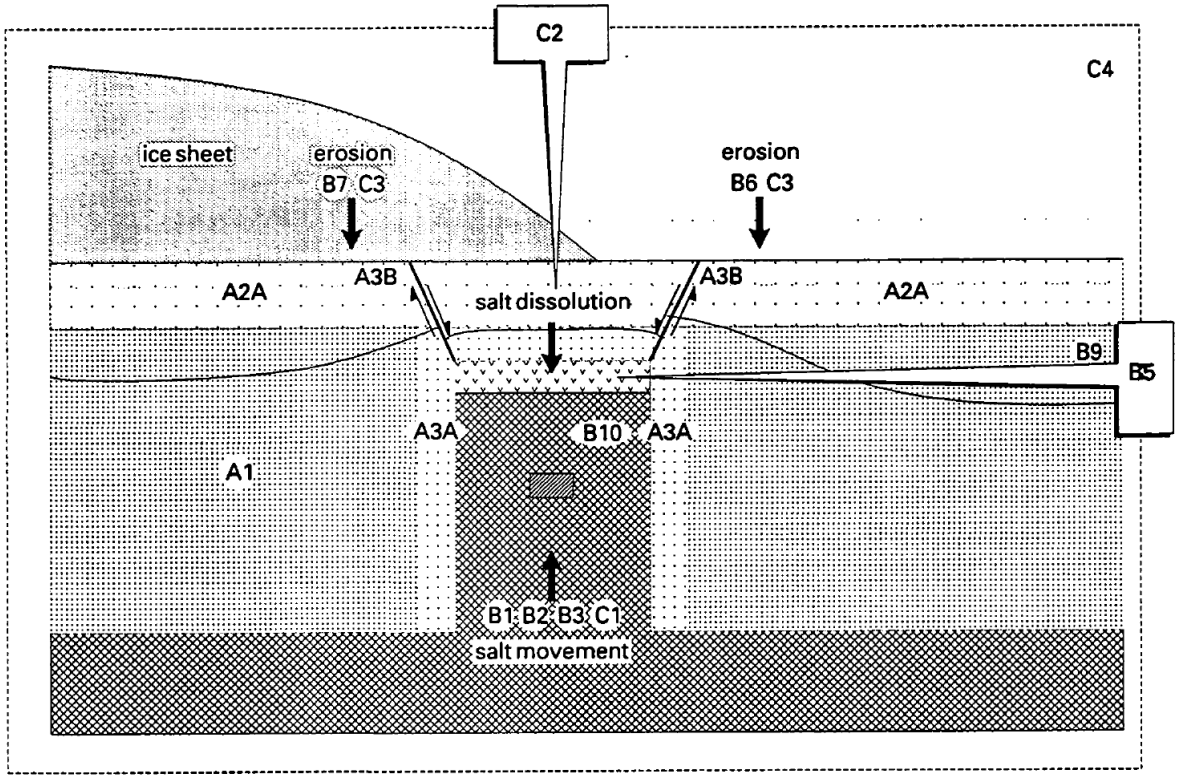

Figure 6-1. Conceptual diapir model from Geluk et al. (1993), showing the salt diapir, the host rock and the overburden. The salt diapir caprock formation and subrosion are also indicated.

6.1 3D model construction

Model geometry

The geometry was simplified to a 3D heterogeneous model with a limited extent in the y-direction, comprising four layers, due to computing time constraints and in line with the set objective of building on the Geluk et al. (1993) conceptual model. The structured mesh dimensions are 23 km in the x-direction, 0.2 km in the y-direction, and 2.5 km in the z-direction. The diapir measures 3 km × 0.1 km × 2.35 km and occupies only two layers in the y-direction to facilitate water flow in the third dimension. The top of the diapir is located about 150 m below the upper boundary of the grid in the no-caprock scenario and about

250 m below the upper boundary in the caprock scenario. The spatial resolution is set at 0.2 km × 0.05 km × 0.05 km (Fig. 6-2).

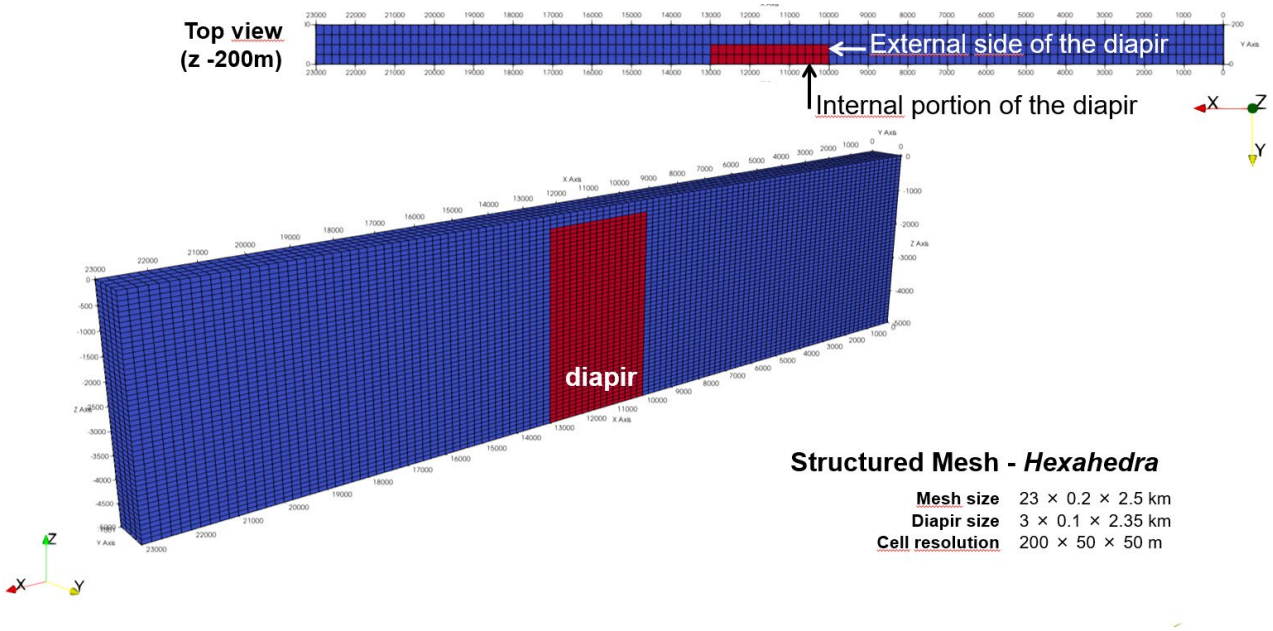

Figure 6-2. Configuration of the 3D grid model of the salt diapir (red cells) in host rock (blue cells): (above) a top view (at -200m from the upper limit of the grid showing topmost part of diapir surrounded by the host rock; (below) a side view of the model (along x-axis) showing the diapir position in the host rock. This configuration is based on the conceptual model provided by Geluk et al. (1993) and presented in Figure 6-1. A scale factor of 2 was applied on the z-axis to ease the readability.

Rock and fluid properties

Most of the rock and fluid properties come from the literature review, the results of Task 1 of the project (Basin modelling), and the parametric study (this report, above).

The geological formations represented in the model, from top to bottom, include Cenozoic clastics (0 to 750 m in depth), Upper Cretaceous carbonates (750 to 1450 m), Jurassic carbonates and sand (1450 to 1750 m), Upper and Middle Triassic carbonates and sandstones (1750 to 2200 m and 2200 to 2500 m, respectively), and the Permian Zechstein diapir salt, which extends from 150 m to 2500 m in depth (Table 10).

Two caprock lithologies were also included: gypsum and anhydrite. Gypsum is assumed to be located at the top of the salt diapir, at depths ranging from 150 to 200 m, while anhydrite is situated just below, between depths of 200 and 250 m (Table 6-1).

Table 6-1. Rock and fluid properties of the 3D transport reactive model. The lithological units are listed from top (younger) to bottom (older), with the exceptions made for the caprock. The related references are indicated.

Lithology name	Facies	Fluid	Porosity	Permeability [m²]	Density [kg m⁻³]	Reference
Cenozoic (0, -750m)	1	1	0.23	1×10^{-12}	2600	Magri et al. (2005)
Upper Cretaceous (-750, -1450m)	1	1	0.20	2×10^{-14}	2600	Reservoir property maps NLOG
Jurassic (-1450, -1750m)	1	1	0.13	1×10^{-13}	2600	Magri et al. (2005)
Upper Triassic (-1750, -2200m)	1	1	0.11	2×10^{-14}	2600	Reservoir property maps NLOG
Middle Triassic (-2200, -2500m)	1	1	0.06	1×10^{-14}	2600	Magri et al. (2005)
Diapir (-150, -2500m)	2	2	0.01	1×10^{-18} -10^{-22}	2100	Reservoir property maps NLOG
Caprock gypsum (-150, -200)	3	3	0.01	1×10^{-20}	2100	Geluk et al. (1993)
Caprock anhydrite (-200, -250)	4	2	0.01	1×10^{-15}	2100	Geluk et al. (1993)

These geological formations correspond to four facies: (1) host rock (clastics and carbonates), (2) salt, (3) gypsum caprock, and (4) anhydrite caprock (Table 11). Three in-situ fluids were considered: Fluid 1 present in the host rock, Fluid 2 at equilibrium with the salt diapir and the anhydrite caprock, and Fluid 3 at equilibrium with the gypsum caprock. The chemical compositions of these fluids are presented in Table 6-2. The thermodynamic database Thermoddem along with the Pitzer-Shemat activity model were used in this study, while the kinetic database was derived from Palandri and Kharaka (2004).

Table 6-2. Mineralogical composition of the host-rock (facies 1), salt diapir (facies 2), gypsum caprock (facies 3), and anhydrite caprock (facies 4).

Minerals	Facies 1 [mol %]	Facies 2 [mol %]	Facies 3 [mol %]	Facies 4 [mol %]
Inert Halite	100	0	0	0
Halite	0	80	0	0
Gypsum	0	0	100	0
Anhydrite	0	20	0	100

Table 6-3. In-situ fluid compositions for the host-rock (1), salt diapir (2), and caprock (3).

Elements	Fluid 1 [mol kg^{-1}]	Fluid 2 [mol kg^{-1}]	Fluid 3 [mol kg^{-1}]
C	0.0098	0.0098	0.0095
Ca	0.0026	0.37	0.61
Cl	0.15	6.83	7.12
K	0.0017	0.0017	0.0011
Mg	0.0035	0.0035	0.0035
Na	0.15	6.83	7.12
S	0.00098	0.36	0.61
Si	0.00019	0.00019	0.00019

Initial and boundary conditions

The initial and boundary conditions used in this study are presented in Tables 6-4 and 6-5, respectively. The temperature in the diapir domain was set at 58°C corresponding to the modelled temperature in Basin Modelling, while the temperature within the host rock followed a linear gradient of 35°C km^{-1} (Geluk et al., 1993), with the surface temperature established at 10°C. Pressure was assumed to be hydrostatic throughout the entire domain. Water saturation was set at 100 mol% for both domains, with a NaCl molar fraction of 0.27 mol% in the surrounding rock and 7.5 mol% in the diapir (Table 6-3).

A fixed pressure gradient of 0.002% was set between the lateral boundaries to simulate natural groundwater flow similar to those observed in the North East German Basin where salt structures are also observed (Magri et al., 2005). Data from Germany were used since no information was found for the northern part of the Netherlands. The top boundary is open to meteoric recharge at a rate of 2.9×10^{-4} m^3 s^{-1}, while the bottom and side (parallel to the flow direction) boundaries are closed (Table 6-4). The fluid that is allowed to flow into the model at the top and lateral sides corresponds in terms of composition to that of Fluid 1 (Table 6-2).

Table 6-4. Initial temperature, pressure, water saturation, NaCl molar fraction, and salinity conditions in host-rock (surrounding rock) and diapir domains.

Zone	Temperature [°C]	Pressure [bar]	SW [%]	NaCl [mol %]	Salinity [gr kg^{-1}]
Surrounding rock	Linear gradient 35 °C km^{-1} with T_{surf} = 10°C	Hydrostatic	100	0.27	8.8
Diapir	58	Hydrostatic	100	7.5	320

Table 6-5. Boundary conditions applied to the 3D model

Zone	Conditions
Bottom Faces	No flux
Lateral Faces	Fixed pressure: pressure gradient of 0.002% between laterals min. and max.
Top Faces	Flux: meteoric recharge with a volumetric flow rate of 2.9×10^{-4} m^3 s^{-1}

6.2 Modelling results

Figure 6-3 illustrates the fluid phase velocity distribution at the end of the simulation run (10 kyr) under the two different scenarios (A, without caprock; B, with caprock). The vectors indicate the flow direction and magnitude. At this time step, the system has already reached a steady-state (i.e., since about 2 kyr after start of simulation). The velocity values range from 1×10^{-8} m s^{-1} in the shallow aquifer to 1×10^{-10} m s^{-1} in the deeper stratigraphic unit, corresponding to Q4 and Q2 values of the 0D geochemical modelling part, respectively. This decrease is due to the vertical heterogeneity of the layers in the domain. Peak velocity values (7×10^{-8} m s^{-1}) are observed at the top and upper flanks of the diapir, where fluid flow is constricted due to the presence of the impermeable diapiric structure. No clear difference in the flow regime of the two scenarios can be highlighted based on velocity distribution.

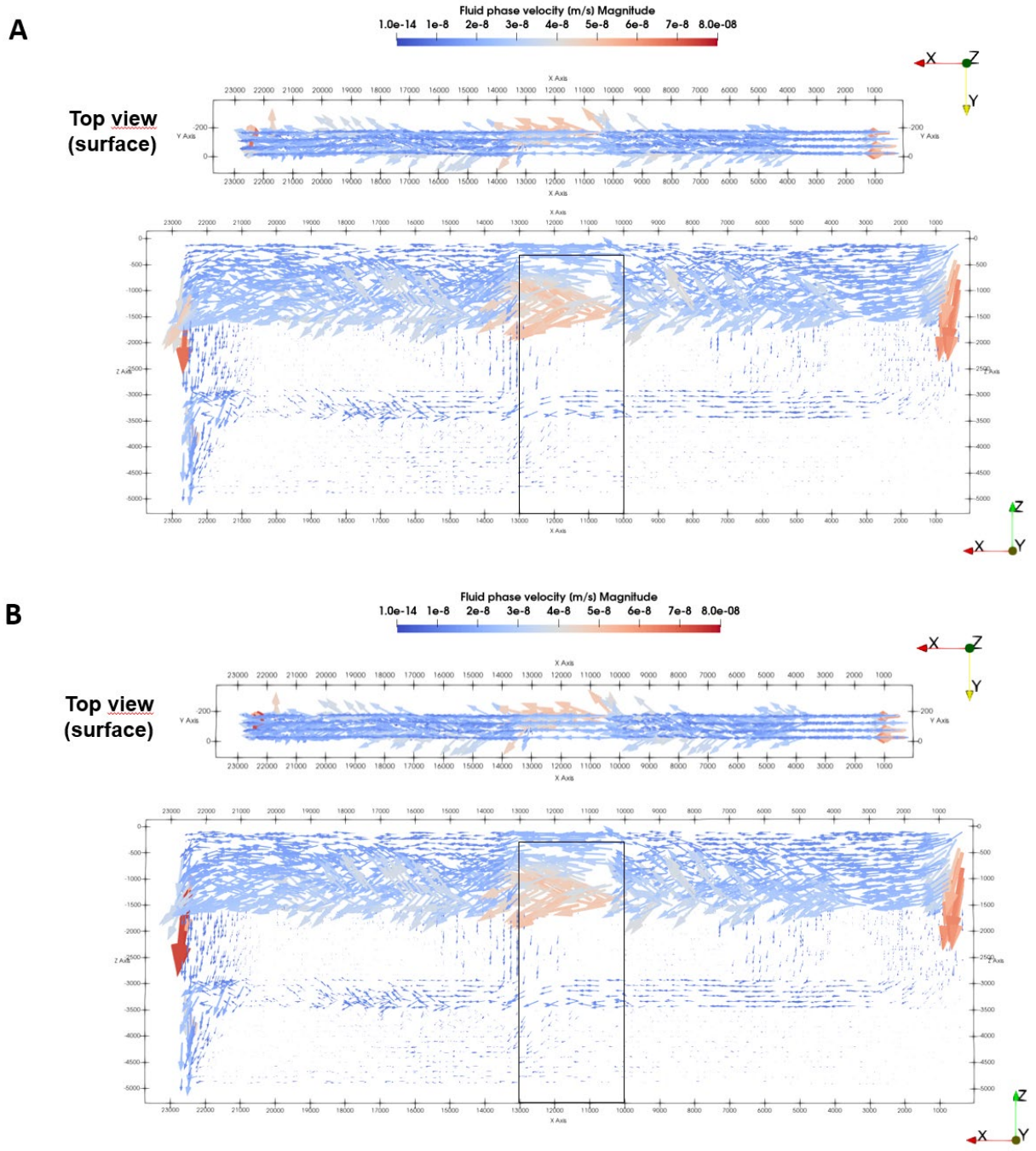

Figure 6-3. Fluid phase velocity distribution at 10 kyr without 'caprock' (A) and with 'caprock' (B). For (A) and (B): (above) a top view, at the surface of the grid showing the fluid circulating above the diapir in the host-rock; (below) a side view of the model (along x-axis) showing the fluid velocity distribution in the host-rock. The vectors indicate the flow direction and magnitude. A scale factor of 2 was applied on the z-axis to ease the readability.

Figure 6-4 presents the distribution of the tracer concentration within the model domain under the two different scenarios (A, without caprock; B, with caprock) and highlights how the presence of a caprock affects the tracer transport at the top of the diapir. The absence of a less permeable caprock allows for a more homogeneous distribution of the tracer and higher concentration at the top of the diapir. In contrast, when a caprock is present, the tracer distribution at the top of the diapir is significantly altered. The caprock acts as a barrier, preventing fluid and tracer from migrating over the top of the diapir. As a result, a tracer concentration gradient is observed from the inflow side to the center of the anhydrite caprock diapir suggesting that the caprock prevents high fluid phase velocity.

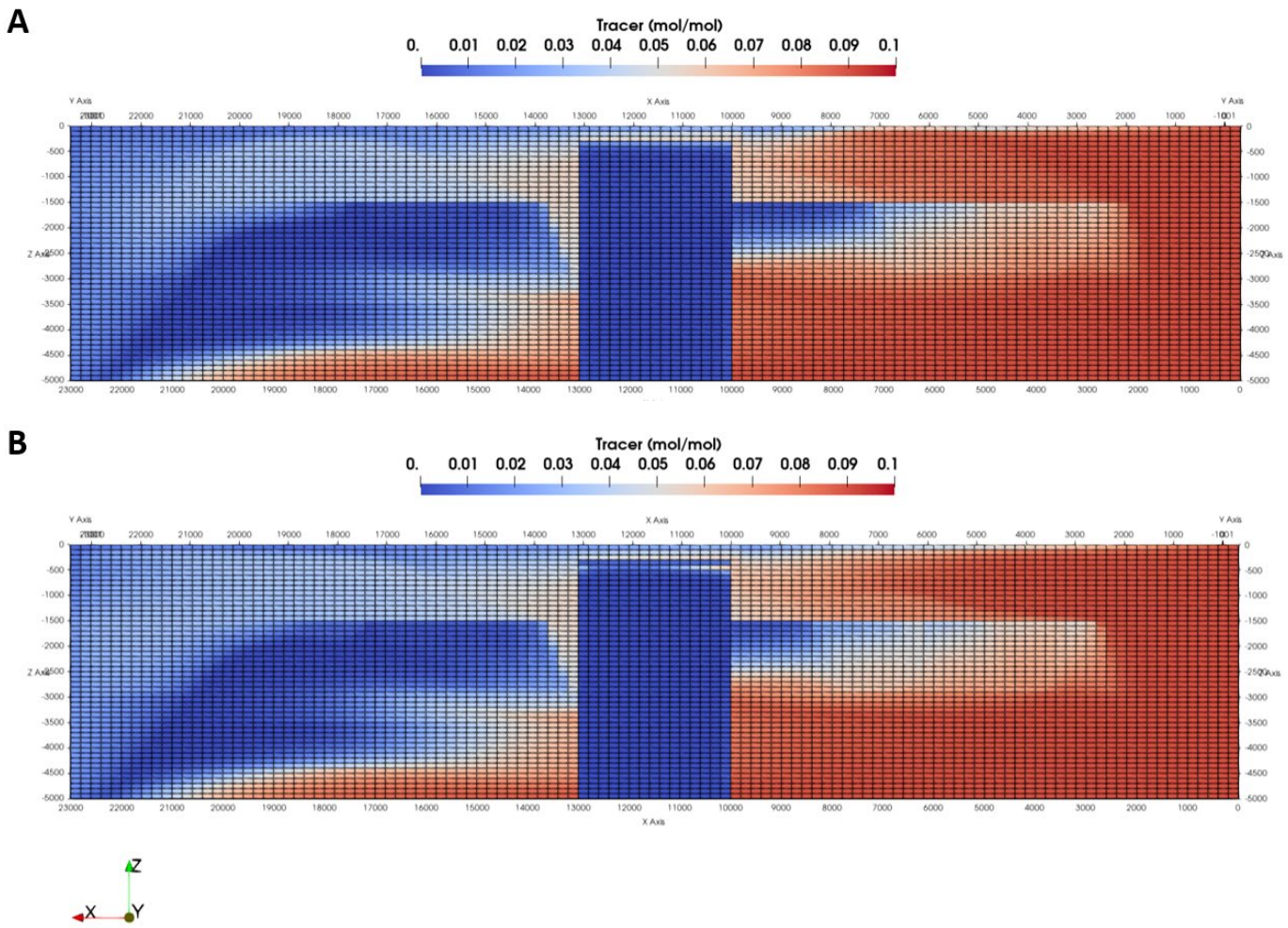

Figure 6-4. Tracer distribution throughout the model at the end of the simulation time (10 kyr), for the scenario without 'caprock' (A) and the scenario with 'caprock' (B). The initial tracer concentration was set at 0 mol% while the tracer concentration of the recharging fluid (by the top of the model and the right lateral boundary) was set at 10 mol%. The tracer distribution follows the different unit permeabilities. The "tail" observed at the left side corresponds to the ΔP set at the lateral boundaries to generate a horizontal flow. This pattern is also observed in Figure 6-3. A scale factor of 2 was applied on the z-axis to ease the readability.

Figure 6-5 presents the calculated subrosion rates, based on the reactive transport modelling results, at the top (Fig. 6-5A) and the margins (Fig. 6-5B) of the diapir under two different scenarios: no caprock and with caprock.

Figure 6-5A shows the subrosion rate along the distance from the inflow side of the salt mirror (top part of the diapir, cf., Geluk et al., 1993) for both external and internal portions of the salt structure. The results indicate that the subrosion rate is highest near the edges of the salt mirror for both scenarios, with a notable decrease in the middle region, followed by an increase again towards the edges. The presence of the caprock generally reduces the subrosion rate across the entire profile compared to the no caprock scenario, with the most significant differences observed towards the middle region of the salt mirror.

Figure 6-5B shows the subrosion rate along the margins of the diapir for the no caprock scenario and caprock scenario. The downstream and upstream flanks are distinguished. The subrosion rate decreases with depth in both scenarios and the presence of the caprock significantly reduces subrosion rates in the shallower sections of the diapir. There is almost no variation in the subrosion rates between the upstream and downstream flanks for both scenarios.

Overall, the results indicate that the caprock scenario limits the dissolution of the salt diapir at its top

horizontally. The presence of caprock acts as a protective barrier that decreases the dissolution rates, particularly in the middle shallower portions of the salt structure.

A

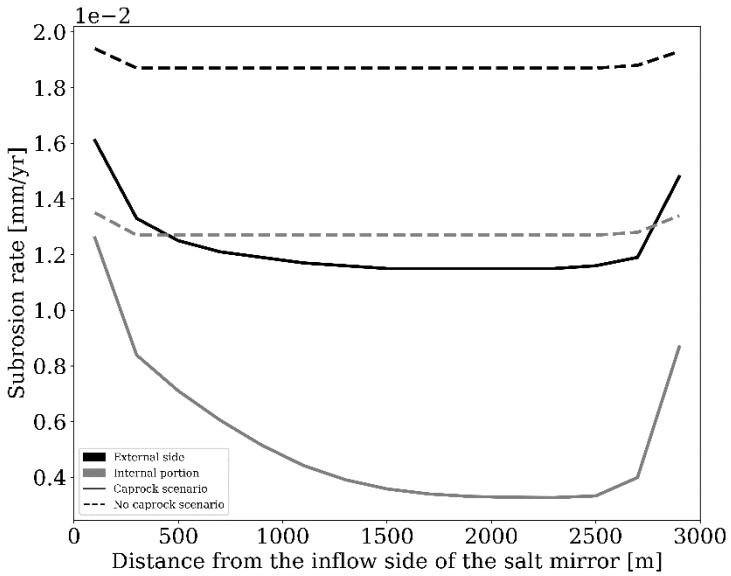

B

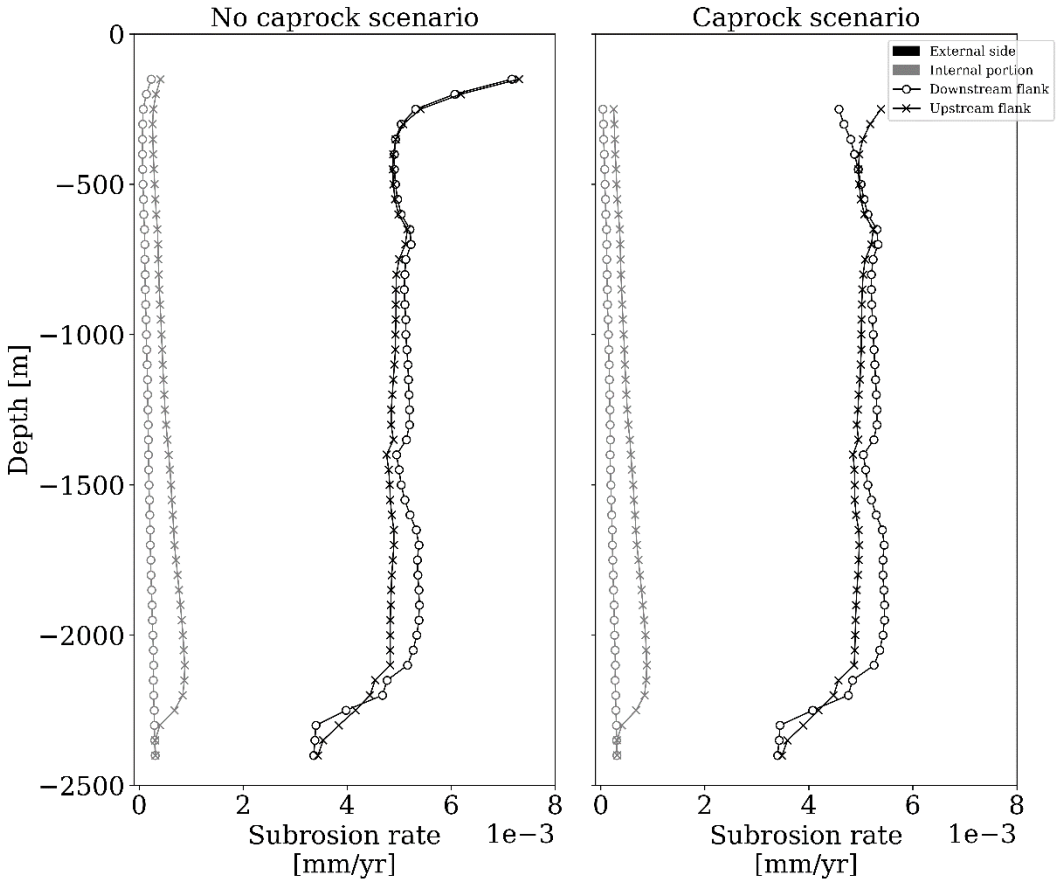

Figure 6-5. A) Cross-plot of calculated subrosion rate (mm yr^{-1}) with respect to distance at the top of the diapir from both external and internal sides; B) Cross-plots of calculated subrosion rate (mm yr^{-1}) at the margins of the diapir from both external and internal sides, and downstream and upstream flanks. No scale factor was applied.

6.3 Synopsis of the 3D reactive transport modelling

The main conclusions drawn from the results of the 3D reactive transport modelling representing the Permian Zechstein salt diapirs in the Netherlands are as follows:

- Subrosion at the top of the diapir (i.e., on the order of 1×10^{-2} mm yr^{-1}) is greater than at its margins (i.e., on the order of 1×10^{-3} mm yr^{-1}) due to the higher flow rate in that specific zone.
- The model incorporating caprock shows a significant reduction in the subrosion rate at the top of the diapir, with the rate being nearly halved compared to the scenario without caprock.
- The subrosion rate at the margins of the diapir remains of the same order of magnitude, whether on the upstream or downstream flanks, and depth has little effect on the calculated rate. This may be due to insufficient hydrogeological data, resulting in an unconstrained flow regime around the diapir in the reactive transport simulations.

Fluid flow velocity is one of the key parameters influencing the subrosion rate. Therefore, it is recommended to:

- Collect more data on flow velocities, permeabilities around the salt diapir, and the hydraulic gradient at the regional scale.
- Extend the lateral boundaries of the model and consider a complete 3D representation of the diapir to avoid altering the velocity field around it.

7 Conclusions

We investigated salt diapirism and salt subrosion in the northeast Netherlands by the means of numerical modelling approaches. Our study started from a readily available regional geological model combining both deep (DGM Diep v.5) and shallow (DGM v.2.2) stratigraphic surfaces constrained by 3D reflection seismic and well data. Based on this available geological data we have constructed a detailed (250-m resolution) basin-scale model that employed 22 Permian – Quaternary stratigraphic surfaces, with increased resolution for the last 2 Ma. We employed a quantitative structural modelling restoration approach for the Zechstein salt to quantify the rates of diapirism, evolution of various salt structures and the connection with the thermal and fluid flow evolution at these different stratigraphic stages in the northeast Netherlands. Our model displays an increased temporal resolution for the most recent 2 Ma in order to assess the most recent diapir evolution in detail for forecasting the stability of salt domes for the next 1 Ma. The large salt domes that reach 150-200m depth in the subsurface generally follow sub-salt fault systems activated during the Mesozoic extensional evolution with the salt decoupling deformation in the underburden from the overburden. Salt diapirism accelerated during the main tectonic events affecting the sedimentary basin and was particularly high (one order of magnitude higher) during the late Cretaceous – early Paleogene basin inversion. While diapirism remained relatively high during the remainder of the Tertiary, there is no direct evidence in our modelled dataset of any significant diapiric growth during the Pleistocene- Holocene, most large structures being gradually buried beneath ongoing sedimentation.

Our modelling results are in agreement with previous inferences that salt diapirs started to grow already during the Triassic times, when our results indicate for instance a diapirism rate of 6 m/My at the Anloo diapir, while at others the salt movement has lower rates to 1 m/My or below. The diapiric growth continued at similarly low rates during Jurassic - Early Cretaceous, being associated also with low sedimentation rates in the studied area. Salt diapirism has radically increased during the Late Cretaceous – Paleogene by many structures piercing the overburden, with the highest rate of 70 m/My modelled at Onstwedde. The modelling infers that some diapirs continued their growth during Paleogene times, such as 10 m/My modelled at Zuidwending, while others ceased their development. A similar situation is observed for Neogene times, the highest rate modelled being 6 m/My, while many diapirs stopped their ascent or started to lose thickness. The latter result may be connected with subrosion, since many diapirs reached shallow depths. The modelling infers that the reduction in diapiric thickness is on average -10 m/My in the Pleistocene – Holocene and resulted in a loss of thickness in the order of few hundred meters. Our modelling also infers that salt diapirism was not a significant process in this period. Even during and after the removal of sediments by glacial erosion when up to 300m of sediments were eroded, salt movements are not inferred by our modelling. All diapirs have been buried (i.e., negative diapirism rate) and were gradually reduced in size, possibly as an effect of subrosion processes. Extreme negative diapirism rates up to -400 m/My were calculated for the Holocene, although the resolution of our modelling for this time interval is fairly low. Our modelling also infers that if the current glacio-tectonic condition continues, the diapirs may not be activated in the coming one million years, while their burial may continue, reducing further the subrosion rate.

Previous studies combined with the results of the diapir evolution and the associated fluid and heat flow are used as input to the subsequent reservoir-scale modeling of subrosion. Two complementary modelling approaches were applied: (1) 0D geochemical modelling using Arxim to study the effects of different environmental conditions on salt rock subrosion over a 1 Ma period, and (2) 3D reactive transport modelling using Geoxim to investigate the subrosion processes at the top and flanks of salt domes over 10-ka period. Subrosion rates were calculated through geochemical modelling for Halite, Sulphate (halite + anhydrite), and K-Mg Salt facies, considering varying salinities (1 to 90 g/L), temperatures (20 to 80°C), and Darcy flow velocities (1×10^{-6} m/yr to 5×10^{-3} m/yr), over 1 Ma. The results show that Darcy flow velocity has the most significant impact on subrosion rates which increase linearly with rising velocity for halite and potassium – magnesium salt facies. Less pronounced than the influence of the Darcy's velocity, the subrosion rate is also

influenced by the composition of the subroding fluid: the more negative the fluid's saturation index with respect to the diapir mineralogical composition, the higher the subrosion rate. Recharge fluids that are away from equilibrium with carnallite and kieserite lead to these minerals dissolving more quickly than halite and anhydrite. The initial mineralogy of the subroded rock is very important: the subrosion rate increases with a higher proportion of potassium-magnesium salt and decreases with an increase in the amount of anhydrite. The temperature range considered has a negligible effect on the subrosion rate compared to Darcy velocity, salinity, or initial mineralogy. Subrosion at the top of the diapir (i.e., on the order of 10 m/My) is greater than at its margins (i.e., on the order of 1 m/My) due to the higher flow rates in that specific shallower zone. The model incorporating caprock shows a significant reduction in the subrosion rate at the top of the diapir, with the rate being nearly halved compared to the scenario without caprock. The subrosion rate at the margins of the diapir remains of the same order of magnitude, whether on the upstream or downstream flanks, and depth has little effect on the calculated rate. These results may also be due to the low amount of hydrogeological constraints used in our study, resulting in a less constrained flow regime around the diapir in the reactive transport simulations.

In summary, our 3D basin model shows long-term net diapirism rates ranging from a few m/My in the Triassic – Early Cretaceous, 70 m/My in the Late Cretaceous to below 10 m/My in the Paleogene – Neogene. Diapirs have been buried and were reduced in thickness in Pleistocene – Holocene with an average negative diapirism rate of -10 m/My and extreme rates up to -400 m/My in Holocene. Our 3D reactive transport model infers a subrosion rate of 10 m/My on the top of the diapirs, and 1 m/My on the margins under theoretical situations, while the flow regime around the diapirs could change these values drastically when hydrogeological conditions change more significantly than assumed. Our 0D parametric study explores the impacts of varying fluid salinity, temperature and fluid flow and reports broad subrosion rates ranging from 180 m/My to 3×10^7 m/My, strongly dependent on the Darcy flow velocity. Considering the overall recent evolution of the salt diapirs and the results of the more reliable 3D reactive transport model, the modelling suggests that a surrounding salt thickness of 350 m, currently assumed in the current Netherlands disposal concept, seems to be conservative enough for preventing diapirism and subrosion impairing the natural barrier and affecting the safety of the repository for the next one million years.

Given existing constraints and uncertainties of the geological models used as input and the type of modelling used in our study factoring the short time available for the project, we strongly recommend further studies continuing on a more quantitative understanding of diapirism and subrosion for the development of accurate repository performance models, safety assessments, and long-term management strategies. We recommend improvements on: (1) an improved representation of the geometry of the salt structures by a higher resolution interpretation of the available seismic and well data, (2) improving the numerical modelling in a two-steps procedure by adding a forward numerical modelling technique and a fully coupled thermos-mechanical-geochemical approach, (3) building an improved subrosion dataset in terms of flow velocities, permeabilities around the salt diapir, and the hydraulic gradient at the regional scale, and (4) extending the lateral boundaries of the subrosion model and consider a complete 3D representation of the diapir to avoid altering the velocity field around it.

Data availability

The model and datasets generated by this study can be accessed via https://surfdrive.surf.nl/files/index.php/s/d694hMOfPVeLLTb.

References

Al-Halbouni, D., Holohan, E.P., Saberi, L., Alrshdan, H., Sawarieh, A., Closson, D., Walter, T.R., Dahm, T., 2017. Sinkholes, subsidence and subrosion on the eastern shore of the Dead Sea as revealed by a close-range photogrammetric survey. Geomorphology 285, 305-324. 10.1016/j.geomorph.2017.02.006

Almaki, B., 2023. Zechstein Salt Structures Evolution in the Northeastern Netherlands. MSc internship COVRA - University of Utrecht, 35pp.

Bartol, J., & Vuorio, M. (2022). Disposal of radioactive waste in rock salt: Long-term research programme. In The Mechanical Behavior of Salt X (pp. 236-241). CRC Press.

BEICIP-FRANLAB, 2023. OpenFlow Suite 2021, Rueil Malmaisson, France, 2021, https://www.beicip.com/sites/default/files/ofs2021_releasenotes.pdf

Bérest, P., Béraud, J.F., Gharbi, H., Brouard, B., DeVries, K., 2014. A very slow creep test on an Avery Island salt sample. Am. Rock Mech. Assoc.

Bonte, D., J.-D. Van Wees, and J. Verweij, Subsurface temperature of the onshore netherlands: new temperature dataset and modelling, *Netherlands Journal of Geosciences*, *91* (4), 491–515, 2012.

Brun, J.-P., Nalpas, T., 1996. Graben inversion in nature and experiments. Tectonics 15, 677-687. https://doi.org/10.1029/95tc03853

Burton, Z.F.M., Dafov, L.N., 2023. Salt Diapir-Driven Recycling of Gas Hydrate. Geochem. Geophys. Geosyst. 24, e2022GC010704. https://doi.org/10.1029/2022GC010704

Daudré, B., Cloetingh, S., 1994. Numerical modelling of salt diapirism: influence of the tectonic regime. Tectonophysics 240, 59-79. https://doi.org/10.1016/0040-1951(94)90264-X

Desbois, G., Urai, J.L., de Bresser, J.H.P., 2012. Fluid distribution in grain boundaries of natural fine grained rock salt deformed at low differential stress (Qom Kuh salt fountain, central Iran): Implications for rheology and transport properties. J. Struct. Geol. 43, 128–143.

Duin, E. J. T., Doornenbal, J. C., Rijkers, R. H., Verbeek, J. W., & Wong, T. E. (2006). Subsurface structure of the Netherlands-results of recent onshore and offshore mapping. Netherlands Journal of Geosciences, 85(4), 245.

Estublier, A., Fornel, A., Brosse, É., Houel, P., Lecomte, J.-C., Delmas, J. and Vincké, O., 2017. Simulation of a Potential CO2 Storage in the West Paris Basin: Site Characterization and Assessment of the Long-Term Hydrodynamical and Geochemical Impacts Induced by the CO2 Injection. Oil Gas Sci. Technol. – Rev. IFP Energies nouvelles 72, https://doi.org/10.2516/ogst/2017021.

Fattah, R. A., Verweij, J. M., Witmans, N., & Ten Veen, J. H. (2012). Reconstruction of burial history, temperature, source rock maturity and hydrocarbon generation in the northwestern Dutch offshore. Netherlands Journal of Geosciences, 91(4), 535-554.

Gabrielsen, R.H., Giannenas, P.A., Sokoutis, D., Willingshofer, E., Hassaan, M., Faleide, J.I., 2023. Analogue experiments on releasing and restraining bends and their application to the study of the Barents Shear Margin. Solid Earth 14, 961-983. 10.5194/se-14-961-2023

Geluk, M.C., Dammam, A.H., Klaver, G.T., Obdam A., 1993. Evaluation of salt bodies and their overburden in the Netherlands for the disposal of radioactive waste. Part C: Caprock formation and subrosion, Rijks Geologishe Dienst, 48 pp.

Geluk, M.C., 2007. Salt. In Geology of the Netherlands, Royal Netherlands Academy of Arts and Sciences, Amsterdam, 2007, pp. 63-84.

Gerardi, J., and Wildenborg, A.F.B., 1999. Szenarienanalyse, szenarienbewertung und geologische langzeitprognose fur das Endlager fur radioaktive Abfalle Morsleben (ERAM), BGR Report, 200pp.

Griffioen, J., Verweij, H. and Stuurman, R., 2016. The composition of groundwater in Palaeogene and older formations in the Netherlands. A synthesis. Netherlands Journal of Geosciences, 95(3), pp.349-372.

Hansen, F.D., Kuhlman, K.L., Sobolik, S.R., 2016. Considerations of the differences between bedded and domal salt pertaining to disposal of heat-generating nuclear waste. Sandia National Lab.(SNL-NM).

Harding, R., Huuse, M., 2015. Salt on the move: Multi stage evolution of salt diapirs in the Netherlands North Sea. Mar. Petrol. Geol. 61, 39-55. https://doi.org/10.1016/j.marpetgeo.2014.12.003

Hummelman, J., D. Maljers, A. Menkovic, R. Reindersma, J. Stafleu, and R. Vernes, Totstand-komingsrapport digitaal geologisch model (dgm), *Report: TNO*, *11653*, 2019.

Hunfeld, L.B., Pluymaekers, M.P.D., Larède, V., 2023. Database with the Thermal, Hydrological, Mechanical, Chemical (THMC) Properties of Rock Salt. TNO Publiek, Report No. R10585, Utrecht, The Netherlands, pp. 21.

Jackson, M.P.A., Hudec, M.R., 2017. Internal Deformation in Salt Bodies, Salt Tectonics: Principles and Practice. Cambridge University Press, Cambridge, pp. 181-228. DOI: 10.1017/9781139003988.011

Kothe, A., Hoffmann, N., Krull, P., Zirngast, M., Zwirner, R., 2007. Geology of the overburden and adjoining rock of the Gorleben salt dome, BGR report, 220pp.

Kobe, M., Gabriel, G., Weise, A., Vogel, D., 2019. Time-lapse gravity and levelling surveys reveal mass loss and ongoing subsidence in the urban subrosion-prone area of Bad Frankenhausen, Germany. Solid Earth 10, 599-619. 10.5194/se-10-599-2019

Kombrink, H., Doornenbal, J.C., Duin, E.J.T., den Dulk, M., ten Veen, J.H., Witmans, N., 2012. New insights into the geological structure of the Netherlands; results of a detailed mapping project. Netherlands Journal of Geosciences - Geologie en Mijnbouw 91, 419-446. 10.1017/S0016774600000329

Lafosse, M., Smit, J., 2020. RiFa - "Rise and Fall", the role of thermal uplift in the formation of Jurassic basins in the Dutch subsurface, Public summary, EBN Kennisbank, https://www.ebn.nl/feiten-en-cijfers/kennisbank/aardgas/rifa-rise-and-fall-the-role-of-thermal-uplift-in-the-formation-of-jurassic-basins-in-the-dutch-subsurface/

Lang, J., Hampel, A., Brandes, C., Winsemann, J., 2014. Response of salt structures to ice-sheet loading: implications for ice-marginal and subglacial processes. Quaternary Science Reviews 101, 217-233. https://doi.org/10.1016/j.quascirev.2014.07.022

Lauwerier, W., 2022. Evolution of the Zechstein salt diapirs in the northeast Netherlands. MSc internship COVRA - University of Utrecht, 61pp.

Lemgruber-Traby, A., Espurt, N., Souque, C., Henry, P., Calderon, Y., Baby, P. and Brusset, S., 2020. Thermal structure and source rock maturity of the North Peruvian forearc system: Insights from a subduction-sedimentation integrated petroleum system modeling. Marine and Petroleum Geology

122, 104664, https://doi.org/10.1016/j.marpetgeo.2020.104664.

Manea, V.C., Armaş, I., Manea, M., Gheorghe, M., 2021. InSAR surface deformation and numeric modeling unravel an active salt diapir in southern Romania. Scientific Reports 11, 12091. 10.1038/s41598-021-91517-4

Magri, F., Bayer, U., Jahnke, C., Clausnitzer, V., Diersch, H.J., Fuhrman, J., Möller, P., Pekdeger, A., Tesmer, M., Voigt, H. J., 2005.

Ministry of infrastructure and the Environment, 2016. The national programme for the management of radioactive waste and spent fuel, p. 61.**There are no sources in the current document.**

Nader, F.H. (2016). Multi-scale Quantitative Diagenesis and Impacts on Heterogeneity of Carbonate Reservoir Rocks. Springer, ISBN: 978-3-319-46444-2, 146p.

Nader, F.H., van Unen, M., Darnault, R., Rudkiewicz, J.L., Matenco, L., 2023. Coupled kinematic and thermal modelling of collisional orogens: Implications for subsurface geo-resources assessment in the external Dinarides. Global Planet. Change 223, 104090. https://doi.org/10.1016/j.gloplacha.2023.104090

Nalpas, T., Le Douaran, S., Brun, J.P., Unternehr, P., Richert, J.P., 1995. Inversion of the Broad Fourteens Basin (offshore Netherlands), a small-scale model investigation. Sediment. Geol. 95, 237-250. https://doi.org/10.1016/0037-0738(94)00113-9

Palandri, J. L., & Kharaka, Y. K. (2004). A compilation of rate parameters of water-mineral interaction kinetics for application to geochemical modeling (No. 2004-1068). US Geological Survey.

Peryt, T., Geluk, M., & Mathiesen, A. Paul, J. and Smith, K., 2010. Zechstein. Petroleum Geological Atlas of the Southern Permian Basin Area, 123-147.

Prij, J., Blok, B.M., Laheij, G.M.H., Van Rheenen, W Slagter, W Uffink, G.J.M., Uijt de Haag, P., Wildenborg, A.F.B., Zanstra, D.A., 1993. Probabilistic Safety Assessment, Final Report of ECN, RTVM and RGD in Phase 1A of the OPLA Programme. In: Geological problems in radioactive waste isolation. Second Worldwide Review. Witherspoon, P.A. (ed.), LBNL-38915, p. 161-181

Rowan, M.G., Giles, K.A., 2021. Passive versus active salt diapirism. AAPG Bulletin 105, 53-63. 10.1306/05212020001

Schultz-Ela, D.D., Jackson, M.P.A., Vendeville, B.C., 1993. Mechanics of active salt diapirism. Tectonophysics 228, 275-312. https://doi.org/10.1016/0040-1951(93)90345-K

Smit, J., Brun, J.P., Fort, X., Cloetingh, S., Ben-Avraham, Z., 2008. Salt tectonics in pull-apart basins with application to the Dead Sea Basin. Tectonophysics 449, 1-16. https://doi.org/10.1016/j.tecto.2007.12.004

Strozyk, F., L. Reuning, M. Scheck-Wenderoth, and D. Tanner, The tectonic history of the zech- stein basin in the netherlands and germany, in *Permo-Triassic salt provinces of Europe, North Africa and the Atlantic Margins*, pp. 221–241, Elsevier, 2017.

Tesauro, M., Kaban, M. K., & Cloetingh, S. A. (2008). EuCRUST-07: A new reference model for the European crust. Geophysical Research Letters, 35(5).

Tilita, M., Scheck-Wenderoth, M., Matenco, L., Cloetingh, S., 2015. Modelling the coupling between salt kinematics and subsidence evolution: Inferences for the Miocene evolution of the Transylvanian Basin. Tectonophysics 658, 169-185. https://doi.org/10.1016/j.tecto.2015.07.021

TNO – GDN (2019) DGM-deep v5.0. TNO - Geological Survey of the Netherlands,

https://www.dinoloket.nl/en/subsurface-models/Myp

TNO – GDN (2014) BRO DGM v2.2. TNO - Geological Survey of the Netherlands, https://www.dinoloket.nl/en/subsurface-models/Myp

Urai, J.L., Schléder, Z., Spiers, C.J., Kukla, P.A., 2008. Flow and transport properties of salt rocks. Dyn. complex Intracont. basins Cent. Eur. basin Syst. 277–290.

Van Adrichem Boogaert, H.A. & Kouwe, W.F.P. 1994. Stratigraphic nomenclature of The Netherlands; revision and update by RGD and NOGEPA, Section D, Permian.

Vis, G.J., Van Gessel, S.F., Mijnlieff, H.M., Pluymaekers, M.P.D., Hettelaar, J.M.M., Segers, D.P.M., 2010. Lower Cretaceous Rijnland Group aquifers in the West Netherlands Basin: suitability for geothermal energy. TNO report: TNO-034-UT-2009-02410.

Appendix

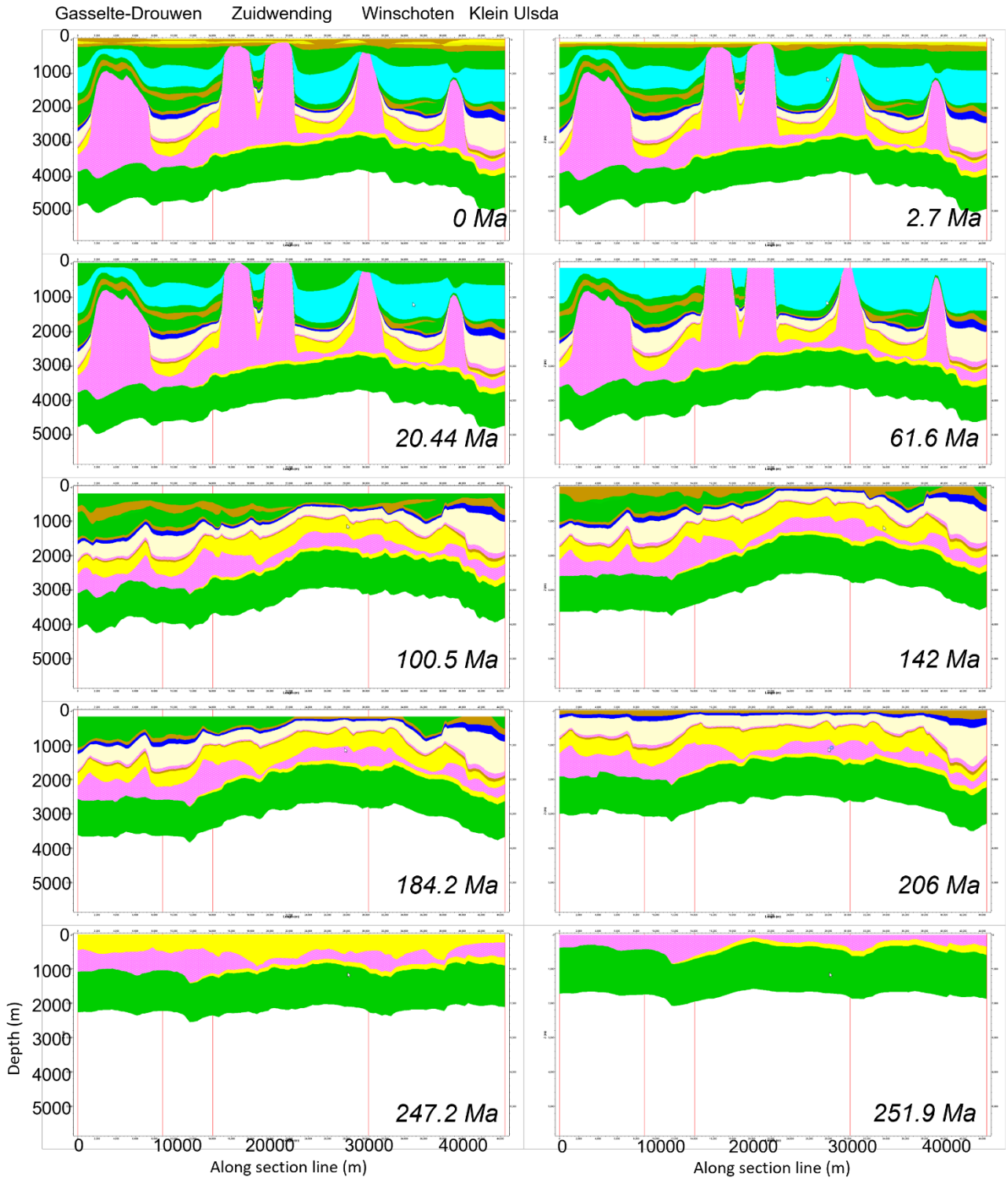

Figure A-1: Salt evolution along the cross-section S1 in Fig 2-1.

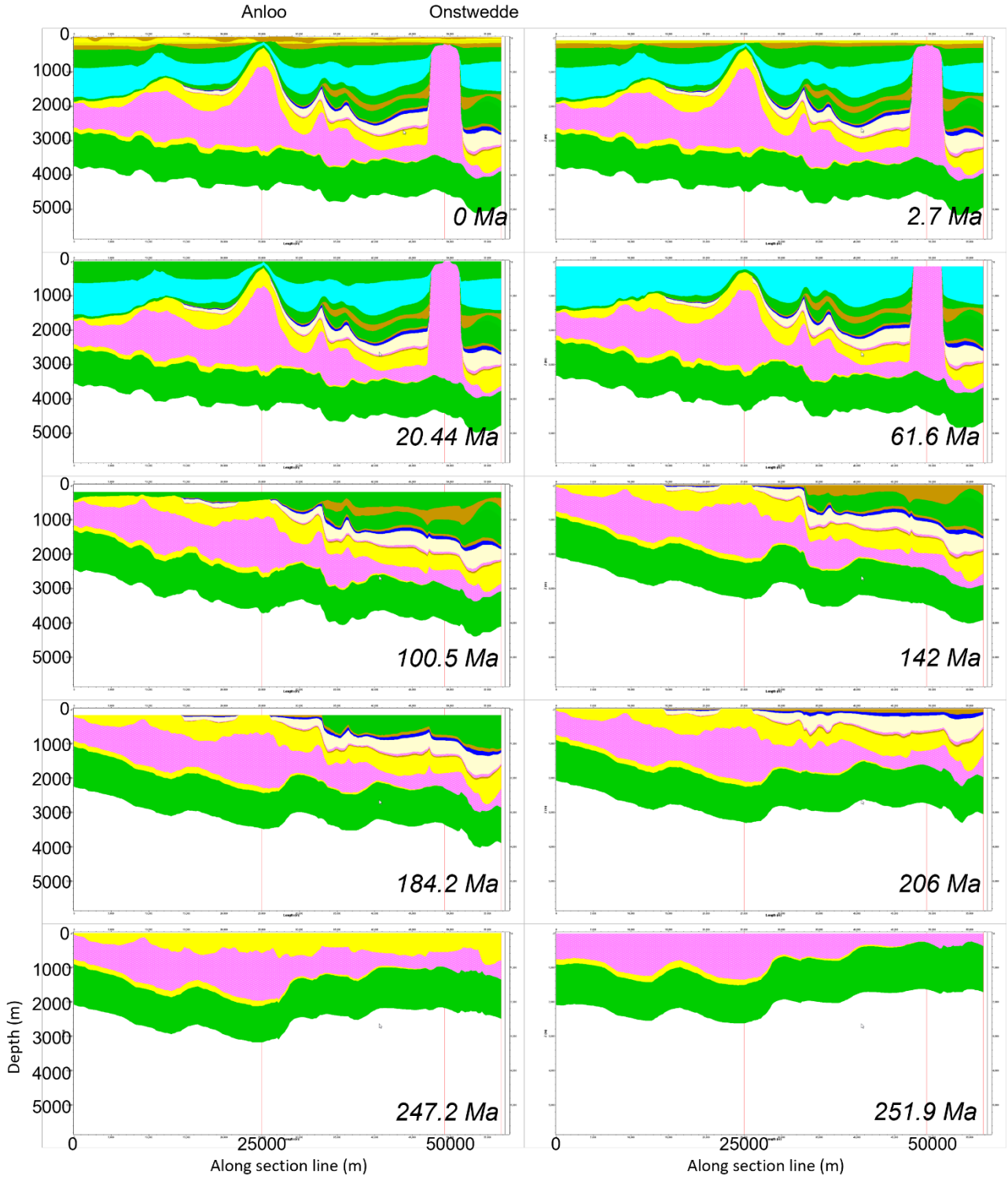

Figure A-2: Salt evolution along the cross-section S2 in Fig 2-1.

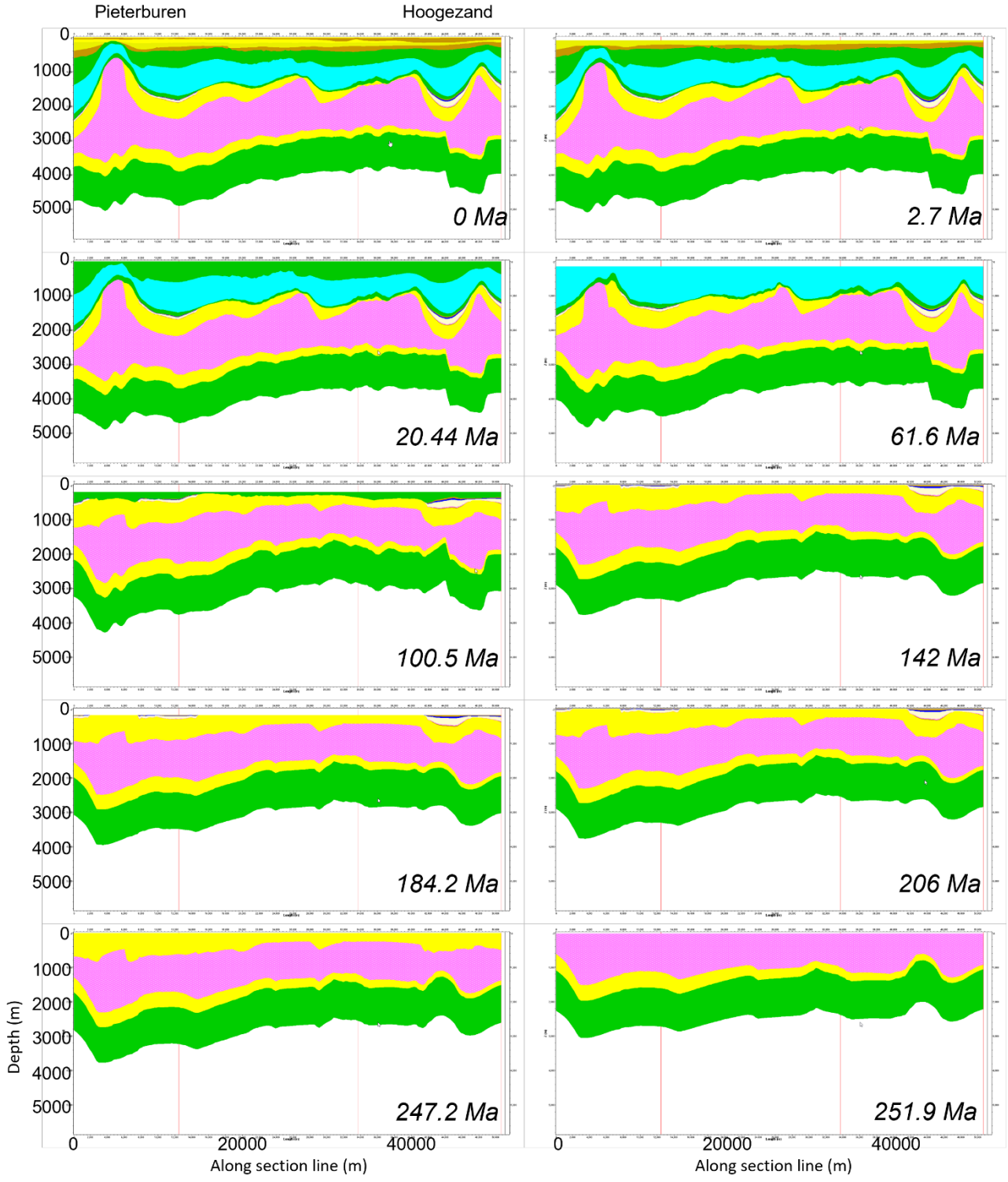

Figure A-3: Salt evolution along the cross-section S3 in Fig 2-1.

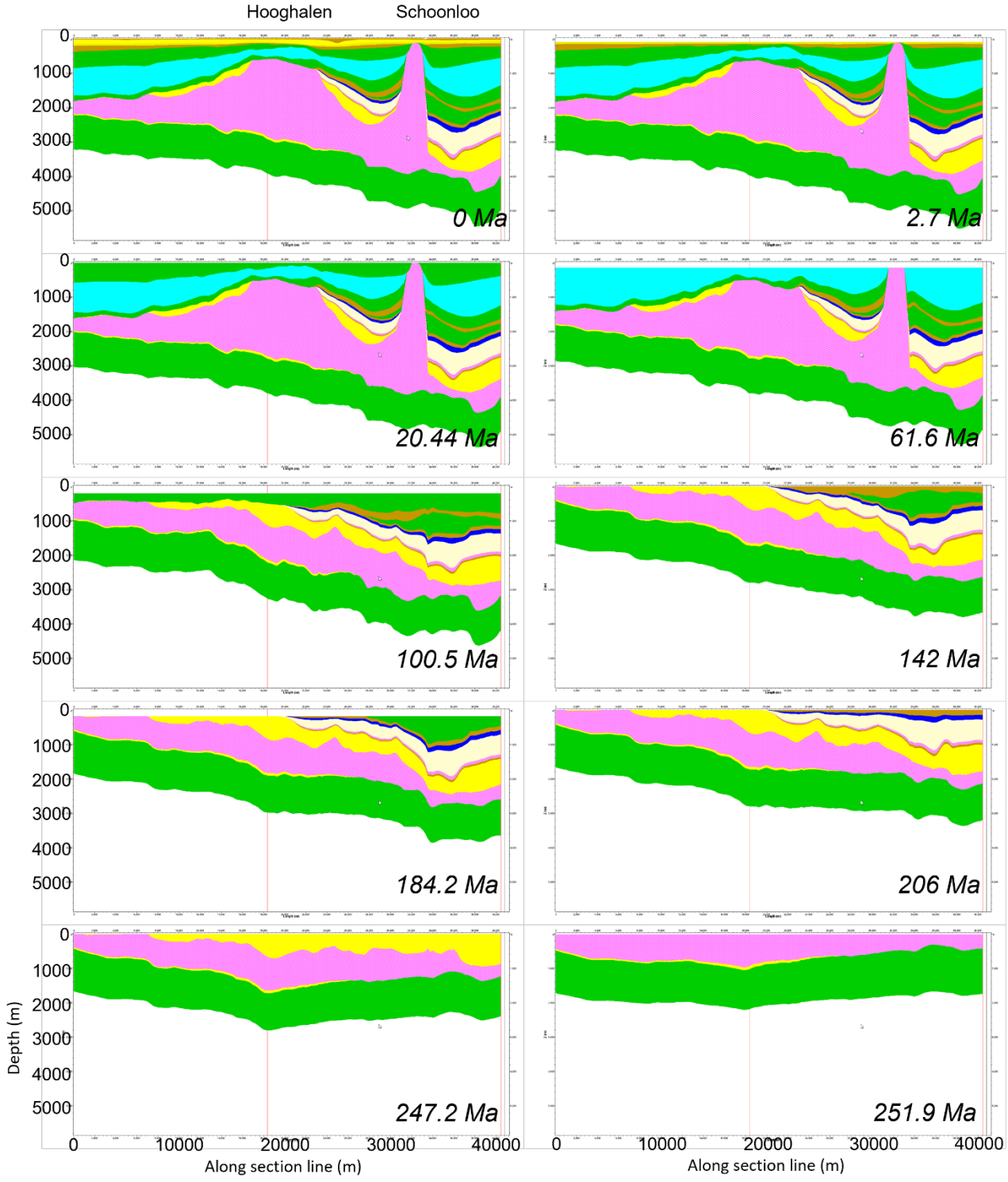

Figure A-4: Salt evolution along the cross-section S4 in Fig 2-1.

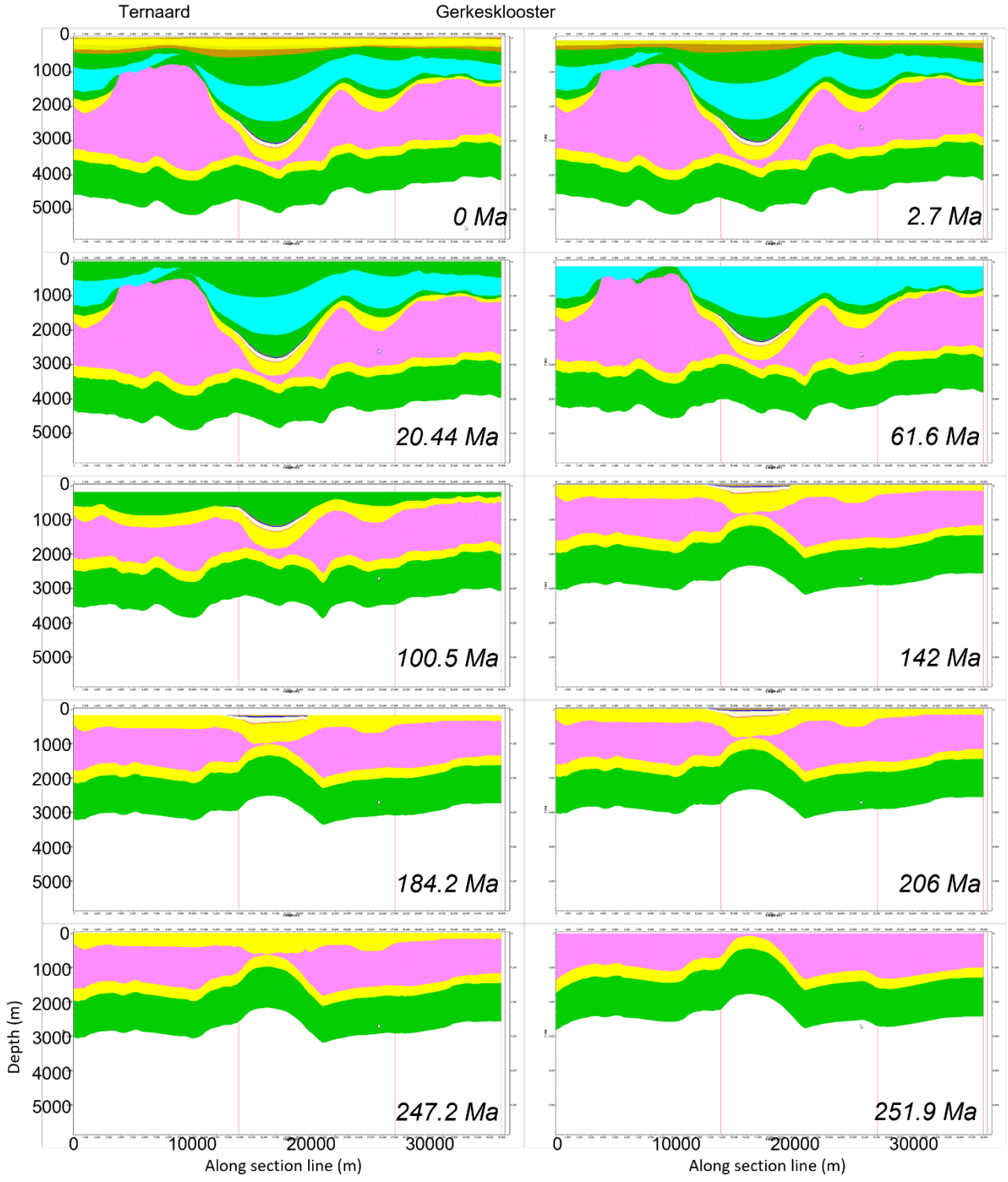

Figure A-5: Salt evolution along the cross-section S5 in Fig 2-1.

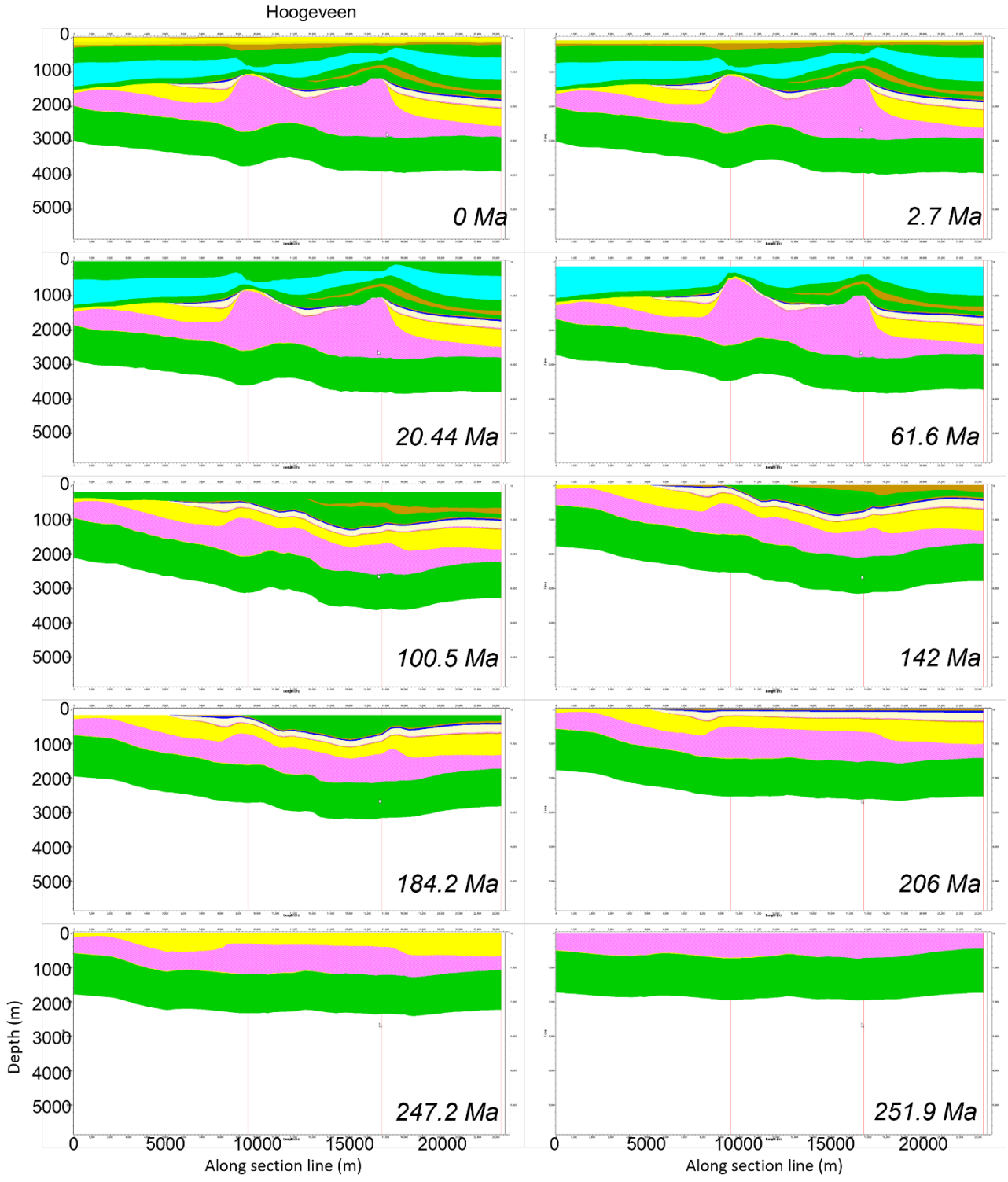

Figure A-6: Salt evolution along the cross-section S6 in Fig 2-1.